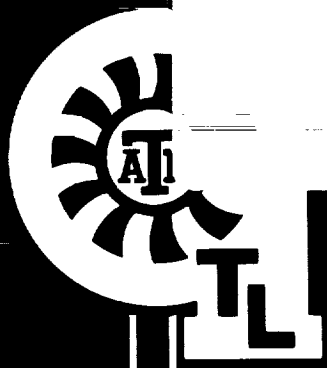

EP62/James Cannon

PART A: BULK-FLOW ANALYSIS

FINAL REPORT

NASA Contract No. NAS 8-37821

Dara W. Childs
Texas A&M University

10 December 1993

Turbomachinery Laboratory

PART A: BULK-FLOW ANALYSIS

FINAL REPORT

NASA Contract No. NAS 8-37821

Dara W. Childs
Jordan Professor of Mechanical Engineering
Turbomachinery Laboratory
Texas A&M University
College Station, TX 77843-3254

10 December 1993

Executive Summary

CDM 17

FINAL REPORT

NASA Contract No. NAS8-37821

EXECUTIVE SUMMARY

Introduction

The bulk-flow analysis results for this contract are incorporated in the following publications:

(a) Childs, D. (1991a), "Fluid-Structure Interaction Forces at Pump-Impeller-Shroud Surfaces for Axial Vibration Analysis," *ASME Trans., Journal of Vibration and Acoustics,* Vol. 113, pp. 113-115, January 1991

(b) Childs, D. (1991b), "Centrifugal Acceleration Modes for Incompressible Fluid in the Leakage Annulus Between a Shrouded Pump Impeller and Its Housing," *ASME Trans., Journal of Vibration and Acoustics,* Vol. 113, pp. 209-218, April 1991

(c) Williams, J. and Childs, D. (1992a), "Influence of Impeller Shroud Forces on Pump Rotordynamics," *ASME Trans., Journal of Vibration and Acoustics,* Vol. 113, pp. 509-515, October 1991

(d) Childs, D. (1992b), "Pressure Oscillation in the Leakage Annulus Between a Shrouded Impeller and Its Housing Due to Impeller-Discharge-Pressure Disturbances, *ASME Trans., Journal of Fluids Engineering,* Vol. 114, pp. 61-67, March 1992

(e) Cao, N. (1993), "Compressibility Effects on Rotor Forces in the Leakage Path Between a Shrouded Pump Impeller and Its Housing," M.S. M.E. Thesis, Texas A&M University, August 1993

Computational Fluid Mechanics (CFD) results developed by Dr. Erian Baskharone are reported separately. Two copies of these publications, were submitted as preliminary final reports under the terms of this contract and are incorporated in this final report.

The results of this study and the publications above can be summarized as follows:

Impeller Forces for Axial Vibration Analysis

Initial bulk-flow analyses for impellers considered radial reaction forces developed by impellers due to lateral rotor motion Reference (a) above examined the axial reaction forces, concluding that no resonance exists for axial motion. Methods are presented for calculating stiffness, damping, and added mass coefficients for axial vibrations of turbopumps.

Centrifugal Acceleration Modes

Prior to this study, Childs (1989) calculated reaction force components for an impeller due to precession of a pump rotor at nonsynchronous frequencies. His results showed unexpected peaks in the force components which he ascribed to fluid "resonance", arising from the centrifugal-acceleration term in the momentum equation. Dr. Brennen at Cal Tech questioned this terminology, suggesting that the term resonance could only be supported if an analysis confirmed that the governing system actually had complex eigenvalues at or near the locations of peak amplitudes. Childs (1991b) cited above, yielded roots and eigenvectors at the predicted locations, confirming the prior predictions of fluid resonances.

Influence of Impeller Shroud Forces on Pump Rotordynamics

A question presented by the initial predictions that impeller reaction forces could contain "peaks" was: How should radial and circumferential reaction forces be modeled if they can not be modeled with stiffness, damping, and added-mass coefficients? Furthermore, what influence do the predicted peaks have on rotordynamics? Williams and Childs (1992a) developed linear and nonlinear analysis procedures for incorporating the frequency-dependent radial and circumferential force coefficients into a rotordynamic analysis. Transient nonlinear analysis used the predicted reaction forces directly as a function of the instantaneous normalized precession frequency. Synchronous response due to imbalance proceeds directly, replacing the radial and circumferential force coefficients with direct and cross-coupled stiffness coefficients which are a function of running speed. Eigenanalysis is iterative, since the stiffness coefficients depend on the precession frequency which is in turn defined by the eigenvalue.

The predicted impeller-force peaks were shown to have a major influence on rotordynamics for the model considered. However, the results are difficult to generalize to turbomachinery rotordynamics.

Pressure Oscillation Excitation of the Flow in an Impeller Shrouded Annulus

The analyses cited above all considered reaction forces due to impeller shroud motion. Childs (1992b) looked at the separate problem of pressure and velocity predictions in the annulus due to precessing pressure oscillations at the discharge of the impeller. This analysis was not aimed at rotordynamics . The impeller is assumed to be spinning but not precessing.

Pressure oscillation from the impeller discharge propagate down through the annulus and out the exit wearing-ring seal. The analysis showed that multiple sharp resonances could be excited in the annulus and that they typically resulted in peak pressure oscillations at or near the exit wearing-ring seal. These results suggested a possible explanation for the internal-cooling problem for the KEL-F exit seals of the SSME-HPFTP. However, the applicability of the analysis was limited because an incompressible-flow model was used.

Compressibility Effects on Rotordynamics and Leakage and Pressure in an Impeller Annulus

Nhai's (1993) thesis extended previous models by incorporating fluid compressibility. Nhai uses a barotropic model for which the viscosity and density are functions of the pressure (only). Adding compressibility to the model means that acoustic modes can be generated in addition to the "centrifugal-accelerations" modes which were present in earlier analyses. Acoustic analysis normally discards perturbation terms which are included in Nhai's general perturbation analysis.

Nhai used the HPFTP first stage impeller for his analysis. He analyzed the exit wearing-ring seal leakage-ΔP relationship using a code developed by Morrison et al. (1983). Fluid properties were modeled via an NBS code, McCarthy et al. (1986).

Nhai examined the influence of compressibility on both rotordynamic characteristics of pumps and pressure and flow oscillations within the annulus due to pressure perturbations of the impeller exit. Concerning rotordynamic-response characteristics, Nhai's analysis sought to answer the following basic questions:

(a) What influence does compressibility have on the centrifugal-acceleration modes predicted by earlier analyses?

(b) What "acoustic" modes are predicted due to fluid compressibility?

The answers provided are as follows:

(a) Compressibility has a negligible influence on centrifugal-acceleration modes. The result with and without compressibility are basically the same.

(b) Fluid compressibility yields acoustic modes, with the lowest mode appearing at about twelve times running speed. This mode would be excited by rotor precession.

Concerning pressure oscillations within the leakage annulus, Nhai used a precessing pressure wave at the pump impeller exit for excitation with n diametral modes. Following Bolleter (1988), $n=n_1$ (impeller vanes) - n_2 (diffuser vanes) = 24-13=11. Nhai's analysis predicts sharp peaks at precessional frequencies which are 6.5 and 7.8 times running speed. These modes give predicted amplification factors from impeller discharge to the exit seal of the annulus

(inlet seal of the impeller) of 7.5 and 17.8. Either mode could reasonably explain the internal melting observed in the HPFTP seals. The difficulty is that no excitation frequency is predicted by existing theories near these resonant frequencies. Bolleter predicts excitation frequencies at multiples of $\Omega = n_1\ \omega/n$ where ω is the running speed. Table 2 (page 38) of Nhai's thesis shows no excitation frequencies at or near the resonant frequencies.

To be brief, the present analysis only provides a plausible explanation for the melting-seal situation, if the impeller provides the required excitation frequencies, and testing would be necessary to confirm their presence or absence.

REFERENCES

Bolleter, U., (1988), "Blade Passage Tones of Centrifugal Pumps," *Vibrations,* Vol. 4, pp. 8-13, September.

Childs, D. W., (1989), "Fluid-Structure Interaction Forces at Pump-Impeller-Shroud Surface for Rotordynamic Calculations," *ASME Trans., Journal of Vibrations, Acoustics, Stress, and Reliability in Design,*Vol. 111, pp. 216-225, July.

McCarthy, R.D., (1986), "Thermophysical Properties of Fluids, MIPROPS 86," NBS Standard Reference Data Base 12, Thermophysics Division, Center for Chemical Engineering, National Bureau of Standards, Boulder, Colorado.

Morrison, G.L., Rhode, D.L., Kogan, K.C., Chi, D., and Demco, J., (1983) "Labyrinth Seals for Incompressible Flow - Final Report," G.C. Marshall Space Flight Center, MSFC, Alabama, 35812, Report Number SEAL-4-83, November.

Childs, D.
(1991a)

PREV. ANN. 91A23668

Reprinted from January 1991, Vol. 113, Journal of Vibration and Acoustics

Fluid-Structure Interaction Forces at Pump-Impeller-Shroud Surfaces for Axial Vibration Analysis

D. W. Childs
Turbomachinery Laboratories,
Mechanical Engineering Department,
Texas A&M University,
College Station, TX 77843

Solutions are presented for the dynamic axial forces developed by pump-impeller-shroud surfaces. A bulk-flow model of the leakage path between the impeller and the housing is used for the analysis consisting of the path-momentum, circumferential-momentum, and continuity equations. Shear stresses at the impeller and housing surfaces are modeled according to Hirs' turbulent lubrication model. The governing equations were developed earlier to examine lateral rotordynamic forces developed by impellers.

A perturbation expansion of the governing equations in the eccentricity ratio yields a set of zeroth and first-order governing equations. The zeroth-order equations define the leakage rate, velocity distributions, and the pressure distribution for a centered impeller position. The first-order equations define the perturbations in the velocity and pressure distributions due to axial motion of the impeller. Integration of the perturbed pressure and shear-stress distribution acting on the rotor yields the reaction forces acting on the impeller face.

Calculated results yield predictions of resonance peaks of the fluid within the annulus formed by the impeller shroud and housing. Centrifugal acceleration terms in the path-momentum equation are the physical origin of these unexpected predictions. For normalized tangential velocities at the inlet to the annulus, $u_{\theta o}(0) = U_{\theta o}(0)/R_i\omega$ of 0.5, the phenomenon is relatively minor. As $u_{\theta o}(0)$ is increased to 0.7, sharper peaks are predicted. The fluid modes are well damped in all cases.

Numerical results are presented for a double-suction single-stage pump which indicate that the direct stiffness of the perturbed impeller shroud forces are negligible. Small but appreciable added-mass and damping terms are developed which have a modest influence on damping and peak-amplitude excitation frequency. The forces only became important for pumps with very low axial natural frequencies in comparison to the running speed, viz., ten percent of the running speed or lower.

Introduction

Figure 1 illustrates an impeller stage of a multistage centrifugal pump. Leakage along the front side of the impeller, from impeller discharge to inlet, is restricted by a wear-ring seal, while leakage along the back side is restricted by either an interstage seal or a balance-discharge seal. The axial thrust on the impeller is obviously of interest for structural integrity of the pump and several investigators have presented analyses and test results for the thrust versus various impeller parameters; Thomae and Stucki (1970), Lobanoff and Ross (1985). Impellers are sometimes used directly as thrust-balancing elements; e.g., the main impeller of the Space Shuttle Main Engine (SSME) High Pressure Oxygen Turbopump (HPOTP) is of double-suction-entry design, and orifices at the inlet and exit of the leakage path create the principal axial-thrust-balance for the rotor. The leakage-path for the back side of the High Pressure Fuel Turbopump (HPFTP) is also used for axial thrust balance.

From an axial vibration viewpoint, the change in the axial thrust of an impeller which is used for axial-thrust balance is normally modeled by a stiffness and damping coefficient, i.e.,

$$F_z = -KZ_r - C\dot{Z}_r \tag{1}$$

where Z_r is the axial change in position. The stiffness coefficient K is the local slope in the thrust versus axial position curve and is nominally constant around the equilibrium position. In the SSME turbopumps, the stiffness of the pump housing is used in series with the slope of the thrust-axial-position curve to calculate K. Damping primarily arises due to flow through orifice restrictions.

An implicit assumption involved in the model of equation (1) is that the natural frequencies of the fluid in the leakage path are much higher than the pump's running speed or the axial vibration frequencies of the rotor. From a conventional

Contributed by the Technical Committee on Vibration and Sound for publication in the JOURNAL OF VIBRATION AND ACOUSTICS. Manuscript received January 1990.

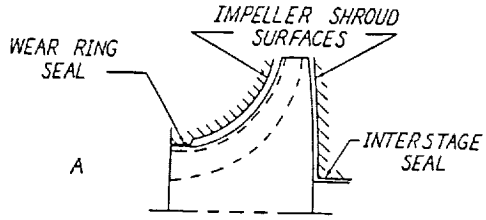

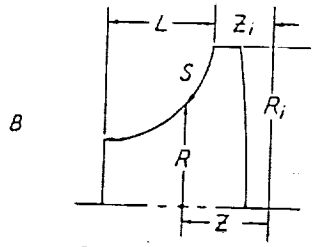

Fig. 1 Impeller stage

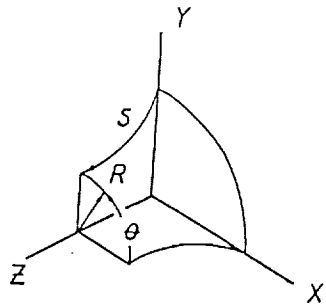

Fig. 2 Impeller surface geometry

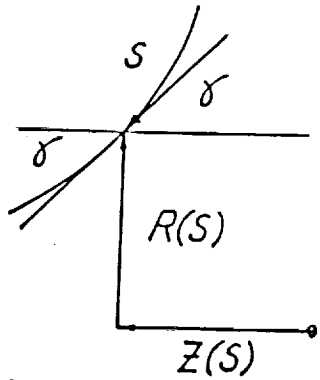

Fig. 3 Local attitude angle of impeller surface

acoustics viewpoint, this is certainly the case; however, Child's (1987, 1989) analysis of incompressible flow in the leakage path revealed resonances associated with the centrifugal acceleration of the inwardly-flowing fluid. The present investigation of the dynamic axial thrust developed by the pump impeller shroud is stimulated by the 1987 analysis and uses the same flow model.

Geometry and Kinematics

Figure 1 illustrates the annular leakage paths along the front and back sides of a typical shrouded impeller of a multistage centrifugal pump. The present discussion concentrates on the flow and pressure fields within the forward annulus; however, the analysis also applies to the rear annulus. As illustrated in Fig. 2, the outer surface of the impeller is a surface of revolution formed by rotating the curve $R = R(Z)$ about the Z axis. A point on the surface may be located by the coordinates $Z, R(Z), \theta$. The length along the curve $R(Z)$ from the initial

Nomenclature

a = nondimensional steady-state amplitude due to harmonic excitation, defined by equation (39)

A_{1s}, A_{2s}, A_{3s} = coefficients introduced in equation (18) and defined in the appendix

$A_{1\theta}, A_{2\theta}, A_{3\theta}$ = coefficients introduced in equation (18) and defined in the appendix

C_{de} = discharge coefficient for the exit wear-ring seal, introduced in equation (13)

C_i = initial ($s = 0$) clearance (L)

$f = \Omega/\omega$ = dimensionless axial excitation frequency

f_1, f_2, f_3 = dimensionless solution coefficients introduced in equation (25)

f_k, f_c = dimensionless force coefficients introduced in equation (31)

F_0 = nominal axial reaction force defined by equation (30)

F_Z = axial reaction force (F)

$h = H/C_i$ = nondimensionalized clearance

H = clearance between impeller shroud and housing (L)

L_s = leakage-path length, defined by equation (3), (L)

$p = P/\rho V_i^2$ = nondimensionalized static fluid pressure

P = fluid static pressure (F/L^2)

$r = R/R_i$ = nondimensionalized radial coordinate

R = radial coordinate (L)

R_i = initial ($s = o$) radius (L)

$R_s = 2HU_s/\nu$ = path-velocity Reynolds number

$s = S/L_s$ = nondimensionalized path length

S = path coordinate introduced in equation (2), (L)

$T = L_s/V_i$ = representative transit time for fluid traversing the leakage path (T)

$u_s = U_s/V_i$ = nondimensionalized path fluid velocity

$u_\theta = U_\theta/R_i\omega$ = nondimensionalized circumferential fluid velocity

V_i = initial ($s = 0$) fluid velocity

ψ = steady-state phase due to harmonic excitation, defined by equation (39)

ϵ = perturbation coefficient

ω = pump running speed (T^{-1})

ω_n = pump axial natural frequency (T^{-1})

$\bar{\omega}_n = \omega_n/\omega$ = dimensionless pump axial natural frequency

Ω = axial excitation frequency (T^{-1})

ρ = fluid density (M/L^3)

θ = circumferential coordinate

σ_r, σ_s = normalized friction factors, defined by equation (15)

$\tau = \omega t$ = nondimensionalized time

ξ = entrance-loss coefficient introduced in equation (11)

$\delta = \Delta/C_i$ = nondimensionalized axial impeller displacement

Δ = axial impeller displacement (L)

point R_i,Z_i to an arbitrary point R,Z is denoted by S and defined by

$$S=\int_{Z_i}^{Z}\sqrt{1+\left(\frac{dR}{dZ}\right)^2}\,du=\int_{R_i}^{R}\sqrt{1+\left(\frac{dZ}{dR}\right)^2}\,du \qquad (2)$$

In the equations which follow, the path coordinate S and angular coordinate θ are used as independent spatial variables. The coordinates Z,R defining the impeller surface are expressed as parametric functions of S, i.e., $Z(S)$, $R(S)$. The length of the leakage path along the impeller face is defined by

$$L_s=\int_{Z_i}^{Z_i+L}\sqrt{1+\left(\frac{dR}{dZ}\right)^2}\,du \qquad (3)$$

Trigonometric functions of the angle γ, illustrated in Fig. 3, are defined as follows

$$\tan\gamma=-\frac{dR}{dZ},\quad \cos\gamma=\frac{dZ}{dS},\quad \sin\gamma=-\frac{dR}{dS} \qquad (4)$$

The clearance between the impeller and the housing is denoted as $H(S,\theta,t)$, with the time dependency introduced by impeller motion. In the centered position, the clearance function depends only on S and is denoted by $H_o(S)$. Displacement of the impeller in the Z direction by the differential Δ yields

$$H(S,\theta,t)=H_o(S)-\Delta(t)\sin\gamma=H_o(S)+\Delta(t)\frac{dR}{dS} \qquad (5)$$

Governing Equations

Returning to Fig. 2, the path coordinate S and circumferential coordinate $R\theta$ are used to locate a fluid differential element of thickness $H(S,\theta,t)$. From Childs (1987), the continuity equation can be stated

$$\frac{\partial H}{\partial t}+\frac{\partial}{\partial S}(U_sH)+\frac{1}{R}\frac{\partial}{\partial\theta}(U_\theta H)+\left(\frac{H}{R}\right)\frac{\partial R}{\partial S}U_s=0$$

where U_s and U_θ are the path and circumferential bulk-velocity components, respectively. Also from Childs (1987), the path and circumferential momentum equations are stated

$$-H\frac{\partial P}{\partial S}=-\rho H\frac{U_\theta^2}{R}\frac{dR}{dS}+\tau_{ss}+\tau_{sr}+\rho H\left(\frac{\partial U_s}{\partial t}+\frac{\partial U_s}{\partial\theta}\frac{U_\theta}{R}+\frac{\partial U_s}{\partial S}U_s\right)$$

$$-\frac{H}{R}\frac{\partial P}{\partial\theta}=\tau_{\theta s}+\tau_{\theta r}+\rho H\left(\frac{\partial U_\theta}{\partial t}+\frac{\partial U_\theta}{\partial\theta}\frac{U_\theta}{R}+\frac{\partial U_\theta}{\partial S}U_s+\frac{U_\theta U_s}{R}\frac{\partial R}{\partial S}\right)$$

Following Hirs' approach (1973), the wall shear-stress definitions in these equations can be stated

$$\tau_{ss}=\frac{ns}{2}\rho U_s^2R_s^{ms}[1+(U_\theta/U_s)^2]^{\frac{ms+1}{2}}$$

$$\tau_{sr}=\frac{nr}{2}\rho U_s^2R_s^{mr}\{1+[(U_\theta-R\omega)/U_s]^2\}^{\frac{mr+1}{2}} \qquad (6)$$

$$\tau_{\theta s}=\frac{ns}{2}\rho U_\theta U_sR_s^{ms}[1+(U_\theta/U_s)^2]^{\frac{ms+1}{2}}$$

$$\tau_{\theta r}=\frac{nr}{2}\rho U_s(U_\theta-R\omega)R_s^{mr}\{1+[(U_\theta-R\omega)/U_s]^2\}^{\frac{mr+1}{2}}$$

where

$$R_s=2HU_s/\nu \qquad (7)$$

Nondimensionalization and Perturbation Analysis

The governing equations define the bulk-flow velocity components (U_s, U_θ) and the pressure P as a function of the coordinates ($R\theta$, S) and time, t. They are conveniently nondimensionalized by introducing the following variables

$$\begin{aligned} u_s&=U_s/V_i, & u_\theta&=U_\theta/R_i\omega, & p&=P/\rho V_i^2\\ h&=H/C_i, & s&=S/L_s, & r&=R/R_i\\ \tau&=\omega t, & b&=V_i/R_i\omega, & T&=L_s/V_i \end{aligned} \qquad (8)$$

The objective of the present analysis is to examine the changes in (u_s, u_θ, p) due to changes in the clearance function $h(\theta,s,t)$ caused by small axial motion of the impeller within its housing. To this end, the governing equations are expanded in the perturbation variables

$$\begin{aligned} u_s&=u_{so}+\epsilon u_{s1}, & h&=h_o+\epsilon h_1\\ u_\theta&=u_{\theta o}+\epsilon u_{\theta 1}, & p&=p_o+\epsilon p_1 \end{aligned} \qquad (9)$$

where $\epsilon=e/C_i$ is the perturbation parameter. The following equations result:

Zeroth-Order Equations

(*a*) Path-Momentum Equation

$$\frac{dp_o}{ds}-\frac{1}{r}\left(\frac{dr}{ds}\right)\frac{u_{\theta o}^2}{b^2}+\left[\left(\frac{\sigma_r+\sigma_s}{2}\right)-\frac{1}{h_o}\frac{dh_o}{ds}-\frac{1}{r}\frac{dr}{ds}\right]u_{so}^2=0 \qquad (10a)$$

(*b*) Circumferential-Momentum Equation

$$\frac{du_{\theta o}}{ds}+\frac{u_{\theta o}}{r}\frac{dr}{ds}+[\sigma_r(u_{\theta o}-r)+\sigma_su_{\theta o}]/2=0 \qquad (10b)$$

(*c*) Continuity Equation

$$rh_ou_{so}=1 \qquad (10c)$$

The continuity equation has been used to eliminate $\frac{du_{so}}{ds}$ from equation (10*a*). The momentum equations define the pressure and velocity distributions for a centered impeller position. They are coupled and nonlinear and must be solved iteratively. The initial condition for $u_{\theta o}(0)$ is obtained from the exit flow condition of the impeller. The inlet and discharge pressure of the impeller are known and serve, respectively, as the exit (P_e) and supply (P_s) pressures for the leakage flow along the impeller face. The inlet condition for p_o is obtained from the inlet relationship

$$P_s-P_o(0,\theta,t)=\rho(1+\xi)U_{so}^2(0,\theta,t)/2 \qquad (11)$$

From this relationship, the zeroth-order pressure relationship is

$$p_o(0)=P_s/\rho V_i^2-(1+\xi)u_{so}^2(0)/2 \qquad (12)$$

The wear-ring seal at the leakage-path exit also provides a restriction, yielding a relationship of the form

$$P(L_s,\theta,t)-P_e=\frac{\rho}{2}C_{de}U_s^2(L_s,\theta,t) \qquad (13)$$

First-Order Equations

(*a*) Path-Momentum Equation

$$\frac{\partial p_1}{\partial s}+u_{\theta 1}A_{2s}+u_{s1}A_{3s}+\left[\omega T\frac{\partial u_{s1}}{\partial\tau}+\omega T\frac{u_{\theta o}}{r}\frac{\partial u_{s1}}{\partial\theta}+u_{so}\frac{\partial u_{s1}}{\partial s}\right]=h_1A_{1s} \qquad (14a)$$

(*b*) Circumferential-Momentum Equation

$$b\frac{L_s}{R_i}\frac{1}{r}\frac{\partial p_1}{\partial\theta}+u_{\theta 1}A_{2\theta}+u_{s1}A_{3\theta}+\left[\omega T\frac{\partial u_{s1}}{\partial\tau}+\omega T\frac{u_{\theta o}}{r}\frac{\partial u_{s1}}{\partial\theta}+u_{so}\frac{\partial u_{s1}}{\partial s}\right]=h_1A_{1\theta} \qquad (14b)$$

(*c*) Continuity Equation

$$\frac{\partial u_{s1}}{\partial s}+\frac{\omega T}{r}\frac{\partial u_{\theta 1}}{\partial\theta}+u_{s1}\left(\frac{1}{r}\frac{dr}{ds}+\frac{1}{h_o}\frac{dh_o}{ds}\right)=+\frac{h_1u_{so}}{h_o^2}\frac{dh_o}{ds}-\frac{1}{h_o}\left(u_{so}\frac{\partial h_1}{ds}+\omega T\frac{u_{\theta o}}{r}\frac{\partial h_1}{\partial\theta}+\omega T\frac{\partial h_1}{\partial\tau}\right) \qquad (14c)$$

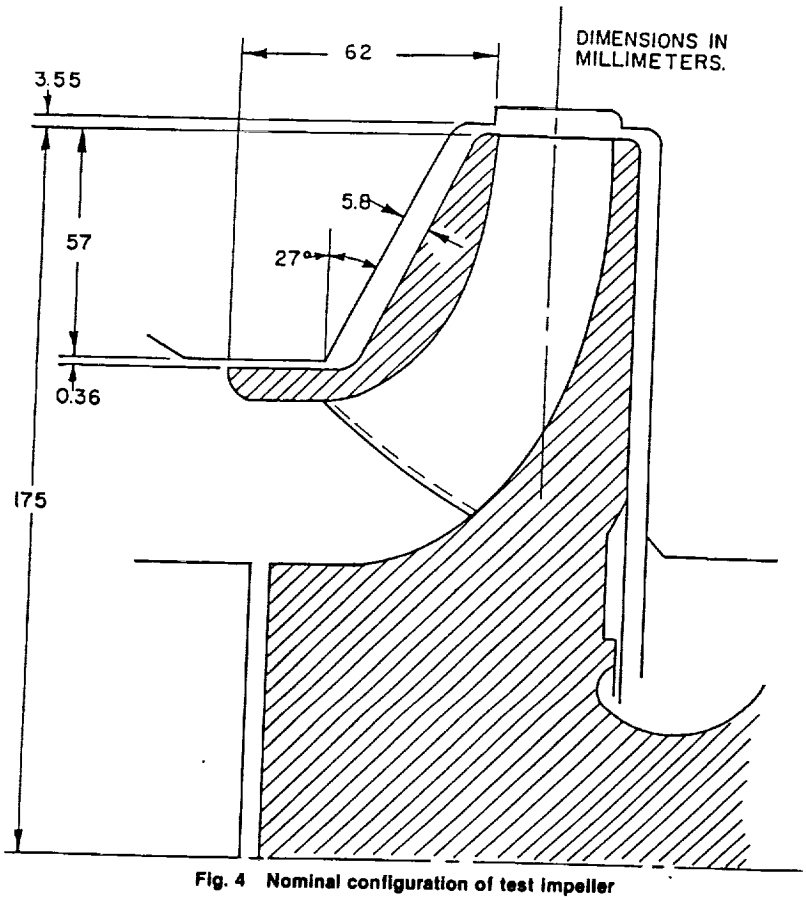

Fig. 4 Nominal configuration of test impeller

Most of the parameters of these equations are defined in Appendix A. The quantities σ_s and σ_r are defined by

$$\sigma_s = (L_s/H_o)\lambda_s, \quad \sigma_r = (L_s/H_o)\lambda_r \tag{15}$$

where λ_s and λ_r are dimensionless stator and rotor friction factors defined by

$$\lambda_s = nsR_{so}^{ms}[1 + (u_{\theta o}/bu_{so})^2]^{\frac{ms+1}{2}}$$

$$\lambda_r = nrR_{so}^{mr}\{1 + [(u_{\theta o} - r)/bu_{so}]^2\}^{\frac{mr+1}{2}}$$

From equations (5) and (8), the perturbation clearance function is

$$h_1 = \frac{\delta}{\epsilon}\left(\frac{R_i}{L_s}\right)\frac{dr}{ds}, \quad \delta = \frac{\Delta}{C_i} \tag{16}$$

Hence,

$$\frac{\partial h_1}{\partial s} = \frac{\delta}{\epsilon}\left(\frac{R_i}{L_s}\right)\frac{d^2r}{ds^2}, \quad \frac{\partial h_1}{\partial \theta} = 0$$

First-Order Equation Solutions. For axial excitation, the θ partial derivatives of equations (14) are eliminated. The time variation can be eliminated by assuming the following harmonic solutions for the clearance excitation

$$\delta = \delta_0 e^{j\Omega t} = \delta_0 e^{jf\tau} \tag{17}$$

and dependent variables

$$p_1 = \bar{p}_1 e^{jf\tau}, \quad u_{s1} = \bar{u}_{s1} e^{jf\tau}, \quad u_{\theta 1} = \bar{u}_{\theta 1} e^{jf\tau} \tag{18}$$

where

$$f = \Omega/\omega, \quad \omega t = \tau \tag{19}$$

Note that $\bar{p}_1$, $\bar{u}_{s1}$, and $\bar{u}_{\theta 1}$ are now complex variables. Substitution into equations (14) yields

$$\frac{d}{ds}\begin{Bmatrix}\bar{u}_{s1}\\ \bar{u}_{\theta 1}\\ \bar{p}_1\end{Bmatrix} + [A]\begin{Bmatrix}\bar{u}_{s1}\\ \bar{u}_{\theta 1}\\ \bar{p}_1\end{Bmatrix} = \left(\frac{\delta_o}{\epsilon}\right)\begin{Bmatrix}g_1\\ g_2\\ g_3\end{Bmatrix} \tag{20}$$

where

$$[A] = \begin{bmatrix} B & 0 & 0 \\ A_{3\theta}/u_{so} & (A_{2\theta} + j\Omega T)/u_{so} & 0 \\ A_{3s} - u_{so}B + j\Omega T & A_{2s} & 0 \end{bmatrix} \tag{21}$$

$$\begin{Bmatrix}g_1\\ g_2\\ g_3\end{Bmatrix} = \left(\frac{R_i}{L_s}\right)\begin{Bmatrix} -F_2 + j\dfrac{\Omega T}{ho}\dfrac{dr}{ds} \\ -\left(\dfrac{A_{1\theta}}{u_{so}}\right)\dfrac{dr}{ds} \\ A_{1s}\dfrac{dr}{ds} + u_{so}F_2 + ju_{so}\dfrac{\Omega T}{h_o}\dfrac{dr}{ds}\end{Bmatrix} \tag{22}$$

and

$$F_2 = \frac{u_{so}}{h_o}\left(\frac{d^2r}{ds^2} - \frac{1}{h_o}\frac{dh_o}{ds}\frac{dr}{ds}\right), \quad B = \frac{1}{r}\frac{dr}{ds} + \frac{1}{h_o}\frac{dh_o}{ds} \tag{23}$$

The following three boundary conditions are specified for the solution of equation (20):

(*a*) The entrance-perturbation, circumferential velocity is zero, i.e.,

$$\bar{u}_{\theta 1}(0) = 0 \tag{24a}$$

(*b*) The entrance loss at the seal entrance is defined by equation (11), and the corresponding perturbation-variable relationship is

$$\bar{p}_1(0) = -(1 + \xi)\bar{u}_{s1}(0) \tag{24b}$$

(*c*) The relationship at the exit is provided by equation (13) and yields the following perturbation relationship

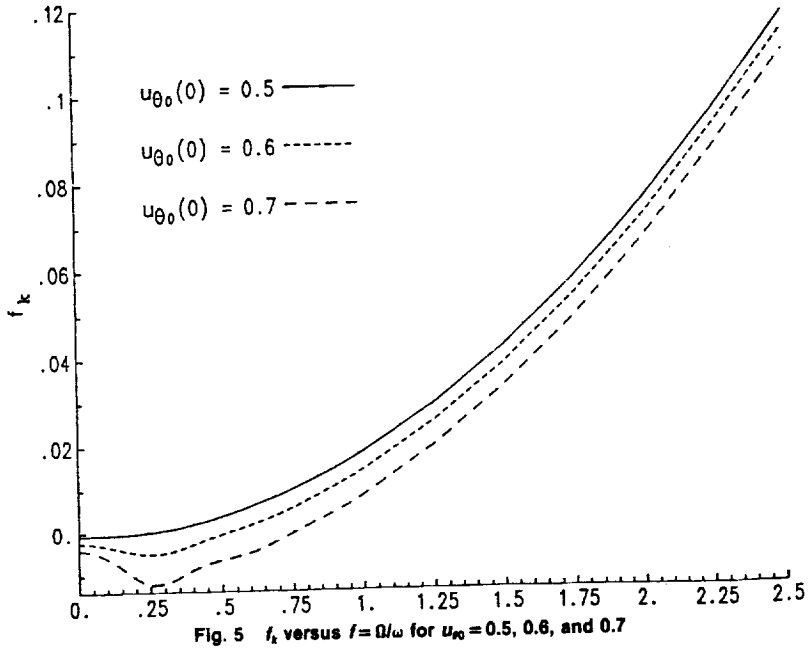

Fig. 5 f_k versus $f = \Omega/\omega$ for $u_{\theta 0} = 0.5$, 0.6, and 0.7

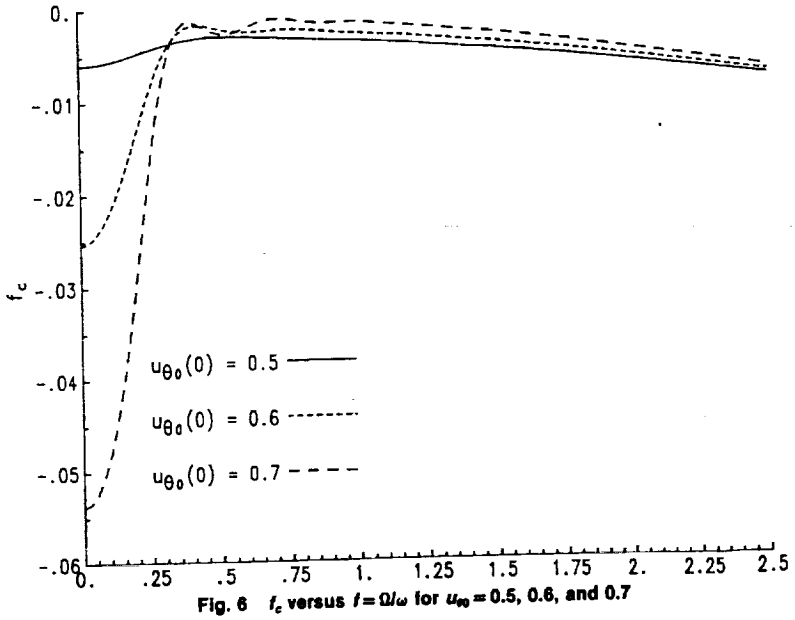

Fig. 6 f_c versus $f = \Omega/\omega$ for $u_{\theta 0} = 0.5$, 0.6, and 0.7

Table 1 Zeroth-order-solution results; $C_l = 3.5$ mm

$u_{\theta 0}(0)$	0.5	0.6	0.7
C_{de}	1.655	1.690	1.731
$\dot{m}$ (kg/sec)	4.784	4.391	3.973
$F_o \times 10^{-4}(N)$	2.25	2.15	2.04

Table 2 Asymptotic coefficients from Figs. 5 and 6

$u_{\theta 0}$ –	$K_a \times 10^{-4}$ N/m	M_a Kg	$C_a \times 10^2$ Kg
0.5	.648	5.61	.809
0.6	6.06	5.63	.911
0.7	13.6	5.68	1.05

$$\tilde{p}_1(1) = C_{de} u_{so}(1) \tilde{u}_{s1}(1) \tag{24c}$$

The value for C_{de} depends on the wear-ring seal geometry. Solution of equation (20) for the boundary conditions of equations (24) is relatively straightforward using a transition-matrix approach (Meirovitch, 1986). The solution can be stated

$$\begin{Bmatrix} \tilde{u}_{s1} \\ \tilde{u}_{\theta 1} \\ \tilde{p}_1 \end{Bmatrix} = \left(\frac{\delta_o}{\epsilon}\right) \begin{Bmatrix} f_{1c} + jf_{1s} \\ f_{2c} + jf_{2s} \\ f_{3c} + jf_{3s} \end{Bmatrix} = \left(\frac{\delta_o}{\epsilon}\right) \begin{Bmatrix} f_1 \\ f_2 \\ f_3 \end{Bmatrix} \tag{25}$$

Reaction Force. From Fig. 4, the axial differential force component on a differential-impeller surface area can be stated

$$dF_Z = -(P\sin\gamma + \tau_{rs}\cos\gamma) R d\theta dS \tag{26}$$

The zeroth and first-order force components are obtained by substituting for P and τ_{rs} in equation (26). From equation (6), the perturbation shear stresses can be stated

$$\tau_{sr1} = \rho V_i^2 (B_{s1} u_{s1} + B_{s2} u_{\theta 1} + B_{s3} h_1) \tag{27}$$

The coefficients of these equations are defined in the appendix.

The zeroth and first-order forces are defined by

$$F_{Z0} = 2\pi R_i^2 \int_o^1 \left[\rho V_i^2 \frac{dr}{ds} P_0 + \left(\frac{L}{R_i}\right) \frac{dz}{dr} \tau_{rs0} \right] rds \tag{28}$$

and

$$F_{Z1} = F_{Z1k} + jF_{Z1c} = F_0(f_k + jff_c)\delta_0 \tag{29}$$

where

$$F_0 = \pi R_i^2 \Delta P = \pi R_i^2 C_{d0} \rho V_i^2 \tag{30}$$

$$f_k = \frac{2}{C_d} \int_0^1 \left[f_{3c} \frac{dr}{ds} + \left(\frac{L}{R_i}\right) B_{s1} f_{1c} + \left(\frac{L}{R_i}\right) B_{s2} f_{2c} - \left(\frac{L^2}{RL_s}\right) B_{s3} \frac{dz}{ds} \right] rds \tag{31}$$

$$ff_c = \frac{2}{C_d} \int_0^1 \left[f_{3s} \frac{dr}{ds} + \left(\frac{L}{R_i}\right) B_{s1} f_{1s} + \left(\frac{L}{R_i}\right) B_{s2} f_{2s} \right] rds$$

Numerical Results. Figure 4 illustrates the pump-impeller and shroud geometry used by Bolleter et al. (1987) in their test program for radial force coefficients. Their pump uses a vaned diffuser. Their tests were at best efficiency point (BEP) with the pump running at 2000 rpm, while developing 68m of head and 130 l/sec of flow rate. The impeller has seven blades and an impeller exit angle of 22.5 deg. The test fluid is water at 80°F. For the present study, ΔP across the impeller is assumed to be 70 percent of the total head rise of the stage. Based on pitot-tube measurements, impeller exit tangential velocity is about 50 percent of the impeller discharge surface velocity; hence, $u_{\theta 0}(0) = 0.5$.

Both walls of the annulus are assumed to be smooth and represented by Yamada's (1962) test data; $mr = ms = -0.25$, $nr = ns = 0.079$. The inlet loss for the annulus, ξ, is assumed to be 0.1. The discharge coefficient for the seal is calculated iteratively as follows. With an assumed C_{de}, equations (10), (11), and (12) were used to calculate the leakage through the impeller annulus and the pressure and tangential-velocity upstream of the seal. The seal is then analyzed (with the same equations) using the calculated seal inlet pressure and tangential velocity to determine leakage and C_{de}. The iteration continues until the leakage predictions for the exit seal and the impeller annulus agree. Table 1 provides zeroth-order solutions.

Figures 5 and 6 illustrate f_k and f_c versus f for $u_{\theta 0}(0) = 0.5$, 0.6, and 0.7. The $u_{\theta 0}(0) = 0.5$ curves are comparatively smooth; the $u_{\theta 0}(0) = 0.6$, 0.7 curves show evidence of fluid resonances similar to those obtained earlier by Childs (1987). Specifically, in the absence of fluid resonances, the expected results for f_k would be a parabola without the predicted fluctuation in the neighborhood of $f = 0.25$. Further, the expected result for f_c would be a constant without the low-frequency fluctuations.

The functions f_k, f_c are nondimensionalized frequency-dependent stiffness and damping coefficients. To develop a physical model for the axial reaction forces defined by these curves, the $f_k(f)$ curves will be reviewed first. All of the f_k curves demonstrate a quadratic asymptote with the following frequency-domain model

$$f_{ka}(f) = -\bar{K} + \bar{M}f^2, \tag{32}$$

which implies the time-domain reaction-force model

$$F_{k1a} = -(K_a Z_r + M_a \ddot{Z}_r) \tag{33}$$

where

$$K_a = \bar{K}F_o/C_i, \; M_a = \bar{M}F_o/C_i\omega^2 \tag{34}$$

The physical coefficients obtained from a curve fit of the asymptotic solutions in Fig. 5 yield the physical coefficients of Table 2.

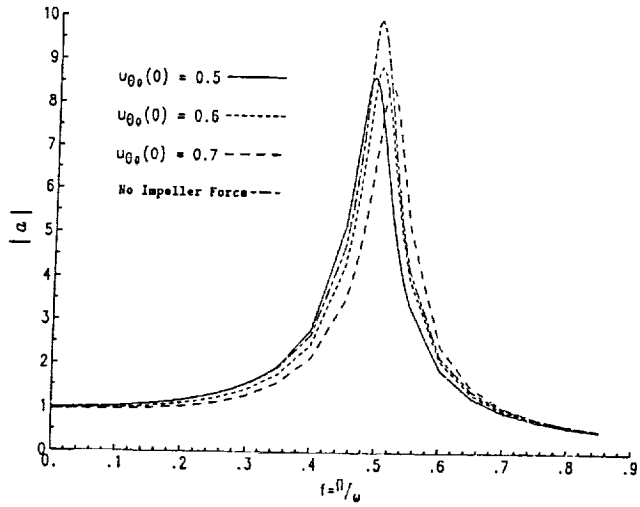

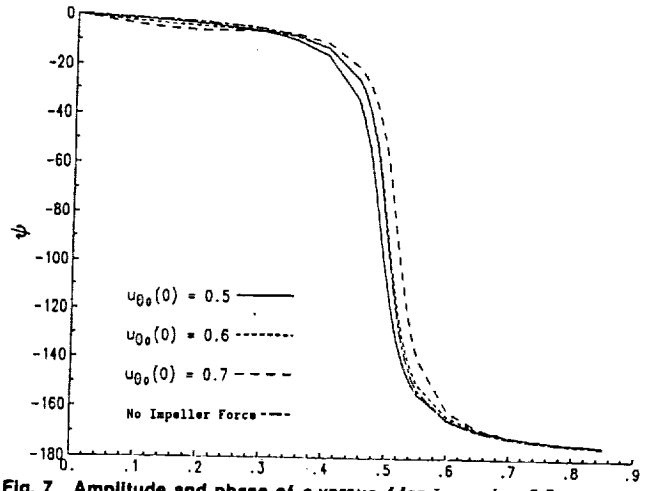

Fig. 7 Amplitude and phase of a versus f for $\bar{\omega}_n = \omega_n/\omega = 0.5$; $u_{\theta 0} = 0.5$, 0.6, and 0.7

The stiffness values are negligibly small in comparison to the axial stiffness which would center the pump rotor either through a thrust bearing or balance-piston arrangements. The mass coefficient is small but appreciable in comparison to the impeller mass. This "added mass" contribution to the impeller rotor has not previously been accounted for in axial vibration analyses of pumps.

The f_c curves of Fig. 6 can be viewed as nondimensionalized frequency-dependent damping coefficients. The asymptotic behavior of these curves (for high values of f) shows an unexpected, approximately-linear, increase in damping with increasing frequency. The asymptotic results are curvefitted by the linear model

$$f_c(f) = \bar{C}_o - \bar{C}f \tag{35}$$

The linear dependence of f_c on $\bar{C}$ yields the time-domain reaction-force model

$$F_{ca} = -C_a \Omega_a \dot{Z}_r, \; \Omega_a = |\ddot{Z}_r/Z_r|^{1/2} \tag{36}$$

where

$$C_a = \bar{C}F_o/C_i\omega^2$$

Values of C_a are provided in Table 2. Physically meaningful values for damping are obtained by multiplying C_a by Ω, e.g., the nominal damping value for $\Omega = \omega = 209$ *rd/sec* is about 209 *N sec/m* (1.2 *lb sec/in*) which is significant.

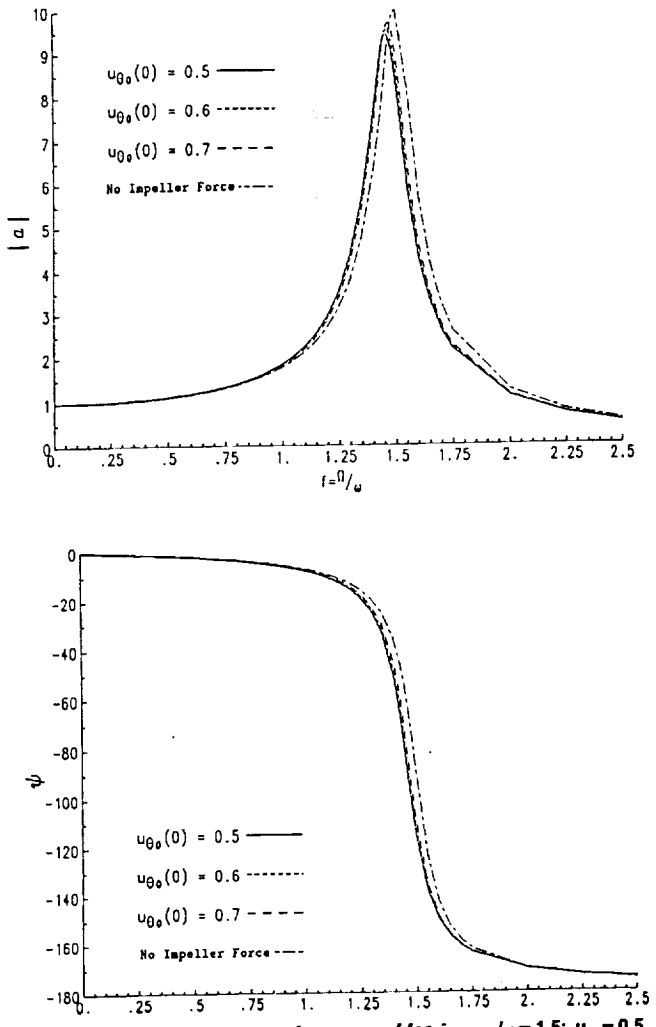

Fig. 8 Amplitude and phase of a versus f for $\bar{\omega}_n = \omega_n/\omega = 1.5$; $u_{\theta 0} = 0.5$, 0.6, and 0.7

Modeling Annular Forces for Axial-Vibration Analysis. The transient model for axial vibrations, including the impeller forces, can be stated

$$M_{zo}\ddot{Z}_r + (C_{zo} - F_c)\dot{Z}_r + (K_{zo} - F_k)Z_r = F_e(t) \tag{37}$$

where M_{zo}, C_{zo}, and K_{zo} are the nominal mass, damping, and stiffness coefficients, $F_e(t)$ is the external excitation force, and

$$F_c(f_a) = f_c(f_a)F_o/C_i\omega;\ F_k(f_a) = f_k(f_a)F_o/C_i \tag{38}$$
$$f_a = \Omega_a/\omega$$

The model of equation (2) has moved the impeller-shroud reaction force from the right-hand side of the equation to the left-hand side of the equation. The force is now modeled as frequency-dependent stiffness and damping coefficients, which combine directly with the nominal, mechanical, stiffness and damping coefficients.

For an external harmonic excitation force of the form $F_e = F_{eo}e^{j\Omega t}$, the steady-state solution $Z_{rss} = Ae^{j\Omega t}$ is defined by

$$a = |a|e^{j\psi} = A/(F_{eo}/K_{zo})$$
$$= \bar{\omega}_n^2/\{[\bar{\omega}_n^2(1 - \bar{f}_k) - f^2] + jf\bar{\omega}_n(2\zeta - \bar{f}_c\bar{\omega}_n)\} \tag{39}$$

where

$$\omega_n^2 = K_{zo}/M_{zo};\ 2\zeta\omega_n = C_{zo}/M_{zo} \tag{40}$$
$$\bar{\omega}_n = \omega_n/\omega;\ \bar{f}_c = \frac{f_c}{C_i}\left(\frac{F_o}{K_{zo}}\right);\ \bar{f}_k = \frac{f_k}{C_i}\left(\frac{F_o}{K_{zo}}\right)$$

The physical example used to demonstrate the solution of equation (39) is a double-suction single-stage pump with the impeller of Fig. 4 and the following physical data:

$$M_{zo} = 100\ kg,\ \zeta = 0.05,\ \omega = 2000\ rpm = 209\ rd/sec$$

With a double-suction design, the reaction force from the impeller face is doubled. Figures 7 and 8 illustrate solutions to equation (39) for $\bar{\omega}_n = 0.5$ and 1.5 times the running speed for no impeller forces and impeller forces corresponding to $u_{\theta 0}(0) = 0.5$, 0.6, and 0.7. The magnitude and phase of a are presented and demonstrate that the impeller forces provide a modest amount of additional damping and slightly displace the peak-amplitude-frequency location. Although not presented here, the impeller forces did cause significant changes in the steady state response when $\bar{\omega}_n$ was reduced to unrealistically low values on the order of 0.1.

Summary and Conclusions

An analysis has been developed and predictions presented for the axial forces developed on a pump impeller shroud. The force coefficients are reduced to frequency-dependent stiffness and damping coefficients. Fluid resonances are evident in these results comparable to the rotordynamic-coefficient analysis results of Childs (1987). The asymptotic expansion of these coefficients yield negligible stiffness values and small but appreciable added mass and damping coefficients.

Frequency-response analysis of a double-suction single-stage pump impeller indicates that the impeller shroud forces provide a little additional damping and can modestly move the damped natural frequency of the system for pumps with axial natural frequencies on the order of 0.5 to 1.5 times the running speed. The impeller-shroud forces can only become really significant for natural frequencies that are much lower than the running speed, viz., one tenth of the running speed or lower.

Acknowledgment

The results reported herein were funded in part by NASA Marshall Space Flight Center, NASA Contract NAS 8-37821; Contract Monitor: James Cannon.

References

Bolleter, U., Wyss, A., Welte, I., and Sturchler, R., 1987, "Measurement of Hydrodynamic Matrices of Boiler Feed Pump Impellers," ASME JOURNAL OF VIBRATIONS, STRESS, AND RELIABILITY IN DESIGN, Vol. 109, pp. 144-151.

Childs, D. W., 1987, "Fluid Structure Interaction Forces at Pump-Impeller-Shroud Surfaces for Rotordynamic Calculations," *Rotating Machinery Dynamics*, Vol. 2, ASME, pp. 581-593.

Childs, D. W., 1989, "Fluid Structure Interaction Forces at Pump-Impeller-Shroud Surfaces for Rotordynamic Calculations," ASME JOURNAL OF VIBRATION, ACOUSTICS, STRESS, AND RELIABILITY IN DESIGN, Vol. 111, pp. 216-225.

Lobanoff, V. S., and Ross, R. K., 1985, *Centrifugal Pumps, Design and Applications*, Gulf Publishing.

Meirovitch, L., 1985, *Introduction to Dynamics and Control*, J. Wiley.

Thomae, H., and Stucki, R., 1970, "Axial Thrust in Centrifugal Pumps," *Sulzer Technical Review*, No. 3.

Yamada, Y., 1962, "Resistance of Flow Through an Annulus with an Inner Rotating Cylinder," Bull. JSME, Vol. 5, No. 18, pp. 302-310.

APPENDIX A

Perturbation Coefficients

$$A_{1s} = [\sigma_s(1 - ms) + \sigma_r(1 - mr)]u_{so}^2/2h_o$$

$$A_{2s} = -\frac{2u_{\theta o}}{r}\frac{dr}{ds}/b^2 + [\sigma_r(mr + 1)\beta_o + \sigma_s(ms + 1)\beta_1]u_{so}/2$$

$$A_{3s} = \frac{du_{so}}{ds} + [(2 + mr)\sigma_r + (2 + ms)\sigma_s]u_{so}/2$$
$$- [(1 + mr)\sigma_r\beta_o(u_{\theta o} - r) + (1 + ms)\sigma_s\beta_1 u_{\theta o}]/2$$
$$2A_{1\theta} = u_{so}[(1 - mr)(u_{\theta o} - r)\sigma_r + (1 - ms)u_{\theta o}\sigma_s]/h_o$$

$$2A_{2\theta} = u_{so}(\sigma_r + \sigma_s) + \sigma_r(mr+1)(u_{\theta o} - r)\beta_o + \sigma_s(ms+1)u_{\theta o}\beta_1 + 2\frac{u_{so}}{r}\frac{dr}{ds}$$

$$2A_{3\theta} = \sigma_r(u_{\theta o} - r)[mr - (1+mr)\beta_o(u_{\theta o} - r)/u_{so}] + \sigma_s u_{\theta o}[ms - (1+ms)\beta_1 u_{\theta o}/u_{so}]$$

$$\beta_o = (u_{\theta o} - r)/b^2 u_{so}\{1 + [(u_{\theta o} - r)/bu_{so}]^2\}$$

$$\beta_1 = u_{\theta o}/b^2 u_{so}[1 + (u_{\theta o}/bu_{so})^2]$$

$\tau_{r\theta}$ Perturbation Coefficients

$$B_{\theta 1} = \lambda_r(1+mr)(u_{\theta o} - r)[1 - \beta_o(u_{\theta o} - r)/u_{so}]/2b$$

$$B_{\theta 2} = \lambda_r[u_{so} + (1+mr)(u_{\theta o} - r)\beta_o]/2b$$

$$B_{\theta 3} = \lambda_r mr(u_{\theta o} - r)u_{so}/2bh_o$$

τ_{rs} Perturbation Coefficients

$$B_{s1} = \lambda_r[(2+mr)u_{so} - (1+mr)\beta_o(u_{\theta o} - r)/2]$$

$$B_{s2} = \lambda_r(1+mr)\beta_o u_{so}/2$$

$$\beta_{s3} = \lambda_r mru_{so}^2/2h_o$$

Childs, D.
(1991b)

Reprinted from April 1991, Vol. 113, Journal of Vibration and Acoustics

Centrifugal-Acceleration Modes for Incompressible Fluid in the Leakage Annulus Between a Shrouded Pump Impeller and Its Housing

D. W. Childs
Turbomachinery Laboratories,
Mechanical Engineering Department,
Texas A&M University,
College Station, TX 77843

An analysis is presented for the perturbed flow in the leakage path between a shrouded-pump impeller and its housing. A bulk-flow model is used for the analysis consisting of the path-momentum, circumferential-momentum, and continuity equations. Shear stress at the impeller and housing surfaces are modeled according to Hirs' turbulent lubrication model. The governing equations have been used earlier to examine rotordynamic reaction forces developed by lateral and axial impeller motion.

A perturbation expansion of the governing equations in the eccentricity ratio yields a set of zeroth and first-order governing equations. The zeroth-order equations define the leakage rate, and the velocity and pressure distributions for a centered impeller position. The first-order equations define the perturbations in the velocity and pressure distributions due to axial or lateral motion of the impeller. Prior analyses by the author of the perturbation equation have examined the reaction forces on the shroud due to rotor motion. These analyses have produced "resonance" phenomena associated with the centrifugal-acceleration body forces in the fluid field.

In the present analysis, an algorithm is developed and demonstrated for calculating the complex eigenvalues and eigenvectors associated with these resonances. First- and second-natural-frequency eigensolutions are presented for mode shapes corresponding to lateral excitation. First-natural-frequency eigensolutions are also presented for mode shapes corresponding to axial excitation.

Introduction

Figure 1 illustrates an impeller stage of a multistage centrifugal pump. Leakage along the front side of the impeller, from impeller discharge to inlet, is restricted by a wear-ring seal, while leakage along the back side is restricted by either an interstage seal or a balance-piston discharge seal. The present analysis considers perturbed flow in the leakage paths between the impeller shroud surface and its housing.

Prior analyses by the author of those annulli have been concerned with lateral (1987, 1989) and axial (1990) reaction forces developed by the impeller shrouds as a consequence of impeller motion. These analyses have been based on "bulk-flow" models which neglect the variation in the dependent variables across the fluid film. The model consists of the path and circumferential momentum equations and the continuity equations.

The analyses cited have yielded force and moment coefficients due to impeller motion but have also predicted "resonance" phenomena, which are caused by the centrifugal-acceleration body forces present in the path momentum equations. In the present analysis, an algorithm is developed and demonstrated for calculating the complex eigenvalues and eigenvectors associated with the fluid resonances.

Geometry and Kinematics

Figure 1 illustrates the annular leakage paths along the front and back sides of a typical shrouded impeller of a multistage centrifugal pump. The present discussion concentrates on the flow and pressure fields within the forward annulus; however, the analysis also applies to the rear annulus. As illustrated in Fig. 2, the outer surface of the impeller is a surface of revolution formed by rotating the curve $R = R(Z)$ about the Z axis. A point on the surface may be located by the coordinates Z, $R(Z),\theta$. The length along the curve $R(Z)$ from the initial point R_i, Z_i to an arbitrary point R,Z is denoted by S and defined by

Contributed by the Technical Committee on Vibration and Sound for publication in the JOURNAL OF VIBRATION AND ACOUSTICS. Manuscript received January 1990.

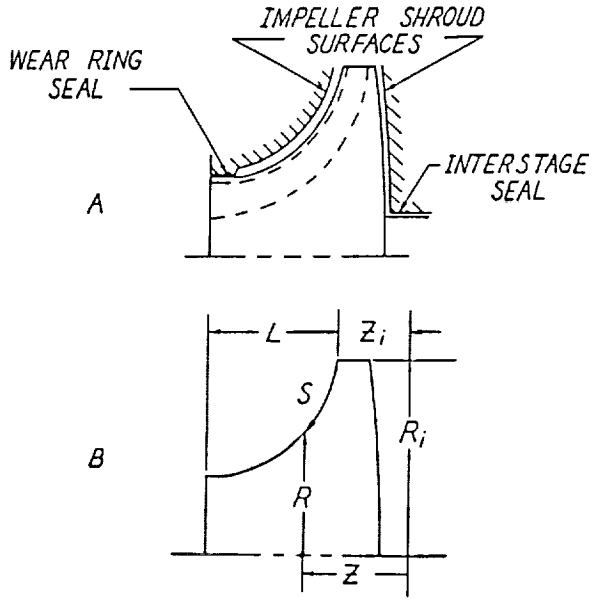

Fig. 1 Impeller stage

$$S=\int_{Z_i}^{Z}\sqrt{1+\left(\frac{dR}{dZ}\right)^2}\,du=\int_{R_i}^{R}\sqrt{1+\left(\frac{dZ}{dR}\right)^2}\,du \qquad (1)$$

In the equations which follow, the path coordinate S and angular coordinate θ are used as independent spatial variables.

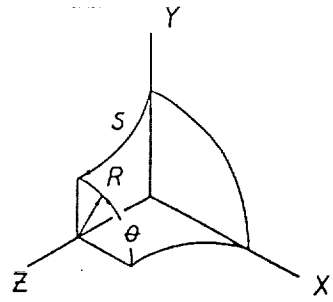

Fig. 2 Impeller surface geometry

The coordinates Z,R defining the impeller surface are expressed as parametric functions of S, i.e., $Z(S),R(S)$. The length of the leakage path along the impeller face is defined by

$$L_s=\int_{Z_i}^{Z_i+L}\sqrt{1+\left(\frac{dR}{dZ}\right)^2}\,du \qquad (2)$$

Trigonometric functions of the angle γ, illustrated in figure 2, are defined as follows

$$\tan\gamma=-\frac{dR}{dZ},\quad \cos\gamma=\frac{dZ}{dS},\quad \sin\gamma=-\frac{dR}{dS} \qquad (3)$$

The clearance between the impeller and the housing is denoted as $H(S,\theta,t)$, with the time dependency introduced by impeller motion. In the centered position, the clearance function depends only on S and is denoted by $H_o(S)$. Displacement

Nomenclature

A_{1s},A_{2s},A_{3s} $A_{1\theta},A_{2\theta},A_{3\theta}$ = coefficients introduced in equation (14) and defined in the appendix

C_{de} = discharge coefficient for the exit wearing seal, introduced in equation (13)

C_i = initial ($s=0$) radial clearance (L)

C_r = exit seal clearance (L)

$f=\Omega/\omega$ = dimensionless excitation frequency

f_k,f_c = nondimensional stiffness and damping coefficients for the impeller corresponding to axial motion at the nondimensional frequency $f=\Omega/\omega$

$frq,f\theta q$ = nondimensional, radial, and circumferential impeller-force coefficients corresponding to a circular orbit at the nondimensional frequency $f=\Omega/\omega$

$h=H/C_i$ = nondimensionalized clearance

H = clearance between impeller shroud and housing (L)

L_s = leakage-path length, defined by equation (2), (L)

$p=P/\rho V_i^2$ = nondimensionalized static fluid pressure

P = fluid static pressure (F/L^2)

$r=R/R_i$ = nondimensionalized radial coordinate

R = radial coordinate (L)

R_i = initial ($s=o$) radius (L)

$R_s=2HU_s/\nu$ = path-velocity Reynolds number

$s=S/L_s$ = nondimensionalized path length

S = path coordinate introduced in equation (1), (L)

$T=L_s/V_i$ = representative transit time for fluid traversing the leakage path (T)

$u_s=U_s/V_i$ = nondimensionalized path fluid velocity

$u_\theta=U_\theta/R_i\omega$ = nondimensionalized circumferential fluid velocity

V_i = initial ($s=0$) rotor velocity

$\alpha=\sigma+j\omega_d$ = dimensionless complex eigenvalue for fluid mode

ϵ = perturbation coefficient

ω = pump running speed (T^{-1})

Ω = excitation frequency (T^{-1})

ρ = fluid density (M/L^3)

θ = circumferential coordinate

σ_r,σ_s = normalized friction factors, defined by equation (15)

$\tau=\omega t$ = nondimensionalized time

ξ = entrance-loss coefficient introduced in equation (11)

Δ = axial impeller displacement (L)

$\sigma=\zeta\omega_n$ = dimensionless real part of complex eigenvalue for fluid mode

ζ = damping factor from complex eigenvalue

$\omega_d=\omega_n\sqrt{1-\zeta^2}$ = dimensionless imaginary part of complex eigenvalue for fluid mode (damped natural frequency)

ω_n = dimensionless undamped natural frequency from complex eigenvalue

of the impeller in the X and Y directions obviously causes a change in the clearance function, as does a change in the axial position defined by $\Delta(t)$. For small displacements and rotations of the impeller, the clearance function can be stated

$$H(S,\theta,t) = H_o(s) - X\cos\theta - Y\sin\theta - \Delta\sin\gamma \tag{4}$$

Observe in this equation that H_o and $\sin\gamma$ are solely functions of S, while X, Y, and Δ are functions only of t.

The clearance function provides the excitation for the reaction forces developed in earlier analyses. Its importance for the present study concerns the nature of the assumed solution in seeking eigen solutions.

Governing Equations

Returning to Fig. 2, the path coordinate S and circumferential coordinate $R\theta$ are used to locate a fluid differential element of thickness $H(S,\theta,t)$. From Childs (1987), the continuity equation can be stated

$$\frac{\partial H}{\partial t} + \frac{\partial}{\partial S}(U_s H) + \frac{1}{R}\frac{\partial}{\partial \theta}(U_\theta H) + \left(\frac{H}{R}\right)\frac{\partial R}{\partial S}U_s = 0 \tag{5a}$$

where U_s and U_θ are the path and circumferential bulk-velocity components, respectively. The path and circumferential momentum equations are stated

$$-H\frac{\partial P}{\partial S} = \tau_{ss} + \tau_{sr} - \rho H\frac{U_\theta^2}{R}\frac{dR}{dS} + \rho H\left(\frac{\partial U_s}{\partial t} + \frac{\partial U_s}{\partial \theta}\frac{U_\theta}{R} + \frac{\partial U_s}{\partial S}U_s\right) \tag{5b}$$

$$-\frac{H}{R}\frac{\partial P}{\partial \theta} = \tau_{\theta s} + \tau_{\theta r} + \rho H\left(\frac{\partial U_\theta}{\partial t} + \frac{\partial U_\theta}{\partial \theta}\frac{U_\theta}{R} + \frac{\partial U_\theta}{\partial S}U_s + \frac{U_\theta U_s}{R}\frac{\partial R}{\partial S}\right) \tag{5c}$$

Following Hirs' approach (1973), the wall shear-stress definitions in these equations can be stated

$$\tau_{ss} = \frac{ns}{2}\rho U_s^2 R_s^{ms}[1 + (U_\theta/U_s)^2]^{\frac{ms+1}{2}}$$

$$\tau_{sr} = \frac{nr}{2}\rho U_s^2 R_s^{mr}\{1 + [(U_\theta - R\omega)/U_s]^2\}^{\frac{mr+1}{2}} \tag{6}$$

$$\tau_{\theta s} = \frac{ns}{2}\rho U_\theta U_s R_s^{ms}[1 + (U_\theta/U_s)^2]^{\frac{ms+1}{2}}$$

$$\tau_{\theta r} = \frac{nr}{2}\rho U_s(U_\theta - R\omega)R_s^{mr}\{1 + [(U_\theta - R\omega)/U_s]^2\}^{\frac{mr+1}{2}}$$

where

$$R_s = 2HU_s/\nu \tag{7}$$

Nondimensionalization and Perturbation Analysis

The governing equations define the bulk-flow velocity components (U_s, U_θ) and the pressure P as a function of the coordinates ($R\theta$,S) and time, t. They are conveniently nondimensionalized by introducing the following variables

$$\begin{aligned} u_s &= U_s/V_i, \quad & u_\theta &= U_\theta/R_i\omega, \quad & p &= P/\rho V_i^2 \\ h &= H/C_i, & s &= S/l_s, & r &= R/R_i \\ \tau &= \omega t, & b &= V_i/R_i\omega, & T &= L_s/V_i \end{aligned} \tag{8}$$

The objective of the present analysis is to examine the changes in (u_s, u_θ, p) due to changes in the clearance function $h(\theta, s, t)$ caused by small motion of the impeller within its housing. To this end, the governing equations are expanded in the perturbation variables

$$\begin{aligned} u_s &= u_{so} + \epsilon u_{s1}, \quad & h &= h_o + \epsilon h_1 \\ u_\theta &= u_{\theta o} + \epsilon u_{\theta 1}, \quad & p &= p_o + \epsilon p_1 \end{aligned} \tag{9}$$

were $\epsilon = e/C_i$ is the perturbation parameter. The following equations result:

Zeroth-Order Equations

(a) Path-Momentum Equations

$$\frac{dp_o}{ds} - \frac{1}{r}\left(\frac{dr}{ds}\right)\frac{u_{\theta o}^2}{b^2} + \left[\left(\frac{\sigma_r + \sigma_s}{2}\right) - \frac{1}{h_o}\frac{dh_o}{ds} - \frac{1}{r}\frac{dr}{ds}\right]u_{so}^2 = 0 \tag{10a}$$

(b) Circumferential-Momentum Equation

$$\frac{du_{\theta o}}{ds} + \frac{u_{\theta o}}{r}\frac{dr}{ds} + [\sigma_r(u_{\theta o} - r) + \sigma_s u_{\theta o}]/2 = 0 \tag{10b}$$

(c) Continuity Equation

$$rh_o u_{so} = 1 \tag{10c}$$

The quantities σ_s and σ_r are defined by

$$\sigma_s = (L_s/H_o)\lambda_s, \quad \sigma_r = (L_s/H_o)\lambda_r \tag{11}$$

where λ_s and λ_r are dimensionless stator and rotor friction factors defined by

$$\lambda_s = nsR_{so}^{ms}[1 + (u_{\theta o}/bu_{so})^2]^{\frac{ms+1}{2}}$$

$$\lambda_r = nrR_{so}^{mr}\{1 + [(u_{\theta o} - r)/bu_{so}]^2\}^{\frac{mr+1}{2}}$$

The continuity equation has been used to eliminate $\frac{du_{so}}{ds}$ from equation (10a). The momentum equations define the pressure and velocity distributions for a centered impeller position. They are coupled and nonlinear and must be solved iteratively. The initial condition for $u_{\theta o}(0)$ is obtained from the exit flow condition of the impeller. The inlet and discharge pressure of the impeller are known and serve, respectively, as the exit (P_e) and supply (P_s) pressures for the leakage flow along the impeller face. The inlet condition for p_o is obtained from the inlet relationship

$$P_s - P_o(0,\theta,t) = \rho(1 + \xi)U_{so}^2(0,\theta,t)/2$$

From this relationship, the zeroth-order pressure relationship is

$$p_o(0) = P_s/\rho V_i^2 - (1 + \xi)u_{so}^2(0)/2 \tag{12}$$

The wear-ring seal at the leakage-path exit also provides a restriction, yielding a relationship of the form

$$P(L_s,\theta,t) - P_e = \frac{\rho}{2}C_{de}U_s^2(L_s,\theta,t) \tag{13}$$

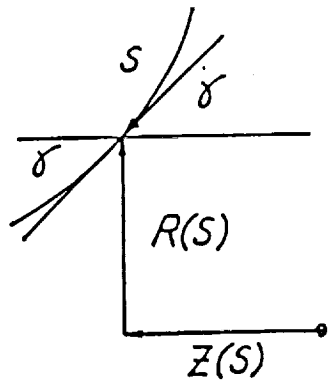

Fig. 3 Local attitude angle of impeller surface

First-Order Equations

(*a*) Path-Momentum Equation

$$\frac{\partial p_1}{\partial s}+u_{\theta 1}A_{2s}+u_{s1}A_{3s}+\left[\omega T\frac{\partial u_{s1}}{\partial \tau}+\omega T\frac{\mu_{\theta o}}{r}\frac{\partial u_{s1}}{\partial \theta}+u_{so}\frac{\partial u_{s1}}{\partial s}\right]=h_1A_{1s} \tag{14a}$$

(*b*) Circumferential-Momentum Equation

$$b\frac{L_s}{R_i}\frac{1}{r}\frac{\partial p_1}{\partial \theta}+u_{\theta 1}A_{2\theta}+u_{s1}A_{3\theta}+\left[\omega T\frac{\partial u_{\theta 1}}{\partial \tau}+\omega T\frac{\mu_{\theta o}}{r}\frac{\partial u_{\theta 1}}{\partial \theta}+u_{so}\frac{\partial u_{\theta 1}}{\partial s}\right]=h_1A_{1\theta} \tag{14b}$$

(*c*) Continuity Equation

$$\frac{\partial u_{s1}}{\partial s}+\frac{\omega T}{r}\frac{\partial u_{\theta 1}}{\partial \theta}+u_{s1}\left(\frac{1}{r}\frac{dr}{ds}+\frac{1}{h_o}\frac{dh_o}{ds}\right)=+\frac{h_1u_{so}}{h_o^2}\cdot\frac{dh_o}{ds}-\frac{1}{h_o}\left(u_{so}\frac{\partial h_1}{ds}+\omega T\frac{\mu_{\theta o}}{r}\frac{\partial h_1}{\partial \theta}+\omega T\frac{\partial h_1}{\partial \tau}\right) \tag{14c}$$

New coefficients in these equations are defined in Appendix A.

Eigen Solutions Corresponding to Lateral Excitation

The first-order equations (14) define the first-order perturbations $u_{s1}(s,\theta,\tau)$, $u_{\theta 1}(s,\theta,\tau)$, and $p(s,\theta,\tau)$ resulting from the perturbed clearance function $h_1(\tau)$. From equations (4) and (8), h_1 can be stated

$$\epsilon h_1=h_{1c}(s,\tau)\cos\theta+h_{1s}(s,\tau)\sin\theta \tag{15}$$

The θ dependency of the dependent variables is eliminated by assuming the comparable, separation-of-variable, solution format

$$\begin{aligned}u_{s1}&=u_{s1c}\cos\theta+u_{s1s}\sin\theta\\ u_{\theta 1}&=u_{\theta 1c}\cos\theta+u_{\theta 1s}\sin\theta\\ p_1&=p_{1c}\cos\theta+p_{1s}\sin\theta\end{aligned} \tag{16}$$

Substituting into equations (14) and equating like coefficients of $\cos\theta$ and $\sin\theta$ yields six equations in the independent variables s,τ. By introducing the complex variables

$$\begin{aligned}\underline{u}_{s1}&=u_{s1c}+ju_{s1s}, & \underline{u}_{\theta 1}&=u_{\theta 1c}+ju_{\theta 1s}\\ \underline{p}_1&=p_{1c}+jp_{1s}, & \underline{h}_1&=h_{1c}+jh_{1s},\end{aligned} \tag{17}$$

these six real equations are reduced to the following three complex equations in s and τ.

$$\frac{\partial \underline{p}_1}{\partial s}+\underline{u}_{\theta 1}A_{2s}+\underline{u}_{s1}A_{3s}+\left[\omega T\frac{\partial \underline{u}_{s1}}{\partial \tau}-j\omega T\frac{\mu_{\theta o}}{r}\underline{u}_{s1}+u_{so}\frac{\partial \underline{u}_{s1}}{\partial s}\right]=\underline{h}_1A_{1s} \tag{18a}$$

$$-j\frac{b}{r}\left(\frac{L_s}{R_i}\right)\underline{p}_1+\underline{u}_{\theta 1}A_{2\theta}+\underline{u}_{s1}A_{3\theta}+\left[\omega T\frac{\partial \underline{u}_{\theta 1}}{\partial \tau}-j\omega T\frac{\mu_{\theta o}}{r}\underline{u}_{\theta 1}+u_{so}\frac{\partial \underline{u}_{\theta 1}}{\partial s}\right]=\underline{h}_1A_{1\theta} \tag{18b}$$

$$\frac{\partial \underline{u}_{s1}}{\partial s}-j\frac{\omega T}{r}\underline{u}_{\theta 1}+\underline{u}_{s1}\left(\frac{1}{r}\frac{dr}{ds}+\frac{1}{h_o}\frac{dh_o}{ds}\right)=\underline{h}_1\left[\frac{u_{so}}{h_o^2}\frac{dho}{ds}+j\frac{\omega T}{h_o}\frac{u_{\theta o}}{r}\right]-\frac{u_{so}}{h_o}\frac{\partial \underline{h}_1}{\partial s}-\frac{\omega T}{h_o}\frac{\partial \underline{h}_1}{\partial \tau} \tag{18c}$$

The time dependency of equations (18) is eliminated by assuming a harmonic solution of the form

$$h_1=h_{10}e^{jf\tau},\ \underline{u}_{s1}=\tilde{u}_{s1}e^{jf\tau},\ \underline{u}_{\theta 1}=\tilde{u}_{\theta 1}e^{jf\tau},\ \underline{p}_1=\tilde{p}_1e^{jf\tau};\ f=\Omega/\omega \tag{19}$$

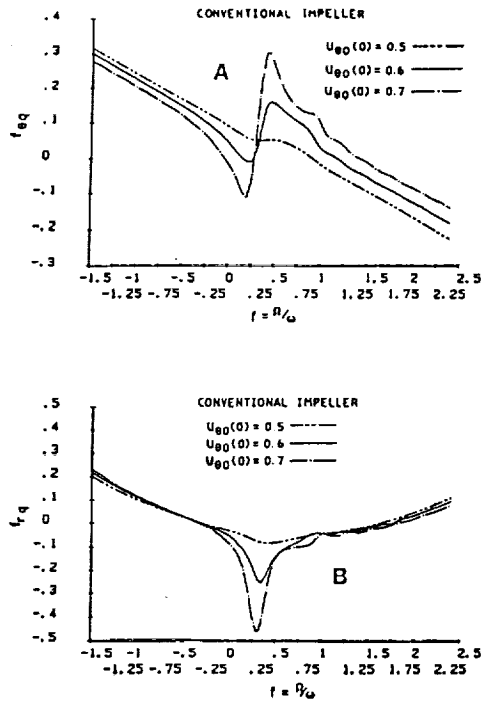

Fig. 4 Nondimensional rotordynamic force coefficients: (*a*) tangential-force coefficient, (*b*) radial-force coefficients

The assumed clearance function $h_1(t)$ correspond to circular orbital motion of the impeller at the precession frequency Ω. Substitution from equation (19) into equation (18) yields the three complex ordinary differential equations in s of the form

$$\frac{d}{ds}\begin{Bmatrix}\tilde{u}_{s1}\\ \tilde{u}_{\theta 1}\\ \tilde{p}_1\end{Bmatrix}+[A]\begin{Bmatrix}\tilde{u}_{s1}\\ \tilde{u}_{\theta 1}\\ \tilde{p}_1\end{Bmatrix}=\left(\frac{q_o}{\epsilon}\right)\begin{Bmatrix}g_1\\ g_2\\ g_3\end{Bmatrix} \tag{20}$$

The parameters q_0, g_1, g_2, and g_3 on the right hand side are defined by Childs (1987). The right hand side is important for the forced solution but irrelevant for eigenanalysis, which concerns the homogeneous solution.

The following three boundary conditions are specified for the solution of equation (20):

(*a*) The entrance-perturbation, circumferential velocity is zero, i.e.,

$$\tilde{u}_{\theta 1}(0)=0 \tag{21a}$$

(*b*) The entrance loss at the seal entrance is defined by equation (12), and the corresponding perturbation-variable relationship is

$$\tilde{p}_1(0)=-(1+\xi)\tilde{u}_{s1}(0) \tag{21b}$$

(*c*) The relationship at the exit is provided by equation (13) and yields the following perturbation relationship

$$\tilde{p}_1(1)=C_{de}u_{so}(1)\tilde{u}_{s1}(1) \tag{21c}$$

The value for C_{de} depends on the wear-ring seal geometry.

Figure 4 illustrates the radial and tangential reaction-force components for solutions to equation (20) from Childs (1989). The three solutions for each frame of the figure correspond to three inlet tangential velocity ratios $u_{\theta 0}(0)$. If the centrifugal acceleration term is dropped from the analysis, the $f_{\theta q}$ curve becomes a straight line and the f_{rq} curve becomes a parabola, which are the expected solutions for liquid, constant-radius, annular seals; Childs and Kim (1985). The sharp deviation from the expected linear and parabolic solution forms for these curves in the "resonance" phenomenon cited in the introduction, and it is eliminated if the centrifugal acceleration term is dropped. The question of interest here is: "If the solutions

of Fig. 4 arise from a 'resonance' of the fluid, how are the associated eigenvalues and eigenvectors to be calculated, and what do the mode shapes look like?"

The first part of the question is answered by reviewing the solution approach to equation (20) which was used in generating the results of Fig 4. Following normal transition-matrix approaches (Meirovitch, 1986), the solution to equation (20) can be stated

$$\{w(s)\} = [\Phi(s)]\{w_o\} + \{v(s)\}; \ (w)^T = (\tilde{u}_{s1}, \ \tilde{u}_{\theta 1}, \ \tilde{p}_1) \quad (22)$$

where $[\Phi]$ is the transition matrix, (w_o) is the vector of initial conditions, and (v) is the particular solution obtained for zero initial conditions. $[\Phi]$ is obtained by solving the homogeneous version of equation (20) three times for the initial conditions (1,0,0), (0,1,0), and (0,0,1). One of the three initial conditions of equation (22) is given; viz., $\tilde{u}_{\theta 1}(0) = 0$. Equation (21*b*) provides one relationship between the remaining unknown initial conditions $\tilde{p}_1(0)$ and $\tilde{u}_{s1}(0)$. The final relationship between these variables is obtained by evaluating equation (22) at $s = 1$ to obtain

$$\begin{aligned} \tilde{u}_{s1}(1) &= \Phi_{11}(1)\tilde{u}_{s1}(0) + \Phi_{13}(1)\tilde{p}_1(0) + v_1(1) \\ \tilde{p}_1(1) &= \Phi_{31}(1)\tilde{u}_{s1}(0) + \Phi_{33}(1)\tilde{p}_1(0) + v_3(1), \end{aligned} \quad (23)$$

and substituting into equation (21*c*). The resulting set of equations for the unknown initial conditions can be stated

$$\begin{bmatrix} (1+\xi) & 1 \\ \Phi_{31}(1) - C_{de}u_{s0}(1) & \Phi_{33}(1) - C_{de}u_{s0}(1) \end{bmatrix} \begin{Bmatrix} \tilde{u}_{s1}(0) \\ \tilde{p}_1(0) \end{Bmatrix} = \begin{Bmatrix} 0 \\ -v_3(1) + C_{de}u_{s0}(1)v_1(1) \end{Bmatrix} \quad (24)$$

For forced response, the right-hand side is nonzero, and the missing initial conditions are obtained by inverting the coefficient matrix.

The resonance peaks in Fig. 4 appear when f is near the imaginary part of the complex eigenvalue. To obtain the eigenvalue, the harmonic solution of equation (19) is replaced by the general solution format

$$\underline{u}_{s1} = \tilde{u}_{s1}e^{\alpha\tau}, \quad \underline{u}_{\theta 1} = \tilde{u}_{\theta 1}e^{\alpha\tau}, \quad \underline{p}_1 = \tilde{p}_1 e^{\alpha\tau}$$

where α is both a complex number and the desired eigenvalue. Substitution into equations (18) yields the following definition for the coefficient matrix of equation (20)

$$[A_r] = \begin{bmatrix} B & -j\dfrac{\omega T}{r} & 0 \\ A_{3\theta}/u_{s0} & (A_{2\theta} + j\Gamma T)/u_{s0} & -j\dfrac{b}{ru_{s0}}\left(\dfrac{L_s}{R_i}\right) \\ A_{3s} - u_{s0}B + j\Gamma T & A_{2s} + j\dfrac{\omega T}{r}u_{s0} & 0 \end{bmatrix} \quad (25)$$

where

$$B = \left(\frac{1}{r}\frac{dr}{ds} + \frac{1}{h_o}\frac{dh_o}{ds}\right), \quad \Gamma = \omega(\alpha - ju_{\theta 0}/r) \quad (26)$$

Now, the differential equations and their homogeneous solutions are a function of the desired eigenvalue α, and the eigenvalue is found when the determinant of the coefficient matrix of equation (24) is zero.

The following approach was used to solve for the complex eigenvalues:

(*a*) An initial value, α_0, is guessed based on the results of Fig. 4; viz., $\alpha_o = 0 + jf_o$ where f_o yields a peak on the $f_{\theta q}$ curve.

(*b*) The homogeneous version of equation (20) is solved to obtain $[\Phi]$, and the determinant

$$De = (1+\xi)[\Phi_{33}(1) - C_{de}u_{s0}(1)] - \Phi_{31}(1) + C_{de}u_{s0}(1) \quad (27)$$

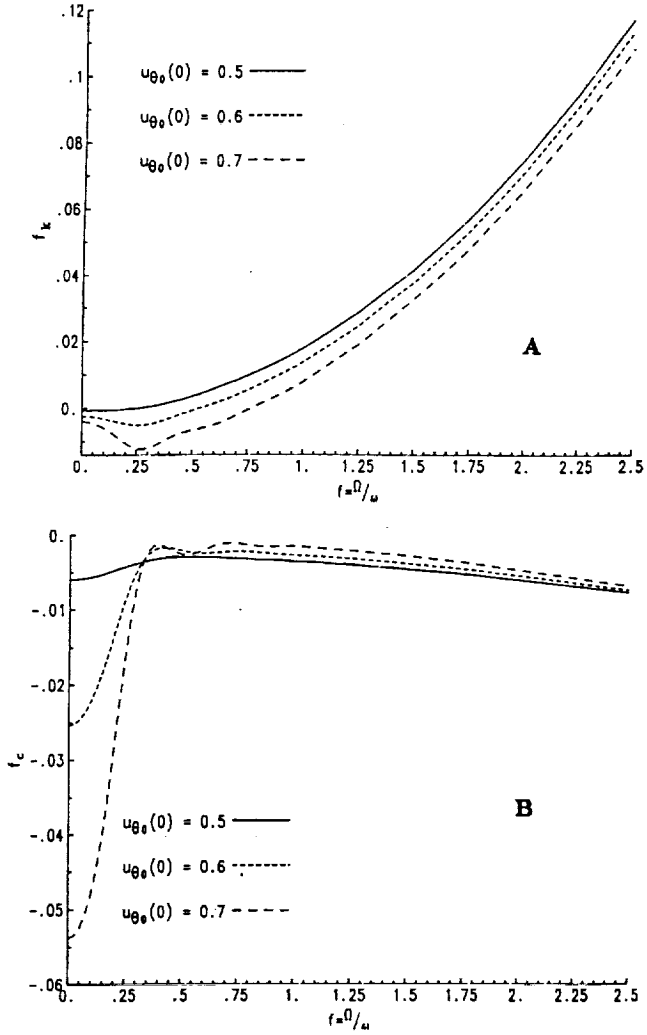

Fig. 5 Nondimensional axial force coefficients: (*a*) stiffness-force coefficient, (*b*) damping-force coefficient

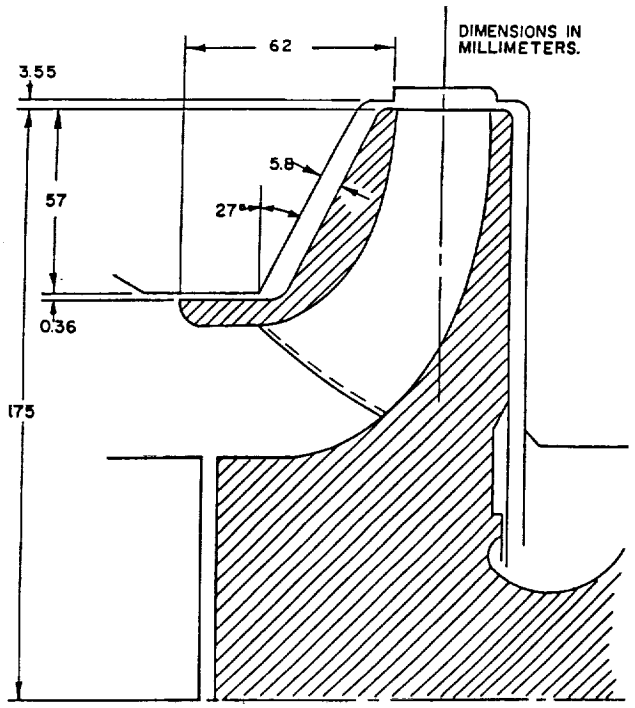

Fig. 6 Nominal configuration of the test impeller

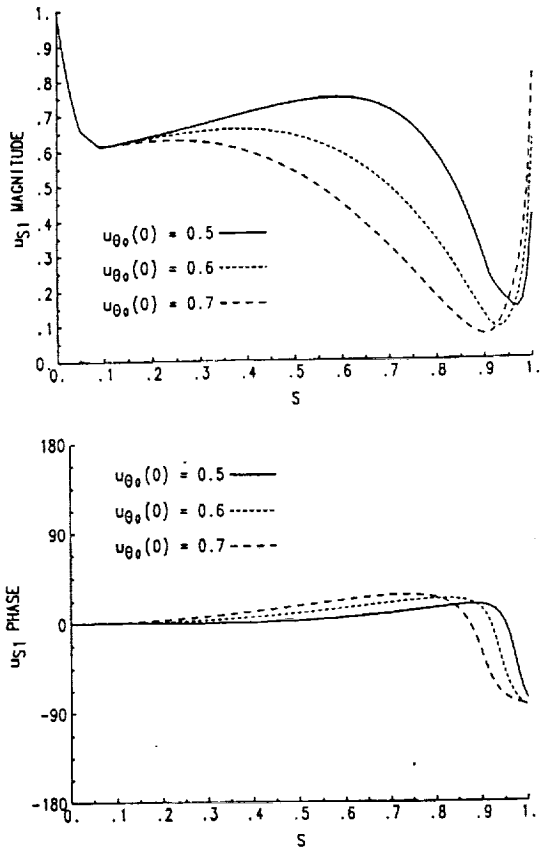

Fig. 7(a) $\bar{u}_{s1}(s)$ first-natural-frequency eigenvector corresponding to lateral excitation; $C_r = 0.36mm$

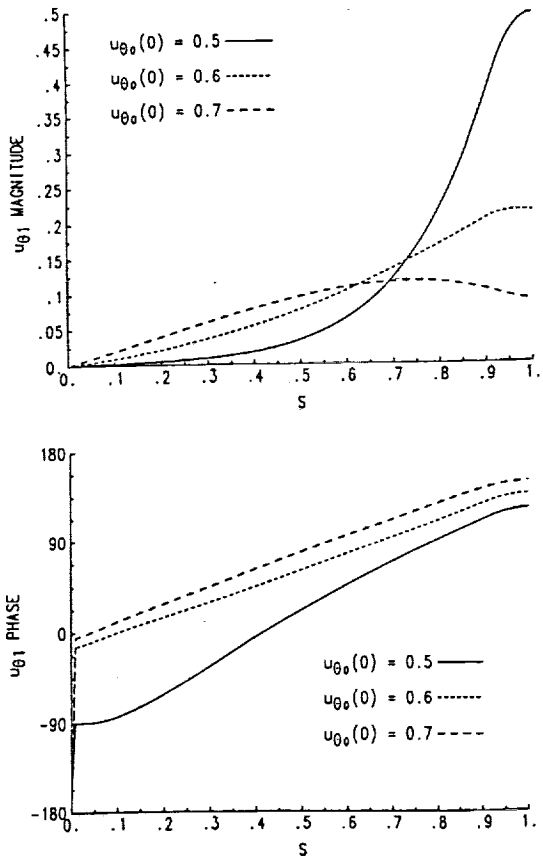

Fig. 7(b) $\bar{u}_{\theta 1}(s)$ first-natural-frequency eigenvector corresponding to lateral excitation; $C_r = 0.36mm$

is calculated at α_0 and $\alpha_1 = \alpha_0[1+\delta(1+j)]$ to obtain De_0 and De_1; δ is a small parameter.

(c) The secant rule is then used to calculate the next estimate α_2 and De_2 and subsequent α_i's and De_i's until convergence is achieved.

The eigenvalues are obtained by setting

$$\bar{u}_{s1}(0) = 1, \quad \bar{p}_1(0) = (1+\xi), \quad \bar{u}_{\theta 1}(0) = 0$$

and evaluating equation (22)

$$\{w(s)\} = [\Phi(s,\alpha)]\{w(0)\}$$

over $s \epsilon [0,1]$.

Eigen Solutions Corresponding to Axial Excitation

For axial excitation, the perturbed clearance function $h_1(\tau)$ is defined from equations (4) and (8) to be

$$\epsilon h_1 = \frac{\Delta(\tau)}{C_i}\left(\frac{R}{L_s}\right)\frac{dr}{ds}$$

This excitation is not a function of θ, and neither are the associated forced-response solutions. Figure 5 illustrates real and imaginary reaction-force coefficients resulting from axial impeller excitation (Childs 1990). Note that "resonance" phenomena are also present in these results.

To obtain eigenvalues and eigenvectors, the following corresponding assumed solution is substituted into equation (14)

$$u_{s1} = \bar{u}_{s1}e^{\alpha\tau}, \quad u_{\theta 1} = \bar{u}_{\theta 1}e^{\alpha\tau}, \quad p_1 = \bar{p}_1 e^{\alpha\tau},$$

and the θ derivatives are dropped to obtain the homogeneous equations

$$\frac{d}{ds}\begin{Bmatrix}\bar{u}_{s1}\\ \bar{u}_{\theta 1}\\ \bar{p}_1\end{Bmatrix} + [A_z]\begin{Bmatrix}\bar{u}_{s1}\\ \bar{u}_{\theta 1}\\ \bar{p}_1\end{Bmatrix} = 0$$

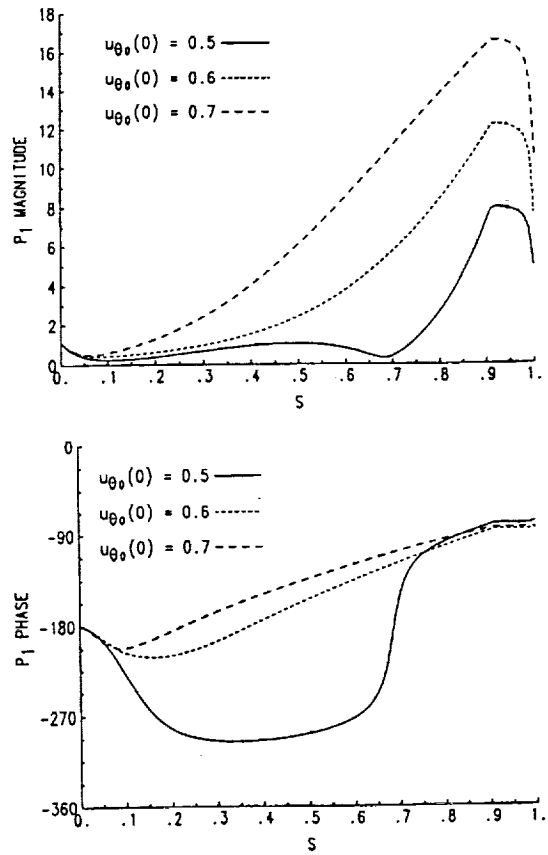

Fig. 7(c) $\bar{p}_1(s)$ first-natural-frequency eigenvector corresponding to lateral excitation; $C_r = 0.36mm$

Table 1 Zeroth-order-solution results; $C_l = 3.5mm$, $C_r = 0.36mm$

$u_{\theta o}(0)$	0.5	0.6	0.7
C_{da}	1.655	1.690	1.731
$\dot{m}$ (kg/sec)	4.784	4.391	3.973

Table 2 Lowest-natural-frequency eigenvalues corresponding to lateral excitation

$u_{\theta 0}(0)$	$C_r(mm)$	σ	ω_d	ζ	ω_n
0.5	.36	−.621	.196	.953	.651
0.6	.36	−.288	.300	.693	.416
0.7	.36	−.174	.349	.446	.391
0.5	.72	−.670	.175	.936	.716
0.6	.72	−.315	.291	.734	.429
.07	.72	−.188	.345	.480	.392

Table 3 Second-natural-frequency eigenvalues corresponding to lateral excitation; $C_r = 0.36mm$

$u_{\theta 0}(0)$	σ	ω_d	ζ	ω_n
0.5	−.787	1.2	.549	1.43
0.6	−.344	1.21	.273	1.26
0.7	−.214	1.23	.172	1.25

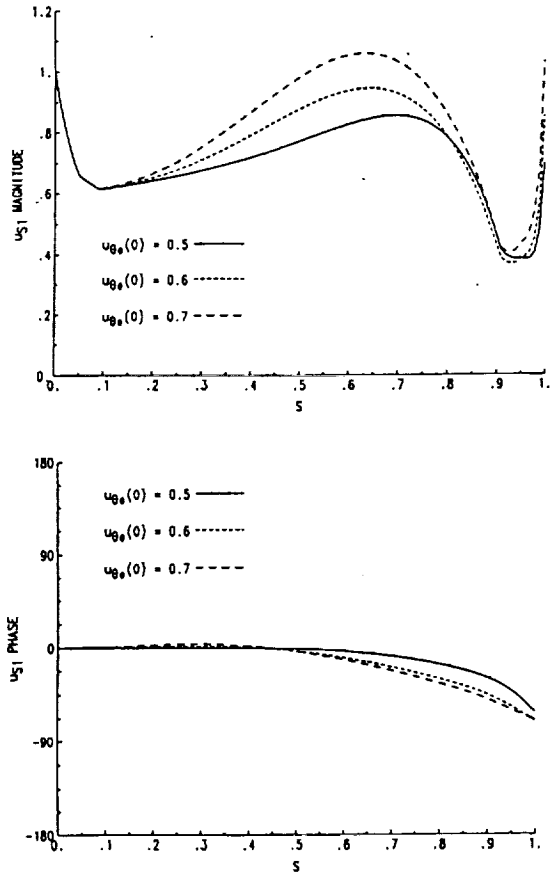

Fig. 8(a) $\tilde{u}_{s1}(s)$ second-natural-frequency eigenvector corresponding to lateral excitation; $C_r = 0.36mm$

where

$$[A_z] = \begin{bmatrix} B & 0 & 0 \\ A_{3\theta}/u_{s0} & (A_{2\theta} + \alpha\omega T)/u_{s0} & 0 \\ A_{3s} - u_{s0}B + \alpha\omega T & A_{2s} & 0 \end{bmatrix} \quad (28)$$

Equation (21) continues to define the boundary conditions,

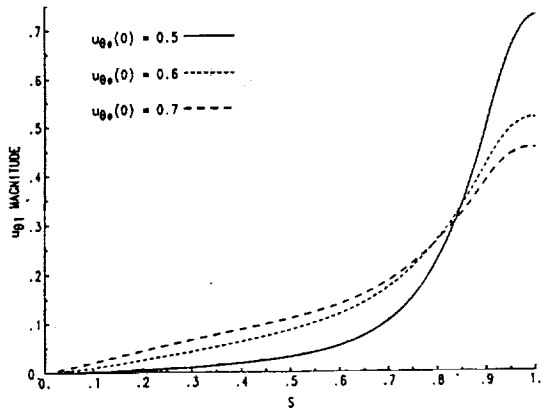

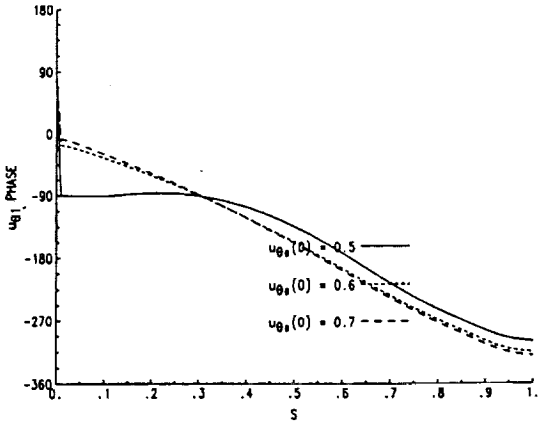

Fig. 8(b) $\tilde{u}_{\theta 1}(s)$ second-natural-frequency eigenvector corresponding to lateral excitation; $C_r = 0.36mm$

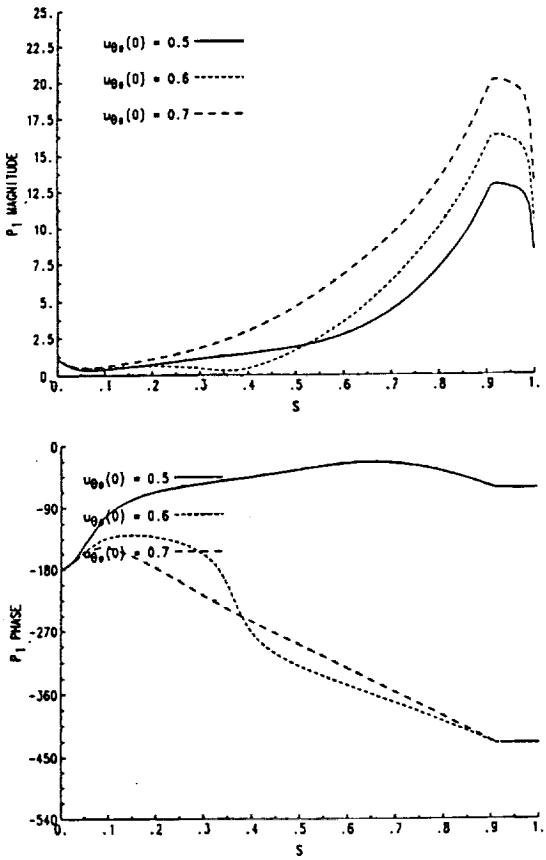

Fig. 8(c) $\tilde{p}_1(s)$ second-natural-frequency eigenvector corresponding to lateral excitation; $C_r = 0.36mm$

Table 4 First-natural-frequency eigenvalues corresponding to axial excitation

$u_{\theta 0}(0)$	$C_r(mm)$	σ	ω_d	ζ	ω_n
0.5	.36	−1.06	.478	.911	1.16
0.6	.36	−.584	.396	.878	.706
0.7	.36	−.400	.364	.740	.541
0.5	.72	−1.12	.505	.912	1.23
0.6	.72	−.619	.418	.829	.746
.07	.72	−.680	.382	.740	.568

and an eigenvalue is obtained when the determinant of equation (27) is zero.

Numerical Results

Introduction. Figure 6 illustrates the pump-impeller and shroud geometry used by Bolleter et al. (1987) in their test program for radial force coefficients. Their tests were at best efficiency point (BEP) with the pump running at 2000rpm, while developing 68m of head and 130l/sec of flow rate. The impeller has seven blades and an impeller exit angle of 22.5 deg. The test fluid is water at 80°F. For the present study, ΔP across the impeller is assumed to be 70 percent of the total head rise of the stage. Based on pitot-tube measurements, impeller exit tangential velocity is about 50 percent of the impeller discharge surface velocity; hence, $u_{\theta 0} = 0.5$.

Both walls of the annulus are assumed to be smooth and represented by Yamada's (1962) turbulence-coefficient test data: $mr = ms = -0.25$, $nr = ns = 0.079$. The inlet loss for the annulus, ξ, is assumed to be 0.1. The discharge coefficient for the seal is calculated iteratively as follows. With an assumed C_{de}, equations (10) through (13) are used to calculate the leakage through the impeller annulus and the pressure and tangential-velocity upstream of the seal. The seal is then analyzed (with the same equations) using the calculated seal inlet pressure and tangential velocity to determine leakage and C_{de}. The iteration continues until the leakage predictions for the exit seal and the impeller annulus agree. Table 1 below provides zeroth-order solutions.

Eigen Solution Results Corresponding to Lateral Excitation. Table 2 contains the complex eigenvalues $\alpha = \sigma + j\omega_d = -\zeta\omega_n + j\omega_n\sqrt{1-\zeta^2}$ for the lowest-frequency eigenvalue. Results are provided for both nominal ($C_r = 0.36$mm) and double radial seal clearances. Observe that the damped natural frequency ω_d ranges from about 20 percent to 30 percent of running speed. Starting guesses for the eigenvalues were $\alpha_o = 0 + 0.4j$, because the lowest-frequency peaks in Fig. 4(*a*) are around $f = 0.4$. Observe that the calculated eigenvalues are entirely consistent with the results of Fig. 4(*a*); specifically, the solutions are stable and highly damped, the damping factor ζ decreases as $u_{\theta 0}(0)$ increases, and both ω_n and the f value corresponding to peaks in the $f_{\theta q}$ curves decrease as $u_{\theta 0}(0)$ increases. The results are observed to be relatively insensitive to changes in the exit-seal clearance.

Figure 7 contains the complex eigenvectors for the $C_r = 0.36$mm. The $\bar{u}_{s1}(s)$ vector has a peak amplitude at the inlet and exit with a small phase shift at the inlet. The $\bar{u}_{\theta 1}(s)$ magnitude and phase tend to increase steadily with increasing s. The $\bar{p}_1(s)$ magnitude increases steadily with increasing s until about $s = 0.9$ and then drops abruptly as it approaches the exit seal. The sharp change in $\bar{u}_{s1}$ and $\bar{p}_1$ between $s = 0.9$ and $s = 1.0$ is caused by the sharply convergent flow path, illustrated in Fig. 5, as the flow approaches the exit seal. Note that the phase of $\bar{u}_{s1}$ is near zero until it approaches the exit and then drops rapidly. The rapid phase shift at the exit is indicative of the large energy dissipation associated with the exit discharge seal.

Table 3 contains eigenvalues for the second-natural-frequency eigenvector. Again, the damping factor and undamped natural frequency drop as $u_{\theta 0}(0)$ increases. Figure 8 illustrates the complex eigenvectors for these eigenvalues. Comparing $\bar{u}_{s1}(s)$ in Figs. 7(*a*) and 8(*a*) shows similar mode shapes; however, the peak amplitudes increase with increasing $u_{\theta 0}(0)$ for the first eigenvector but decrease with increasing $u_{\theta 0}(0)$ for the second eigenvector. The phase of $\bar{u}_{\theta 1}(s)$ increases for the first eigenvector with increasing s but decreases for the second eigenvector. The $\bar{p}_1(s)$ amplitudes are similar for both the first and second eigenvectors; however, their phase behavior is quite different.

Diligent searches revealed no eigenvalues with natural frequencies below the first eigenvalue or between the first and second eigenvalues.

Eigen Solution Results Corresponding to Axial Excitation. Table 4 contains the first-natural-frequency eigenvector corresponding to axial excitation for $C_r = 0.36$, 0.72mm. As with the earlier results of Table 2, the damping factor and undamped natural frequency both drop as $u_{\theta 0}(0)$ increases. Also, the results are relatively insensitive to changes in seal clearance. The undamped natural frequencies are higher for this type of mode shape than for the corresponding lateral-excitation mode shapes.

Figure 9 illustrates the mode shapes corresponding to axial-excitation. Comparing Figs. 7 and 9 shows a pronounced difference for the $\bar{u}_{s1}(s)$ eigenvectors. For the axial case, $\bar{u}_{s1}(s)$ is real and, in fact, coincides with the $u_{s0}(s)$ solution. This result is predicted by equation (28) since $\bar{u}_{s1}$ is uncoupled from $\bar{u}_{\theta 1}$ and $\bar{p}_1$ and satisfies the zeroth-order continuity equation. The $\bar{u}_{\theta 1}(s)$ eigenvector magnitudes of Figs. 7(*b*) and 9(*b*) are similar; however, the magnitudes are much larger for the axial-excitation modes. The amplitude curves for $\bar{p}_1(s)$ are similar in Figs. 7(*c*) and 9(*c*); however, the axial excitation cases are much larger and are relatively insensitive to changes in $u_{\theta 0}(0)$.

Discussion of Approach and Results

The eigenvalues presented in Tables 2 through 4 seem to be entirely consistent with the forced-response curves of Figs. 4 and 5; specifically, the natural frequencies generally lie where they are expected, and they and their damping factors vary with $u_{\theta 0}(0)$ as expected. The eigenvectors of Figs. 7, 8, and 9 are difficult to comment on, given that (to the writer's knowledge) no one has tried to either calculate or measure this type of eigenvector in the past. The mode shapes clearly satisfy the boundary conditions and are consistent with the damped eigenvalues to which they correspond.

The homogeneous versions of equations (14) do not (to the writer) represent an obvious eigenvalue problem, and attempts to formulate a recognizable eigenvalue problem by conventional means were not successful. Specifically, because the governing equations (20) are linear, one can differentiate and substitute to obtain a single third-order equation in one of the variables. Unfortunately, this approach makes the boundary-condition implementation very difficult. Moreover, the final governing equation is itself not amenable to classical eigen-approaches such as central-difference finite differences; such approaches have proven to be notably unsuccessful for fluid mechanics problems.

The approach used here to obtain eigenvalues converged rapidly, but the convergence characteristics suggest that the convergence space is not convex. Specifically, full correction steps predicted by the secant algorithm could not be taken. Generally speaking, correction steps would be reduced by a factor of ten at the outset. The residual error in $|De|$, the magnitude of D_e, would then be rapidly reduced until an overshoot was observed. The problem would then be restarted at the α_i corresponding to $|De|$ *min*, the secant correction factor reduced by an additional factor of ten, and a further rapid incremental reduction in $|De|$ would again be realized

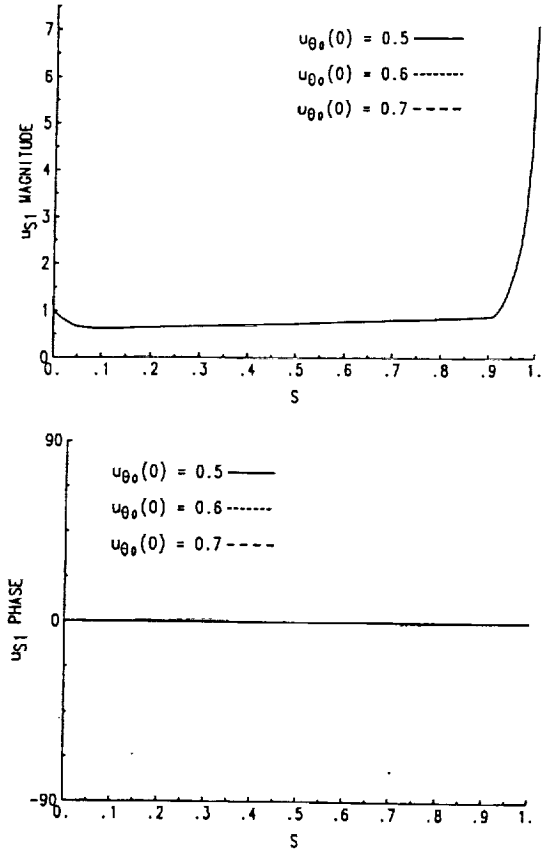

Fig. 9(a) $\bar{u}_{s1}(s)$ first-natural-frequency eigenvector corresponding to axial excitation; $C_r = 0.36mm$

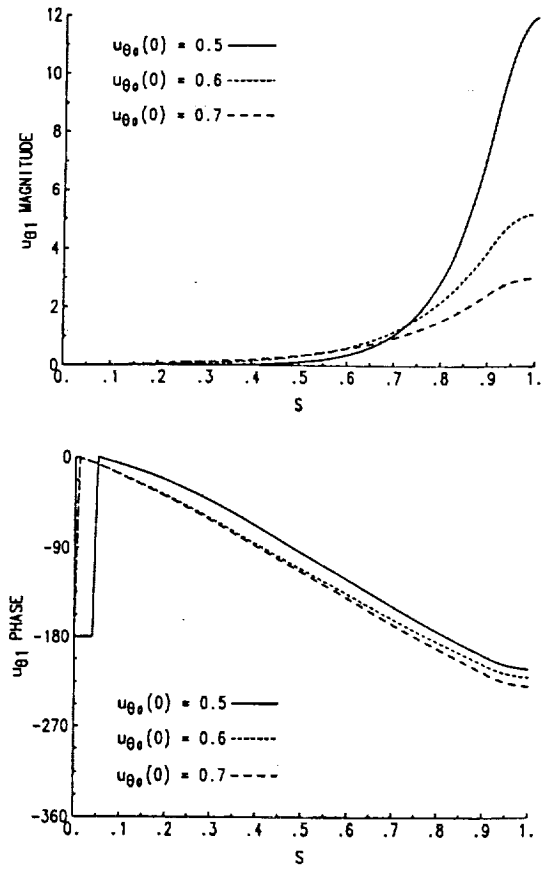

Fig. 9(b) $\bar{u}_{\theta 1}(s)$ first-natural-frequency eigenvector corresponding to axial excitation; $C_r = 0.36mm$

until an overshoot was again experienced. By following this "restart" approach, the eigenvalues could be calculated to any accuracy desired.

The developed algorithm would appear to be applicable to a range of fluid perturbation problems where the fluid mechanics might have an appreciable influence on "acoustics"; specifically, in circumferences where convective acceleration, Coriolis acceleration, and/or centrifugal acceleration terms are not negligible. It would be adaptable to more strictly numerical CFD approaches such as the control-volume-based methods of Patankar (1980).

The eigensolutions which were calculated in this work were, as specified, stimulated by forced frequency-response solutions. Obviously, more general solutions could be calculated; e.g., solutions of the form

$$u_{s1} = u_{s1_c}\cos n\theta + u_{s1_s}\sin n\theta$$
$$u_{\theta 1} = u_{\theta 1_c}\cos n\theta + u_{\theta 1_s}\sin n\theta$$
$$p_1 = p_{1_c}\cos n\theta + p_{1_s}\sin n\theta$$

with n an arbitrary integer, could be assumed for eigenvalue solutions. The solutions developed and presented here only correspond to $n = 0,1$. Also, while the presented solutions correspond to clearance-change excitation due to impeller motion, these modes could be excited by strictly fluid oscillation.

For axial excitation, Childs' (1990) work indicates that the impeller-shroud forces have a negligible influence on pump vibrations. However, Williams and Childs (1989) demonstrate that "fluid resonance" phenomena can have an appreciable influence on lateral rotordynamics of pumps.

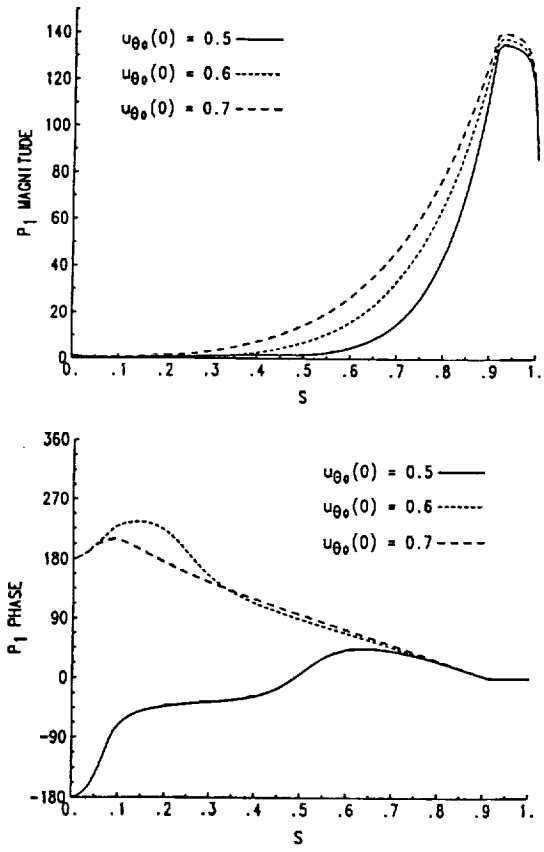

Fig. 9(c) $\bar{p}_1(s)$ first-natural-frequency eigenvector corresponding to axial excitation; $C_r = 0.36mm$

Acknowledgment

The results reported herein were funded in part by NASA Marshall Space Flight Center, NASA Contract NAS 8-37821; Contract Monitor: James Cannon.

References

Bolleter, U., Wyss, A., Welte, I., and Sturchler, R., 1987, "Measurement of Hydrodynamic Matrices of Boiler Feed Pump Impellers," ASME JOURNAL OF VIBRATIONS, STRESS, AND RELIABILITY IN DESIGN, Vol. 109, pp. 144–151.

Childs, D. W., and Kim, C-H, 1985, "Analysis and Testing for Rotordynamic Coefficients of Turbulent Annular Seals with Different Directionally Homogeneous Surface Roughness Treatment for Rotor and Stator Elements," ASME *Journal of Tribology*, Vol. 107, July 1985, pp. 296–306.

Childs, D. W., 1987, "Fluid Structure Interaction Forces at Pump-Impeller-Shroud Surfaces for Rotordynamic Calculations," *Rotating Machinery Dynamics*, Vol. 2, ASME, pp. 581–593.

Childs, D. W., 1989, "Fluid Structure Interaction Forces at Pump-Impeller-Shroud Surfaces for Rotordynamic Calculations," ASME JOURNAL OF VIBRATION, ACOUSTICS, STRESS, AND RELIABILITY IN DESIGN, Vol. 111, pp. 216–225.

Childs, D. W., 1990, "Fluid-Structure Interaction Forces at Pump-Impeller-Shroud Surfaces for Axial Vibration Analysis," ASME JOURNAL OF VIBRATION AND ACOUSTICS, *in press*.

Hirs, G. G., 1973, "A Bulk-Flow Theory for Turbulence in Lubricant Films," ASME *Journal of Lubrication Technology*, April 1973, pp. 137–146.

Meirovitch, L., 1985, *Introduction to Dynamics and Control*, J. Wiley.

Patankar, S. V., 1980, *Numerical Heat Transfer and Fluid Flow*, McGraw-Hill Co., N.Y.

Williams, J., and Childs, D., "Influence of Impeller Shroud Forces on Pump Rotordynamics," presented at the 12th Biennial ASME Vibration Conference, 17–20 September 1989, under review for ASME JOURNAL OF VIBRATION AND ACOUSTICS.

Yamada, Y., 1962, "Resistance of Flow Through an Annulus with an Inner Rotating Cylinder," Bull. JSME, Vol. 5, No. 18, pp. 302–310.

APPENDIX A

Perturbation Coefficients

$$A_{1s} = [\sigma_s(1 - ms) + \sigma_r(1 - mr)]u_{so}^2/2h_o$$

$$A_{2s} = -\frac{2u_{\theta o}}{r}\frac{dr}{ds}/b^2 + [\sigma_r(mr + 1)\beta_o + \sigma_s(ms + 1)\beta_1]u_{so}/2$$

$$A_{3s} = \frac{du_{so}}{ds} + [(2 + mr)\sigma_r + (2 + ms)\sigma_s]u_{so}/2 - [(1 + mr)\sigma_r\beta_o(u_{\theta o} - r) + (1 + ms)\sigma_s\beta_1 u_{\theta o}]/2$$

$$2A_{1\theta} = u_{so}[(1 - mr)(u_{\theta o} - r)\sigma_r + (1 - ms)u_{\theta o}\sigma_s]/h_o$$

$$2A_{2\theta} = u_{so}(\sigma_r + \sigma_s) + \sigma_r(mr + 1)(u_{\theta o} - r)\beta_o + \sigma_s(ms + 1)u_{\theta o}\beta_1 + 2\frac{u_{so}}{r}\frac{dr}{ds}$$

$$2A_{3\theta} = \sigma_r(u_{\theta o} - r)[mr - (1 + mr)\beta_o(u_{\theta o} - r)/u_{so}] + \sigma_s u_{\theta o}[ms - (1 + ms)\beta_1 u_{\theta o}/u_{so}]$$

$$\beta_o = (u_{\theta o} - r)/b^2 u_{so}\{1 + [(u_{\theta o} - r)/bu_{so}]^2\}$$

$$\beta_1 = u_{\theta o}/b^2 u_{so}[1 + (u_{\theta o}/bu_{so})^2]$$

Williams, J. and
Childs, D. (1992a)

Influence of Impeller Shroud Forces on Turbopump Rotor Dynamics

J. P. Williams
Rockwell Space Operations Company,
600 Gemini, R20-B,
Houston, TX 77058

D. W. Childs
Department of Mechanical Engineering,
Texas A&M University,
College Station, TX 77843

The shrouded-impeller leakage path forces calculated by Childs (1987) have been analyzed to answer two questions. First, because of certain characteristics of the results of Childs, the forces could not be modeled with traditional approaches. Therefore, an approach has been devised to include the forces in conventional rotordynamic analyses. The forces were approximated by traditional stiffness, damping and inertia coefficients with the addition of whirl-frequency-dependent direct and cross-coupled stiffness terms. The forces were found to be well-modeled with this approach. Finally, the effect these forces had on a simple rotor-bearing system was analyzed, and, therefore, they, in addition to seal forces, were applied to a Jeffcott rotor. The traditional methods of dynamic system analysis were modified to incorporate the impeller forces and yielded results for the eigenproblem, frequency response, critical speed, transient response, and an iterative technique for finding the frequency of free vibration as well as system stability. All results lead to the conclusion that the forces have little influence on natural frequency but can have appreciable effects on system stability. Specifically, at higher values of fluid swirl at the leakage path entrance, relative stability is reduced. The only unexpected response characteristics that occurred are attributed to the nonlinearity of the model.

Introduction

The vibration of centrifugal pumps has received increasing attention recently because of the inability of current analysis techniques to adequately predict the dynamic characteristics of pump designs. Failure to accurately predict vibrations has resulted in the loss of considerable amounts of money in down time from severe vibration problems. Massey (1985), for example, described an eleven-stage pump that became unstable when its running speed exceeded its critical speed by 25 percent. In other words, it whirled at 80 percent of running speed. Another example occurred in the High Pressure Oxygen Turbopump (HPOTP) of the Space Shuttle Main Engine (SSME) which also whirled at 80 percent of running speed (Childs and Moyer, 1985).

The hydrodynamic forces generated in many of the fluid-filled gaps within the pump are well-established contributors to the problems cited above. This article is concerned specifically with the forces developed along the leakage path between the impeller and the shroud, as shown in Fig. 1. As the fluid is discharged from the impeller, some will return to the lower-pressure, suction side by way of this leakage path. Leakage is minimized typically with wear ring seals, as shown. Hydrodynamic forces are developed along the entire leakage path, i.e., the shroud section as well as the seal. Note that these are only parts of the total force on the impeller and that the impeller/volute region, balance drums, inducers, shaft, etc. also contribute to the dynamics of pumps, although they are not considered here.

Unfortunately, measurements of the total force on actual impellers have typically been obtained using pumps that have been modified to minimize leakage path forces. However, some results have been reported that are of importance here. For example, research at Cal Tech (Adkins, 1976) led to the conclusion that the pressures in the shroud annulus contributed from about 50 percent to 75 percent of the total stiffness acting on the impeller. The pump used included separation rings and an enlarged shroud clearance space to minimize leakage flow forces.

Bolleter et al. (1985) used a rocking-arm mechanism to vertically translate the spinning impeller. Their pump had normal clearances in the leakage path; and, therefore, the forces meas-

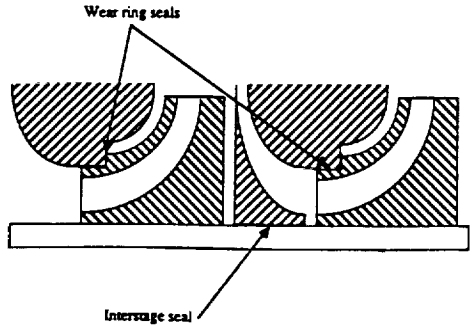

Fig. 1 Typical seal configurations for a multistage pump

Contributed by the Technical Committee on Vibration and Sound for publication in the JOURNAL OF VIBRATION AND ACOUSTICS. Manuscript received February 1990.

ured were more realistic. The results demonstrated that the nondimensionalized cross-coupled stiffness value was about twice that measured on the pump at Cal Tech (Jery et al., 1984). This suggests that the leakage path region in pumps can also reduce the stability of impeller motion. Bolleter et al. (1989) have recently presented extensive force-coefficient results at off-design conditions.

Almost all of the analytical attempts at predicting leakage path forces have been concerned with seals. However, Childs has extended his previous techniques in seal analysis (1980, 81, 82a, 82b, 82c) to apply them to the flow within the clearance space surrounding the shroud (1987). His work will be used to model the seal and shroud forces in this article and will now be summarized.

Childs used a bulk-flow approach to obtain the governing equations of the flow of a differential element of fluid. In the seal problem, three equations were required: axial- and circumferential-momentum equations as well as the continuity equation. In the shroud problem, the axial-momentum equation was replaced by a path-momentum equation, introducing additional terms which described the centrifugal and Coriolis accelerations of the fluid element. After a perturbation expansion of the equations in the eccentricity ratio, the resulting relationships were solved at various values of the whirl frequency, Ω. Integration of the resulting pressure distribution acting on the shaft or shroud yielded the radial and tangential force as functions of whirl frequency. In addition, solution was carried out at various fluid circumferential velocities at the shroud entrance. This variable is of primary importance in system stability (cross-coupled stiffness). Figure 2 shows the results of the shroud problem for three different values of the inlet swirl velocity. The leakage path analyzed corresponded to that used by Bolleter et al. (1985) which ran at 2000 rpm. Figure 3 provides the dimensions of the pump and other data of importance. The curves in Fig. 2 define force coefficients corresponding to a circular orbit of amplitude and whirl frequency ratio f. The impeller force components are linearly proportional to the orbit amplitude A. The sharp deviations

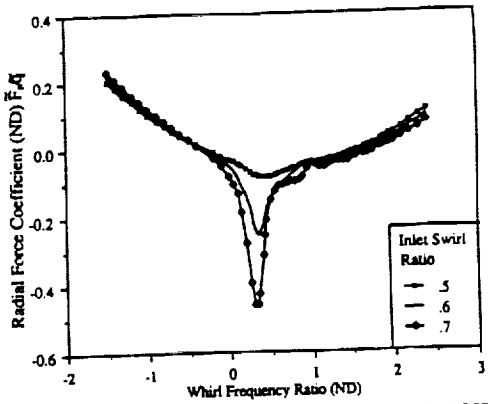

Fig. 2(a) Radial force coefficient curves (Childs, 1987)

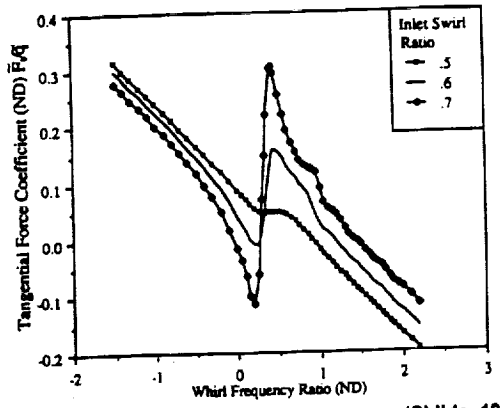

Fig. 2(b) Tangential force coefficient curves (Childs, 1987)

in the radial and tangential force coefficients of Fig. 2 are caused by excitation of a "centrifugal-acceleration mode" natural frequency. Childs (1990) has presented results for damped natural frequencies and eigenvalues for these modes.

Nomenclature

$\bar{C}=\frac{CQ_0\omega_s}{F_0}$ = nondimensional direct damping coefficient

$\bar{c}=\frac{cQ_0\omega_s}{F_0}$ = nondimensionalized cross-coupled damping coefficient

$\bar{F}_{r/t}=\frac{F_{r/t}}{F_0}$ = nondimensionalized radial and tangential forces on the rotor

$F_0=2R_LL\Delta P$ = (Childs, 1987)(F)

$f=\frac{\Omega}{\omega_s}$ = whirl frequency ratio

$\bar{K}=\frac{KQ_0}{F_0}$ = nondimensionalized direct stiffness coefficient

K^* = direct stiffness coefficient which is a function of the whirl frequency ratio (F/L)

$\bar{k}=\frac{kQ_0}{F_0}$ = nondimensionalized cross-coupled stiffness coefficient (Childs, 1987)

k^* = cross-coupled stiffness coefficient which is a function of the whirl frequency ratio (F/L)

L = length of seal or impeller-shroud path (L)

$\bar{M}=\frac{MQ_0\omega_s^2}{F_0}$ = nondimensionalized direct mass coefficient (Childs, 1987)

Q = rotor whirl radius (L)

Q_0 = clearance at leakage path entrance (L)

$\bar{q}=\frac{Q}{Q_0}$ = clearance ratio

R = rotor whirl amplitude (L)

$R_{L,s}$ = inlet radius of shroud leakage path or seal (L)

$\bar{u}_{tL/s}=\frac{u_{tL/s}}{R_L\omega_s}$ = nondimensionalized tangential fluid velocity at leakage path or seal entrance (inlet swirl ratio) (Childs, 1987)

x, y = rectangular coordinates of rotor center (L)

Z = complex rotor whirl amplitude (L)

$z=x+jy$ = complex rotor coordinate (L)

ϕ = phase angle of whirl from harmonic excitation

Ω = rotor whirl frequency ($1/T$)

ω_n = natural frequency of free vibration ($1/T$)

ω_s = shaft speed ($1/T$)

L = shroud leakage path coefficient subscript

r = rotor coefficient subscript

s = seal coefficient subscript

sh = shaft coefficient subscript

$none$ = overall coefficient subscript

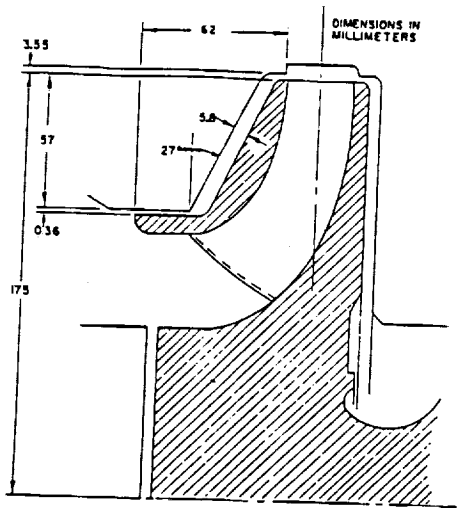

Pump data

shaft speed = ω_s = 2000 rpm

inlet clearance = Q_o = 3.55 mm

impeller exit angle = 22.5 °

flowrate = 130 l/sec

head developed = 68 m

seven-bladed impeller

working fluid is water at 80 °F

Fig. 3 Dimensions and data for the pump tested by Bolleter et al (Bolleter et al, 1985)

In the articles cited above, Childs initially suggested the following conventional, linear relationship to model the forces. It applies for small motion of the rotor about the centered position.

$$-\begin{Bmatrix} F_x \\ F_y \end{Bmatrix} = \begin{bmatrix} M & 0 \\ 0 & M \end{bmatrix} \begin{Bmatrix} \ddot{x} \\ \ddot{y} \end{Bmatrix} + \begin{bmatrix} C & c \\ -c & C \end{bmatrix} \begin{Bmatrix} \dot{x} \\ \dot{y} \end{Bmatrix} + \begin{bmatrix} K & k \\ -k & K \end{bmatrix} \begin{Bmatrix} x \\ y \end{Bmatrix}. \tag{1}$$

If circular whirl at frequency, Ω, and radius, Q, is assumed such that

$$\begin{aligned} x &= Q \cos \Omega t, \\ y &= Q \sin \Omega t, \end{aligned} \tag{2}$$

the radial and tangential force components can be stated

$$-\begin{Bmatrix} F_r \\ F_t \end{Bmatrix} = Q \begin{Bmatrix} -M\Omega^2 + c\Omega + K \\ C\Omega - k \end{Bmatrix} \tag{3}$$

After nondimensionalizing the terms as defined in Childs (1987), Eqs. (3) become

$$\begin{aligned} \frac{\bar{F}_r}{\bar{q}} &= \bar{M}f^2 - \bar{c}f - \bar{K} \\ \frac{\bar{F}_t}{\bar{q}} &= -\bar{C}f + \bar{k}, \end{aligned} \tag{4}$$

where the definitions of the coefficients are included in the Nomenclature and the other variables are defined as follows.

$\bar{F} = \dfrac{F}{2R_L L \Delta P}$, nondimensionalized force

$\bar{q} = \dfrac{Q}{Q_0}$, nondimensionalized clearance

$f = \dfrac{\Omega}{\omega}$, whirl frequency ratio

$\dfrac{\bar{F}}{\bar{q}}$, force coefficient.

The quadratic relationships of equations (4) are to be used to obtain the dynamic coefficients of equations (1). Specifically, a least-squares curve fit of the force curves will yield the coefficients. This is an adequate approach for seal forces because they, in general, do follow a quadratic trend. However, the curves of Fig. 2 illustrate that shroud forces cannot be approximated by equations (4); and, therefore, a traditional linear model as expressed in equations (1) will not adequately represent the forces. Although these results are unexpected, experimental measurements made by Franz and Arndt (1986) of impellers with inducers yielded very similar results.

Problem Definition

At this point, it is not known, assuming the force curves of Fig. 2 are valid, how they can best be included in traditional rotordynamic calculations of stability, response, critical speeds, etc. To solve this problem, the present research has been conducted to answer the following questions.

(*1*) How can the force curves found by Childs (1987) be incorporated in the traditional rotordynamic analyses of system response, stability, critical speeds, etc.?

(*2*) What effects do the forces have on a rotor-bearing system with respect to stability, natural frequencies, imbalance response, etc.?

Before answering these questions, observe that the forces present no new problems in a transient analysis because they could be applied as whirl-frequency-dependent forcing functions to a simple rotor model such as that developed by Jeffcott (1919). Although the force components are linearly proportional to the orbit amplitude, the equations of motion would be nonlinear because the forces depend on the whirl frequency, defined kinematically as

$$f = \frac{\Omega}{w_s} = \frac{x\dot{y} - y\dot{x}}{w_s(x^2 + y^2)}, \tag{5}$$

but this could be handled by integrating the equations of motion numerically with traditional methods. However, a transient analysis alone is not sufficient to obtain an understanding of the forces, and this is why answers to the questions posed above are necessary. The following section describes the model used to analyze the shroud forces, and results are then given for the eigenvalue problem and frequency response, respectively.

Rotordynamic Model

As shown in Fig. 4, the model is a Jeffcott rotor (Jeffcott, 1919) under the application of seal and shroud forces. The rotor itself represents a double-suction impeller, yielding two symmetrical leakage paths. In summary, the forces on the rotor are the shaft stiffness, two identical seal forces, and two identical shroud forces. The mathematical representation of each force will now be discussed.

A 90.7 kg (200lb) rotor is assumed. In addition, the shaft stiffness used (K_{sh} = .2987 MN/m) makes the natural frequency of forward whirl (to be defined later) equal to 80 percent of shaft speed. This choice is not completely arbitrary since this frequency corresponds to that observed in the examples cited in the Introduction (Massey, 1985; Childs and Moyer, 1985).

The seals modeled are smooth, wear ring seals with a clearance and diameter of .36 mm and 236 mm, respectively. The least-squares approach of Childs described earlier has been carried out, and the resulting dynamic coefficients are given

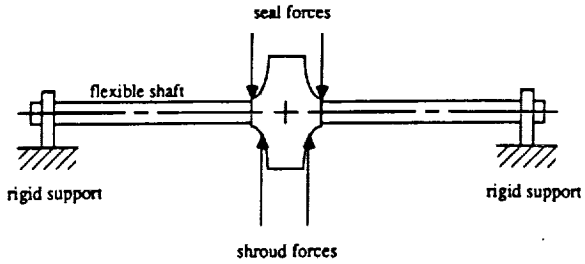

Fig. 4 Jeffcott-based, double-suction impeller leakage path model

Table 1 Coefficients for one wear ring seal

$\bar{u}_{tL}$	M_s kg	C_s Ns/m	c_s Ns/m	K_s MN/m	k_s MN/m
.5	.3111	3356.0	78.6	.6121	.4628
.6	.3398	2167.0	89.6	.5443	.4611
.7	.3714	970.9	101.3	.4755	.4455

in Table 1. The analysis used has at times under-predicted the true value of the direct stiffness. Therefore, K_s is doubled when the coefficients of the entire model are assembled. This modification of K_s has no influence on the results, since the shaft stiffness is selected to yield a desired system natural frequency.

As described in the introduction, conventional stiffness, damping and mass coefficients cannot completely describe the impeller-shroud forces calculated by Childs and shown in Fig. 2. Therefore, the following method has been devised. First, a curve fit of the force curves is carried out, yielding dynamic coefficients which describe the quadratic variation of the forces with respect to the whirl frequency ratio as described above. The difference between these curve fits and the actual force curves is modeled by direct and cross-coupled stiffness coefficients which are functions of whirl frequency ratio. The mathematical equivalent of this approach will now be discussed.

The following modified forms of equations (4) express the method with which the impeller-shroud forces are modeled.

$$\frac{\bar{F}_r}{\bar{q}} = \bar{M}_L f^2 - \bar{c}_L f - [\bar{K}_L + \bar{K}^*(f)]$$

$$\frac{\bar{F}_t}{\bar{q}} = -\bar{C}_L f + [\bar{k}_L + \bar{k}^*(f)], \tag{6}$$

where $\bar{K}^*$ and $\bar{k}^*$ represent the nondimensionalized deviations between the force curves and the approximating quadratic expressions. Figure 5 illustrates $\bar{K}^*$ and $\bar{k}^*$, respectively. Note that, although they represent forces proportional to displacement, they are not traditional stiffness coefficients since they are functions of whirl frequency ratio. Separating the force coefficients into whirl-frequency-independent and whirl-frequency-dependent terms does not introduce any approximation to the force definitions. Equations (1) are now rewritten as

$$-\begin{Bmatrix} F_x \\ F_y \end{Bmatrix} = \begin{bmatrix} M_L & 0 \\ 0 & M_L \end{bmatrix} \begin{Bmatrix} \ddot{x} \\ \ddot{y} \end{Bmatrix} + \begin{bmatrix} C_L & c_L \\ -c_L & C_L \end{bmatrix} \begin{Bmatrix} \dot{x} \\ \dot{y} \end{Bmatrix} + \begin{bmatrix} K_L + K^*(f) & k_L + k^*(f) \\ -k_L - k^*(f) & K_L + K^*(f) \end{bmatrix} \begin{Bmatrix} x \\ y \end{Bmatrix}. \tag{7}$$

In a mathematical sense, the tangential force accounted for by k^* could be modeled as a damping coefficient; however, the result of Fig. 5(*b*) confirms the wisdom of modeling the deviation of the tangential-force coefficient by a whirl-frequency-dependent cross-coupled-stiffness-coefficient. Specifically, k^* oscillates about zero and approaches zero as the inlet swirl ratio is reduced. Finally, observe that equations (7) are,

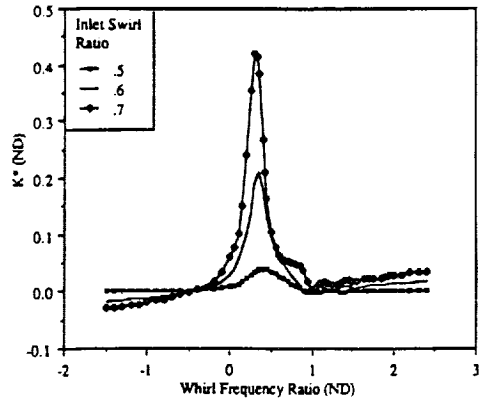

Fig. 5(*a*) Dependency of K^* on whirl frequency ratio

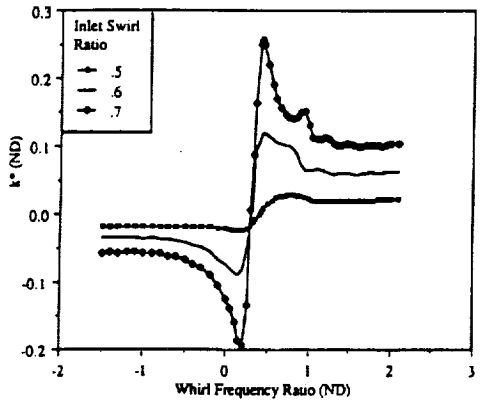

Fig. 5(*b*) Dependency of k^* on whirl frequency ratio

Table 2 Approximating coefficients for one leakage path

M_L kg	C_L Ns/m	c_L Ns/m	K_L MN/m	k_L MN/m
3.469	2037	969.9	.06781	.3137

in general, nonlinear differential equations. To understand this statement, recall that the general definition of the whirl frequency ratio, f, is given in equation (5). If the rotor precession has a constant radius and rate, f is a constant and the motion is linear. However, for general motion, f is variable and a function of the motion.

After performing the asymptotic least-squares curve fit to Fig. 2, the resulting coefficients of equation (6) are given in Table 2.

In summary, the following equations represent how the overall coefficients for the model are defined.

$$\begin{aligned} M &= M_r + 2(M_s + M_L) \\ C &= 2(C_s + C_L) + \bar{C} \\ c &= 2(c_s + c_L) \\ K &= K_{sh} + 2(2K_s + K_L) + 2K^* = \bar{K} + 2K^* \\ k &= 2(k_s + k_L) + 2k^* = \bar{k} + 2k^*. \end{aligned} \tag{8}$$

Particular coefficients are doubled because there are two seals and two leakage paths in a double suction pump. The quantity, $\bar{C}$, must be added to the model to yield reasonable stability. If the eigenvalues of the overall system are obtained without adding $\bar{C}$, the system is found to be unstable. Therefore, by adding another damping term ($\bar{C} = 10{,}422$ Ns/m), reasonable stability, which is consistent with operating pump experience, is ensured. The following equation represents the complete model used to model the forces on the rotor.

Table 3 Coefficients for overall model

$\bar{u}_{tL}$	M kg	C Ns/m	c Ns/m	K MN/m	k MN/m
.5	98.240	21208	2097.1	2.8827	1.5549
.6	98.298	18830	2119.1	2.6115	1.5494
.7	98.361	16438	2142.4	2.3363	1.5184

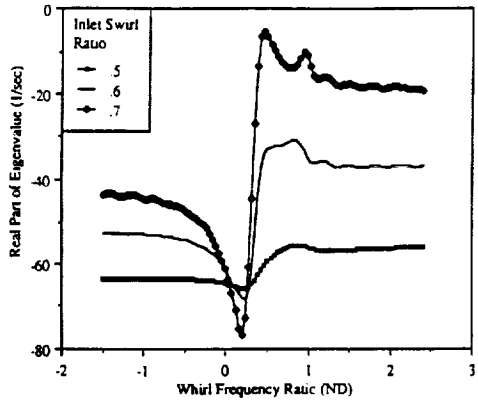

Fig. 6 Real part of the eigenvalues for the forward-whirl mode

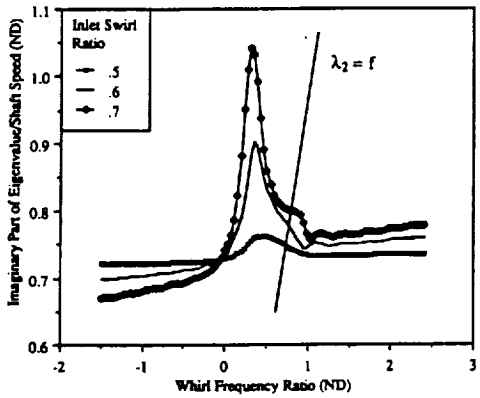

Fig. 7 Imaginary part of the eigenvalues for the forward-whirl mode

$$\begin{bmatrix} M & 0 \\ 0 & M \end{bmatrix}\begin{Bmatrix} \ddot{x} \\ \ddot{y} \end{Bmatrix} + \begin{bmatrix} C & c \\ -c & C \end{bmatrix}\begin{Bmatrix} \dot{x} \\ \dot{y} \end{Bmatrix} + \begin{bmatrix} K(f) & k(f) \\ -k(f) & K(f) \end{bmatrix}\begin{Bmatrix} x \\ y \end{Bmatrix} = \begin{Bmatrix} F_x \\ F_y \end{Bmatrix}. \quad (9)$$

Table 3 contains the numerical values for this analysis. These coefficients combine to make the damping for the uncoupled system, defined by $C/2\sqrt{KM}$, equal to 63 percent, 59 percent, and 54 percent of critical damping for the three swirl ratios shown, respectively. Again, $\bar{K}^*$ and $\bar{k}^*$ are illustrated in Fig. 5 and are defined analytically with cubic-spline curve fits.

Natural Frequency Determination

The characteristic equation for Eq. (9) is

$$[M\bar{s}^2 + C\bar{s} + K(f)]^2 + [c\bar{s} + k(f)]^2 = 0, \quad (10a)$$

where $\bar{s} = s/\omega_s$. For each whirl-frequency ratio f, two pairs of complex conjugate roots of the form

$$\bar{s} = \sigma_i \pm j\lambda_i; \quad i = 1,2 \quad (10b)$$

can be calculated corresponding to forward and backward whirling modes. The concern here is finding the natural frequency for forward whirling motion. Figure 7 illustrates the eigenvalue solutions to Eq. (10a) versus f.

Free whirl of the rotor occurs only when the imaginary part of an eigenvalue equals the whirl frequency ratio f in Fig. 7; i.e., $\lambda_2 = f$. The three points at which the $\lambda_2 = f$ line intersects the $\lambda(f)$ curves defines the forward-whirl natural frequencies for the three inlet swirl ratios. The real part of the eigenvalue at this natural frequency defines the rotor's damping.

To find the "natural frequency" and damping of free whirl, the following iterative technique has been used. First, a whirl frequency ratio is assumed. From this value, the corresponding values of K and k are obtained from the data shown in Fig. 5 from which the eigenvalues are found using Eq. (10). These first two steps are equivalent to finding a point on the curves of Figs. 6 and 7. The imaginary part of the forward-whirl eigenvalue is compared to the whirl frequency used. If they are the same, the natural frequency at which free vibration takes place is defined. If they are different, the imaginary part of the forward-whirl root becomes the assumed whirl frequency ratio, and the same steps are carried out until convergence occurs. Note that this calculation procedure yields the damped natural frequency for the system.

Table 4 Natural frequencies of free vibration for the pump model with and without K^* and k^*

$\bar{u}_{tL}$	$\frac{\omega_n}{\omega_s}$ with K^* and k^*	$\frac{\omega_n}{\omega_s}$ without K^* and k^*	Percent Decrease
.5	.747	.727	2.68%
.6	.777	.724	6.82%
.7	.800	.715	10.63%

Table 5 Real parts of the eigenvalues for the model with and without K^* and k^*

$\bar{u}_{tL}$	Real part with K^* and k^* $1/sec$	Real part without K^* and k^* $1/sec$	Percent Decrease
.5	-55.9	-60.3	7.87%
.6	-31.1	-47.2	51.80%
.7	-13.8	-34.5	150.00%

Tables 4 and 5 show results of the above algorithm. Also included are the eigenvalues of the same model neglecting K^* and k^*, which correspond to a pure quadratic approximation of the leakage path forces as in equations (4). The eigenvalues illustrate at least two important conclusions about the effects of the values of K^* and k^*. First, the natural frequency increases when K^* and k^* are included as well as when the swirl ratio is increased. The variation of K^* in Fig. 5 explains these observations. More importantly, the percent differences between the two models show that the values of K^* and k^* have very little effect on natural frequency. Second, stability is reduced when K^* and k^* are included and when the swirl ratio is increased. The variation of k^* in Fig. 5 is the cause of these observations. Finally, the percent differences between the two models shows that K^* and k^* can cause appreciable reductions in relative stability.

To show that the stability and frequency of free vibration are determined only by the root obtained from the iterative approach described earlier, the equations of motion (9) were integrated in a series of transient, free-vibration simulations. Initial conditions were an initial displacement of .127 mm (.005 in) and velocity equal to $R_L w_s$ (synchronous whirl). Figure 8 includes the resulting orbit and a time history of the whirl frequency ratio for free vibration and an inlet swirl ratio of 0.7. As shown, the rotor executed a well-damped spiral orbit.

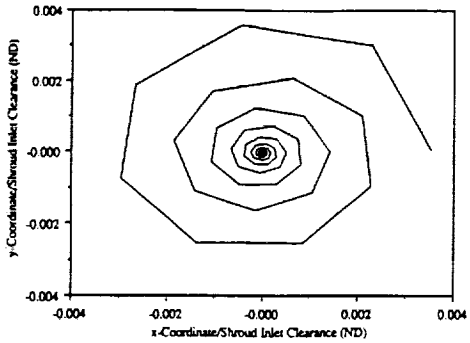

Fig. 8(a) Rotor orbit during free vibration

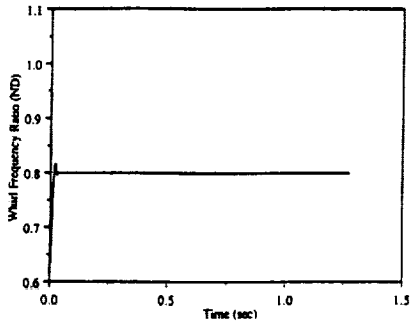

Fig. 8(b) Time history of rotor whirl frequency ratio during free vibration

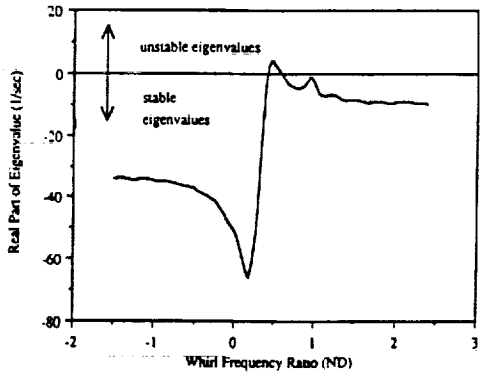

Fig. 9 Real part of the eigenvalues for the forward-whirl mode with a 12.5 percent reduction in direct damping

The whirl frequency ratio of the orbit was exactly 0.8, which corresponds to the natural frequency found earlier. The other two swirl ratios yield similar results.

To verify that the stability of the model is described only by the real part of the eigenvalues obtained with the iterative approach described above, the direct damping coefficient was reduced by 12.5 percent producing a range of unstable eigenvalues as shown in Fig. 9 where the real part of the forward-whirl root is positive between whirl frequency ratios of 0.41 and 0.57. The natural frequency of this altered model corresponds to a stable eigenvalue and is $.825w_s$. Integration of the equations of motion were altered to include a harmonic forcing function with an amplitude of 5N which forced the rotor in a circular direction at a frequency of $.5w_s$. Figure 10 includes the resulting orbit, whirl frequency ratio time history, and a Fast Fourier Transform (FFT) of the x-coordinate, respectively. Even though the forcing frequency was within the unstable range of frequencies, the figures show that the system was stable in that its orbit did not grow without bound. The loops and limit cycle behavior are the results of the nonlinearities in the model. The FFT shows that the steady state orbit consisted of response at both the forcing frequency, $.5w_s$, and the natural frequency, $.825w_s$. Other forcing frequencies were

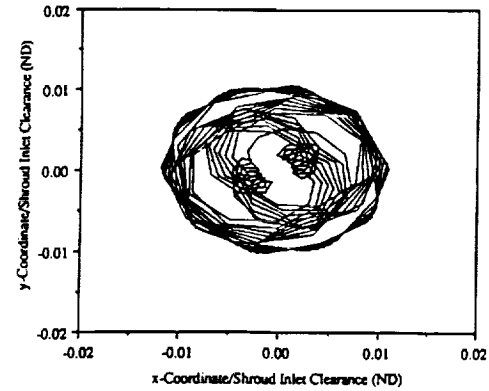

Fig. 10(a) Rotor orbit during harmonic excitation at 50 percent of shaft speed and 12.5 percent reduction in direct damping

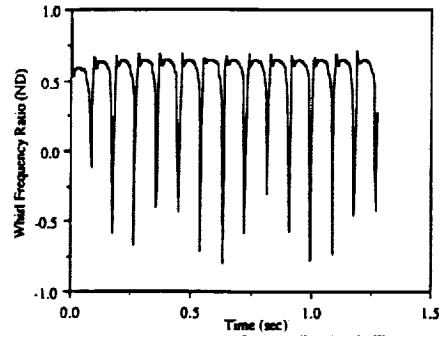

Fig. 10(b) Time history of rotor whirl frequency ratio during harmonic excitation at 50 percent of shaft speed and a 12.5 percent reduction in direct damping

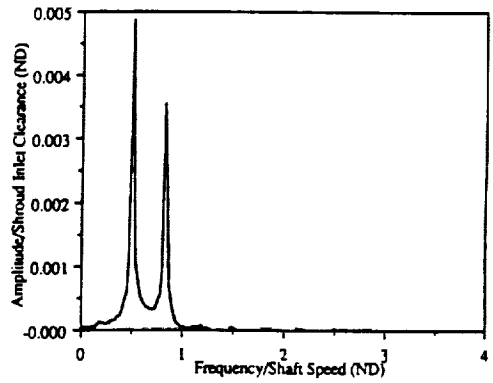

Fig. 10(c) FFT of the response of the rotor during harmonic excitation at 50 percent of shaft speed and a 12.5 percent reduction in direct damping

also tried. Using a stable value of $0.7w_s$, for example, the response did not behave in the same manner; instead, the orbit reached a steady state circular path at the excitation frequency as would be expected from a linear system. However, forcing at $.375w_s$, the characteristics of the results from forcing at $.5w_s$ occurred again, as can be seen in Fig. 11, which again contain the orbit, time history of the whirl frequency ratio and an FFT of the response. Only forcing frequencies below and within the unstable zone resulted in this behavior. Only when the direct damping coefficient was reduced until the natural frequency corresponded to an unstable eigenvalue did the response become unstable in a linear sense, where the orbit grew without bound at the natural frequency. The fundamental result from this analysis is a verification that a range of whirl frequencies yielding eigenvalues with positive real parts does not cause the system response to grow without bound unless it includes the system natural frequency. In addition, the non-

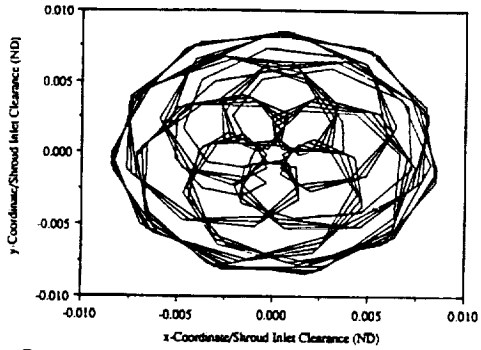

Fig. 11(*a*) Rotor orbit during harmonic excitation at 37.5 percent of shaft speed and a 12.5 percent reduction in direct damping

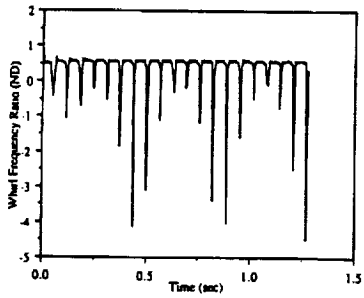

Fig. 11(*b*) Time history of rotor whirl frequency ratio during harmonic excitation at 37.5 percent of shaft speed and a 12.5 percent reduction in direct damping

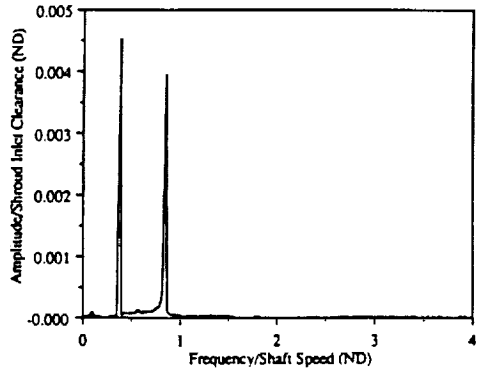

Fig. 11(*c*) FFT of the response of the rotor during harmonic excitation at 37.5 percent of shaft speed and a 12.5 percent reduction in direct damping

linearities of the system can cause a limit cycle to occur under certain conditions.

Finally, the critical speed of the rotor cannot be calculated unless force curves are available at other shaft speeds. In this case, the natural frequency is calculated with the iterative method just described, but at a number of shaft speeds. A plot of natural frequency as a function of shaft speed is then drawn, analogous to "critical speed maps" in fluid-film bearing analysis. The critical speed is defined as the speed where the natural frequency is equal to the shaft speed.

Frequency Response

As discussed earlier, the following are the equations of motion of the model

$$\begin{bmatrix} M & 0 \\ 0 & M \end{bmatrix}\begin{Bmatrix} \ddot{x} \\ \ddot{y} \end{Bmatrix} + \begin{bmatrix} C & c \\ -c & C \end{bmatrix}\begin{Bmatrix} \dot{x} \\ \dot{y} \end{Bmatrix} + \begin{bmatrix} K(f) & k(f) \\ -k(f) & K(f) \end{bmatrix}\begin{Bmatrix} x \\ y \end{Bmatrix} = F\begin{Bmatrix} \cos\Omega t \\ \sin\Omega t \end{Bmatrix}, \quad (11)$$

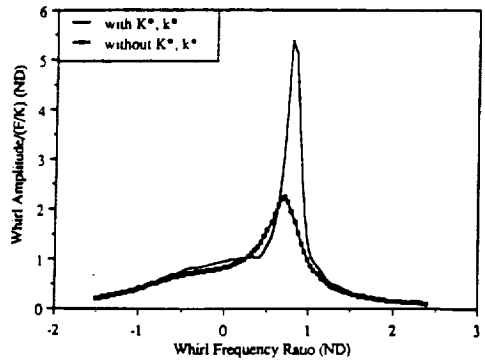

Fig. 12 Frequency response: whirl amplitude

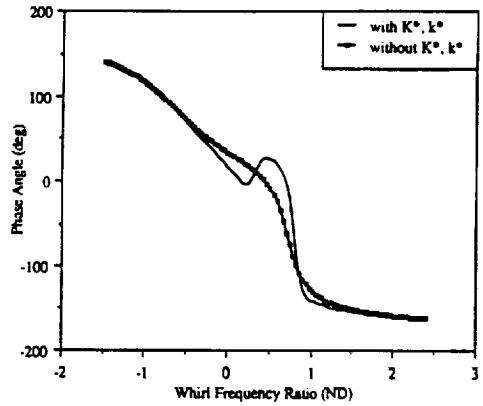

Fig. 13 Frequency response: phase angle

where the right-hand side represents a harmonic forcing function appropriate to frequency response analyses. As in traditional methods, the transient solution is assumed to decay with time, and only the steady-state response of the rotor is considered. Obviously, frequency response solutions are only valid when the system is stable, precluding the type of response illustrated in Figs. 10 and 11. The forcing frequency is defined by Ω which has been used to represent whirl speed. Since the steady-state motion is assumed to occur at the same frequency as the excitation, this should not cause confusion. Note that the model is now linear because the whirl frequency ratio and, hence, the stiffnesses are constant. Multiplying the second equation by the complex number i, the equations can be combined into one in terms of the complex variable z.

$$M\ddot{z} + (C - ic)\dot{z} + (K - ik)z = Fe^{i\Omega t}. \quad (12)$$

Assuming steady-state motion of the following form

$$z = Re^{i\phi}, \quad (13)$$

where R denotes the whirl amplitude, and ϕ is the phase angle yields

$$\frac{R}{F/K} = \frac{K}{\sqrt{[K - M\Omega^2 + c\Omega]^2 + [C\Omega - k]^2}}$$
$$\phi = \tan^{-1}\left[\frac{k - C\Omega}{K - M\Omega^2 + c\Omega}\right]. \quad (14)$$

Equations (14) were solved using the present model data, and the results for a swirl ratio of 0.7 are shown in Figs. 12 and 13. Also included are the same results for the model with K^* and k^* neglected. Again, in obtaining frequency curves as shown in Figs. 12 and 13, the stiffness terms must be calculated at the corresponding whirl frequency ratio.

The swirl ratio of 0.7, used in Figs. 12 and 13, exhibited the largest variation in amplitude and phase at the whirl frequency ratio of .80, the system natural frequency. An amplitude dif-

ference of about 60 percent is shown between the curves, suggesting that K^* and k^* have significant influence on the system primarily at this frequency. The swirl ratios of 0.6 and 0.5 exhibited similar but decreasing results in both the amplitude and phase curves, having differences in amplitude at the peak value of 35 percent and 6 percent, respectively. In fact, the curves were almost identical in the case corresponding to a swirl ratio of 0.5. Note that these resonance peaks occurred in all cases at the corresponding natural frequencies found in the previous section, further verifying the preceding results. The difference in the response to synchronous imbalance excitation ($f = 1$) between the two models is small, and this suggests that the leakage path forces have negligible effects on imbalance response. However, the presence of a subsynchronous excitation near the natural frequency can result in large increases in response amplitude when k^* is included.

Summary and Conclusions

The impeller-shroud forces have been separated into (*a*) constant (whirl frequency-independent) stiffness, damping and mass coefficients and (*b*) direct and cross-coupled added stiffness coefficients which are functions of whirl frequency. With this approach, the model can be analyzed using traditional techniques with a few modifications. A new iterative technique was used in the determination of the rotor's natural frequency and damping. The whirl-frequency-dependent stiffness terms were seen to be convenient and effective models for the impeller-shroud force nonlinearities.

When the values of the added stiffness coefficients, K^* and k^*, were included in addition to the frequency-independent coefficients, a number of effects resulted. First, the natural frequency was seen to increase by a small amount, suggesting that K^* could be neglected when only the natural frequency is important. In addition, the stability is seen to decrease when k^* is included. This effect is appreciable, so stability calculations should include k^*. The frequency response analysis showed synchronous response to imbalance is increased by the stiffnesses although by only a small amount. Appreciable differences in response due to subsynchronous excitation occur only at or near the natural frequency and become negligible at low values of the inlet swirl ratio.

The nonlinearity introduced by the whirl-frequency-dependency of the force coefficients resulted in limit cycles and nonsynchronous response in some cases.

References

Adtkins, D., 1976, "Analyses of Hydrodynamic Forces on Centrifugal Pump Impellers," M.S. Thesis, California Institute of Technology, Pasadena.

Bolleter, U., Wyss, A., Welte, I., and Sturchler, R., 1985, "Measurements of Hydrodynamic Interaction Matrices of Boiler Feed Pump Impellers," ASME, Paper No. 85-DET-148.

Bolleter, U., Leibundgut, E., Sturchler, R., and McCloskey, T., 1989, "Hydraulic Interaction and Excitation Forces of High Head Pump Impellers," presented at the ASCE/ASME Pumping Machinery Symposium, July 9–12, 1989.

Childs, D., Dressman, J., and Childs, S., 1980, "Testing of Turbulent Seals for Rotordynamic Coefficients," *Proc. of Workshop on Rotordynamic Instability Problems in High Performance Turbomachinery*, Texas A&M University, NASA CP-2133, pp. 121–38.

Childs, D., 1981, "Convergent-Tapered Annular Seals: Analysis for Rotordynamic Coefficients," Symposium Vol., Fluid/Structure Interactions Turbomach., ASMW Winter Annual Meeting, pp. 35–44.

Childs, D., 1982a, "Dynamic Analysis of Turbulent Annular Seals Based on Hirs' Lubrication Equations," ASME Paper No. 82-Lub-41.

Childs, D., 1982b, "Finite-Length Solutions for Rotordynamic Coefficients of Turbulent Annular Seals," ASME Paper No. 82-Lub-42.

Childs, D., and Dressman, J., 1982c, "Testing of Turbulent Seals for Rotordynamic Coefficients," *Proceedings of Workshop on Rotordynamic Instability Problems in High Performance Turbomachinery*, Texas A&M University, NASA CP-2250, pp. 157–71.

Childs, D., and Moyer, D., 1985, "Vibration Characteristics of the HPOTP (High Pressure Oxygen Turbopump) of the SSME (Space Shuttle Main Engine)," ASME *Journal of Engineering for Gas Turbines and Power*, Vol. 107, pp. 152–159.

Childs, D., 1987, "Fluid-Structure Interaction Forces At Pump-Impeller-Shroud Surfaces for Rotordynamic Calculations," Texas A&M University, Mechanical Engineering Dept., ASME Vibration Conference, Boston, Mass.

Childs, D., 1990, "Centrifugal-Acceleration Modes for Incompressible Fluid in the Leakage Analysis Between a Shrouded Pump Impeller and Its Housing," ASME JOURNAL OF VIBRATION AND ACOUSTICS, May 1990.

Franz, R., and Arndt, N., 1986, "Measurement of Hydrodynamic Forces on the Impeller of the SSME," Report No. E249.2, California Institute of Technology, Pasadena.

Jeffcott, H., 1919, "The Lateral Vibration of Loaded Shafts in the Neighborhood of a Whirling Speed—The Effect of Want of Balance," The Philosophical Magazine, Vol. 6, No. 37, pp. 304–314.

Jery, B., Acosta, J., Brennen, C., and Caughey, T., 1984, "Hydrodynamic Impeller Stiffness, Damping and Inertia In the Rotordynamics of Centrifugal Flow Pumps," *Proceedings of Workshop on Rotordynamic Instability Problems in High Performance Turbomachinery*, Texas A&M University, NASA CP-2338, pp. 137–160.

Massey, I. C., 1985, "Subsynchronous Vibration Problems in High Speed Multistage Centrifugal Pumps," *Proceedings of the 14th Turbomachinery Symposium*, Turbomachinery Laboratories, Texas A&M University, pp. 11–16.

Childs, D.
(1992b)

Reprinted from March 1992, Vol. 114, Journal of Fluids Engineering

Pressure Oscillation in the Leakage Annulus Between a Shrouded Impeller and Its Housing Due to Impeller-Discharge-Pressure Disturbances

D. W. Childs
Turbomachinery Laboratories,
Mechanical Engineering Department,
Texas A&M University,
College Station, Texas 77843

An analysis is presented for the perturbed flow in the leakage path between a shrouded-pump impeller and its housing caused by oscillations in the impeller-discharge pressure. A bulk-flow model is used for the analysis consisting of the path-momentum, circumferential-momentum, and continuing equations. Shear stress at the impeller and housing surfaces are modeled according to Hirs' turbulent lubrication model. In the present analysis, perturbations of the impeller discharge pressure are used to excite the fluid annulus. The circumferential variation of the discharge pressure is expanded in a Fourier series up to order n_1, where n_1 is the number of impeller blades. A precession of the impeller wave pattern in the same direction or opposite to pump rotation is then assumed to completely define the disturbance excitation. Predictions show that the first (lowest-frequency) "centrifugal-acceleration" mode of the fluid within the annulus has its peak pressure amplitude near the wearing-ring seal. Pressure oscillations from the impeller can either be attenuated or (sharply) magnified depending on: (a) the tangential velocity ratio of the fluid entering the seal, (b) the order of the fourier coefficient, and (c) the closeness of the precessional frequency of the rotating pressure field to the first natural frequency of the fluid annulus, and (d) the clearance in the wearing-ring seal.

Introduction

The present work is stimulated by experiences with the SSME HPFTP (Space Shuttle Main Engine, High Pressure Fuel Turbopump) wearing-ring seals. A stepped, 3-cavity, tooth-on-rotor, labyrinth-seal design is used. The stator for the seal is made from KEL-F, a plastic that is somewhat similar to nylon. In some cases, post-test inspection of the stator element has revealed that interior points in the stator material have melted and then resolidified, despite being in contact with liquid hydrogen. One hypothesis for this exceptional outcome was that the material had been subjected to cyclical stresses which generated heat due to hysteresis. Because of poor conduction properties of the material, the heat could not be dissipated, the temperature rose, and melting resulted. "What pressure oscillations are driving the cyclical stresses?", is an obvious question in reviewing this scenario. The present analysis examines "centrifugal-acceleration" modes, arising between the impeller shroud and its housing and driven by pressure oscillations from the pump, as an answer to this question.

Figure 1 illustrates an impeller stage of a multi-stage centrifugal pump. Leakage along the front side of the impeller, from impeller discharge to inlet, is restricted by a wearing-ring seal, while leakage along the back side is restricted by either an interstage seal or a balance-piston discharge seal. The present analysis considers perturbed flow in the leakage paths between the impeller-shroud surface and its housing.

Prior analyses by the author of those annulli have been concerned with lateral (1987, 1989) and axial (1990a) reaction forces developed by the impeller shrouds as a consequence of harmonic clearance changes due to impeller motion. These analyses have been based on "bulk-flow" models which neglect the variation in the dependent variables across the fluid film. The model consists of the path and circumferential momentum equations and the continuity equations.

The analyses cited have yielded force and moment coefficients due to impeller motion but have also predicted "resonance" phenomena, which are caused by the centrifugal-acceleration body forces present in the path momentum equations. An algorithm was developed (1990b) to calculate the complex eigenvalues and eigenvectors associated with these resonances. In the present analysis, the harmonic response of the flow within the annulus is examined due to time and circumferential variations in the discharge pressure of the impeller.

[1]The work reported herein was supported by NASA Marshall Space Flight Center under contract NAS 8-37821; contract technical monitor: James Cannon.
Contributed by the Fluids Engineering Division for publication in the JOURNAL OF FLUIDS ENGINEERING. Manuscript received by the Fluids Engineering Division August 20, 1990.

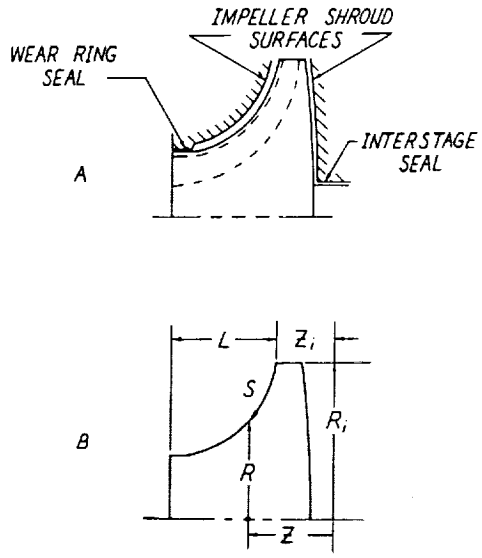

Fig. 1 Impeller leakage paths

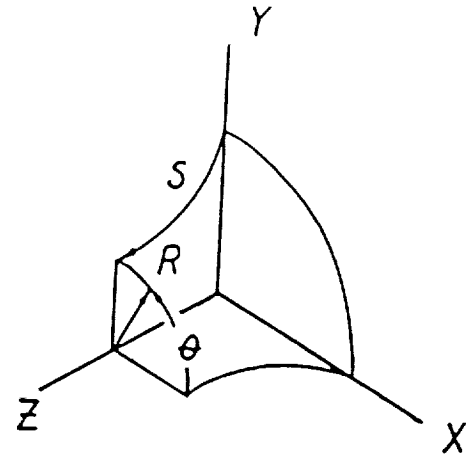

Fig. 2 Impeller surface geometry

Geometry and Kinematics

Figure 1 illustrates the annular leakage paths along the front and back sides of a typical shrouded impeller of a multistage centrifugal pump. The present discussion concentrates on the flow and pressure fields within the forward annulus; however, the analysis can also be applied to the rear annulus.[2] As illustrated in Fig. 2, the outer surface of the impeller is a surface of revolution formed by rotating the curve $R = R(Z)$ about the Z axis. A point on the surface may be located by the coordinates $Z, R(Z), \theta$. The length along the curve $R(Z)$ from the initial point R_i, Z_i to an arbitrary point R, Z is denoted by S and defined by

$$S = \int_{Z_i}^{Z} \sqrt{1 + \left(\frac{dR}{dZ}\right)^2}\, du = \int_{R_i}^{R} \sqrt{1 + \left(\frac{dZ}{dR}\right)^2}\, du \qquad (1)$$

In the equations which follow, the path coordinate S and angular coordinate θ are used as independent spatial variables. The coordinates Z, R defining the impeller surface are expressed as parametric functions of S, i.e., $Z(S)$, $R(S)$. The length of the leakage path along the impeller face is defined by

$$L_s = \int_{Z_i}^{Z_i + L} \sqrt{1 + \left(\frac{dR}{dZ}\right)^2}\, du \qquad (2)$$

Governing Equations

Returning to Fig. 2, the path coordinate S and circumferential coordinate $R\theta$ are used to locate a fluid differential

[2]Although the leakage flow is normally up the backside of all impellers except the last impeller, the governing equations would continue to be valid irrespective of the flow direction.

Nomenclature

A_{2s}, A_{3s}, $A_{2\theta}$, $A_{3\theta}$ = coefficients introduced in Eq. (12)
$b = V_i/R\omega$ = nondimensional velocity ratio
C_{de} = discharge coefficient for the exit wear-ring seal introduced in Eq. (7)
C_i = initial (s = 0) clearance (L)
C_r = exit seal clearance (L)
$f = \Omega/\omega$ = nondimensional precession frequency
f^* = nondimensionalized precession frequency yielding a maximum response pressure
$f^{+1} = \dfrac{n_1}{(n_1 - n_2)}$ = positive, dominant, nondimensional, precession frequency predicted for an impeller with n_1 blades in a diffuser with n_2 blades
$h = H/C_i$ = nondimensionalized clearance
H = clearance between impeller shroud and housing (L)
L_s = leakage-path length, defined by Eq. (2), (L)
n = order of Fourier coefficient, introduced in Eq. (13).
$p = P/\rho V_i^2$ = nondimensional static fluid pressure
$p_s(\theta,t)$ = prescribed annulus supply pressure (impeller exit pressure)
$p_e(\theta,t)$ = prescribed annulus exit pressure (impeller inlet pressure)
P = fluid static pressure (F/L^2)
R = radial coordinate (L)
R_i = initial (s = 0) radius (L)
$r = R/R_i$ = nondimensionalized radial coordinate
$R_s = 2HU_s/\nu$ = path-velocity Reynolds number
S = path coordinate introduced in Eq. (1), (L)
$s = S/L_s$ = nondimensionalized path length
$T = L_s/V_i$ = representative transit time for fluid traversing the leakage path (T)
$u_s = U_s/V_i$ = nondimensionalized path fluid velocity
$u_\theta = U_\theta/R_i\omega$ = nondimensionalized circumferential fluid velocity
V_i = initial (s = 0) path fluid velocity
ϵ = perturbation coefficient
ω = pump running speed (T^{-1})
Ω = excitation frequency (T^{-1})
ρ = fluid density (M/L^3)
θ = circumferential coordinate
σ_r, σ_s = normalized friction factors, defined by Eq. (11)
$\tau = \tau t$ = nondimensionalized time
ξ = entrance-loss coefficient introduced in Eq. (7)
ν = kinematic viscosity (L^2T^{-1})

Overbars denote complex variables; see Eq. (16). Subscripts 0 and 1 denote zeroth- and first-order solutions, respectively.

element of thickness $H(S, \theta, t)$. From Childs (1987), the continuity equation can be stated

$$\frac{\partial H}{\partial t}+\frac{\partial}{\partial S}(U_s H)+\frac{1}{R}\frac{\partial}{\partial \theta}(U_\theta H)+\left(\frac{H}{R}\right)\frac{\partial R}{\partial S}U_s=0 \quad (3a)$$

where U_s and U_θ are the path and circumferential bulk-velocity components, respectively. The path and circumferential momentum equations are stated

$$-H\frac{\partial P}{\partial S}=\tau_{ss}+\tau_{sr}-\rho H\frac{U_\theta^2}{R}\frac{dR}{dS}+\rho H\left(\frac{\partial U_s}{\partial t}+\frac{\partial U_s}{\partial \theta}\frac{U_\theta}{R}+\frac{\partial U_s}{\partial S}U_s\right) \quad (3b)$$

$$-\frac{H}{R}\frac{\partial P}{\partial \theta}=\tau_{\theta s}+\tau_{\theta r}+\rho H\left(\frac{\partial U_\theta}{\partial t}+\frac{\partial U_\theta}{\partial \theta}\frac{U_\theta}{R}+\frac{\partial U_\theta}{\partial S}U_s+\frac{U_\theta U_s}{R}\frac{\partial R}{\partial S}\right) \quad (3c)$$

Following Hirs' approach (1973), the wall shear-stress definitions in these equations can be stated

$$\tau_{ss}=\frac{ns}{2}\rho U_s^2 R_s^{ms}[1+(U_\theta/U_s)^2]^{\frac{ms+1}{2}}$$

$$\tau_{sr}=\frac{nr}{2}\rho U_s^2 R_s^{mr}\{1+[(U_\theta-R\omega)/U_s]^2\}^{\frac{mr+1}{2}}$$

$$\tau_{\theta s}=\frac{ns}{2}\rho U_\theta U_s R_s^{ms}[1+(U_\theta/U_s)^2]^{\frac{ms+1}{2}}$$

$$\tau_{\theta r}=\frac{nr}{2}\rho U_s(U_\theta-R\omega)R_s^{mr}\{1+[(U_\theta-R\omega)/U_s]^2\}^{\frac{mr+1}{2}} \quad (4)$$

where

$$R_s=2HU_s/\nu \quad (5)$$

Nondimensionalization and Perturbation Analysis

The governing equations define the bulk-flow velocity components (U_s, U_θ) and the pressure P as a function of the coordinates ($R\theta$, S) and time, t. They are conveniently nondimensionalized by introducing the following variables

$$u_s=U_s/V_i, \quad u_\theta=U_\theta/R_i\omega, \quad p=P/\rho V_i^2$$

$$s=S/L_s, \quad r=R/R_i, \quad b=V_i/R_i\omega$$

$$\tau=\omega t, \quad T=L_s/V_i \quad (6)$$

The present analysis examines the changes in (u_s, u_θ, p) due to changes in the impeller's discharge or inlet pressure. Following conventional notation, pressure drops at the annulus inlet and exit are stated

$$P_s(\theta,t)-P(0,\theta,t)=\rho(1+\xi)U_s^2(0,\theta,t)/2$$

$$P(L_s,\theta,t)-P_e(\theta,t)=\rho C_{de}U_s^2(L_s,\theta,t)/2 \quad (7)$$

Note specifically that the (upstream) supply and (downstream) exit pressure are now functions of time. Assume that the oscillations consist of a small perturbation of the form

$$P_s(\theta,t)=P_{s0}+\epsilon P_{s1}(\theta,t), P_e(\theta,t)=P_{e0}+\epsilon P_{e1}(\theta,t)$$

and introduce nondimensional variables to yield the following zeroth

$$p_0(0)=p_{s0}-(1-\xi)/2$$

$$p(1)=p_{es}+C_{de}u_{s0}^2(1)/2 \quad (8)$$

and first-order equations

$$p_{s1}(\theta,t)-p_1(0,\theta,t)=(1+\xi)u_{s1}(0,\theta,t)$$

$$p_1(1,\theta,t)-p_{e1}(\theta,t)=C_{de}u_{s0}(1)u_{s1}(1,\theta,t) \quad (9)$$

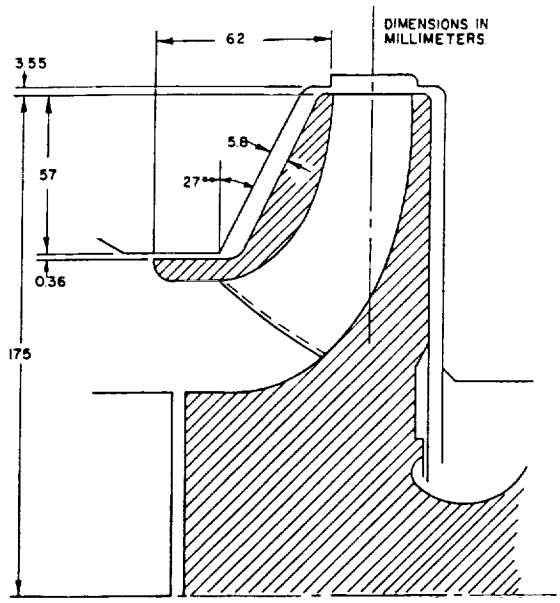

Fig. 3 Example impeller; Bolleter et al. (1987)

The perturbed supply and exit pressures $p_{s1}(\theta,t)$, $p_{e1}(\theta,t)$ can now be specified functions of time and provide excitation for the perturbed flowfield within the annulus.

Expansion of the dependent variables of Eq. (3) in perturbation equations yields:

Zeroth-Order Equations

(a) Path-Momentum Equation

$$\frac{dp_o}{ds}-\frac{1}{r}\left(\frac{dr}{ds}\right)\frac{u_{\theta o}^2}{b^2}+\left[\left(\frac{\sigma_r+\sigma_s}{2}\right)-\frac{1}{h_o}\frac{dh_o}{ds}-\frac{1}{r}\frac{dr}{ds}\right]u_{so}^2=0 \quad (10a)$$

(b) Circumferential-Momentum Equation

$$\frac{du_{\theta o}}{ds}+\frac{u_{\theta o}}{r}\frac{dr}{ds}+[\sigma_r(u_{\theta o}-r)+\sigma_s u_{\theta o}]/2=0 \quad (10b)$$

(c) Continuity Equation

$$rh_o u_{so}=1 \quad (10c)$$

The quantities σ_s and σ_r are defined by

$$\sigma_s=(L_s/H_o)\lambda_s, \quad \sigma_r=(L_s/H_o)\lambda_r \quad (11)$$

where λ_s and λ_r are the dimensionless stator and rotor friction factors:

$$\lambda_s=nsR_{so}^{ms}[1+(u_{\theta o}/bu_{so})^2]^{\frac{ms+1}{2}}$$

$$\lambda_r=nrR_{so}^{mr}\{1+[(u_{\theta o}-r)/bu_{so}]^2\}^{\frac{mr+1}{2}}$$

The continuity equation has been used to eliminate du_{so}/ds from Eq. (10a). The momentum equations define the pressure and velocity distributions for a centered impeller position. They are coupled and nonlinear and must be solved iteratively. The initial condition for $u_{\theta o}(0)$ is obtained from the exit flow condition of the impeller. Zeroth-order pressure boundary conditions are provided by Eq. (8).

Figure 3 illustrates the pump-impeller and shroud geometry used by Bolleter et al. (1987) in their test program for radial force coefficients. Their tests were at best efficiency point (BEP) with the pump running at 2000 rpm, while developing 68m of head and 130l/s of flow rate. The impeller has seven blades and an impeller exit angle of 22.5°. The test fluid is water at 26.6°C. For the present study, ΔP across the impeller is assumed to be 70 percent of the total head rise of the stage. Based on pitot-tube measurements, impeller-exit-tangential velocity is about 50 percent of the impeller discharge surface velocity; hence, $u_{\theta 0} \equiv 0.5$.

Table 1 Zeroth-order-solution results; C_i = 3.5mm, C_r = 0.36mm

$u_{\theta 0}(0)$	0.5	0.6	0.7
R_{s0}	9377	8907	8426
C_{de}	2.068	2.098	2.130
$\dot{m}$ (kg/sec)	4.448	4.225	3.997

Table 1 provides the zeroth-order solutions for new (original-clearance) exit wearing-ring seals. The R_{s0} values on the order of 10,000 are low in comparison to the circumferential Reynolds number $R_{\theta 0} = 2HU_{\theta 0}/\nu$ which varies along the path, but is on the order of 250,000. These leakage results were obtained iteratively starting with guessed values for the seal inlet values of pressure and tangential velocities and yielding an initial estimate for C_{de}. With this estimate for C_{de}, the leakage is calculated through the annulus which yields new inlet conditions for the seal. Solutions are "bounced" back and forth between the seal and the annulus until the same leakage value is obtained for both flow paths (four-place accuracy).

First-Order Equations

(*a*) Path-Momentum Equation

$$\frac{\partial p_1}{\partial s} + u_{\theta 1}A_{2s} + u_{s1}A_{3s} + \left[\omega T \frac{\partial u_{s1}}{\partial \tau} + \omega T \frac{u_{\theta o}}{r}\frac{\partial u_{s1}}{\partial \theta} + u_{so}\frac{\partial us_1}{\partial s}\right] = 0 \quad (12a)$$

(*b*) Circumferential-Momentum Equation

$$b\frac{L_s}{R_i}\frac{1}{r}\frac{\partial p_1}{\partial \theta} + u_{\theta 1}A_{2\theta} + u_{s1}A_{3\theta} + \left[\omega T \frac{\partial u_{\theta 1}}{\partial \tau} + \omega T \frac{u_{\theta o}}{r}\frac{\partial u_{\theta o}}{\partial \theta} + u_{so}\frac{\partial u_{\theta 1}}{\partial s}\right] = 0 \quad (12b)$$

(*c*) Continuity Equation

$$\frac{\partial u_{s1}}{\partial s} + \frac{\omega T}{r}\frac{\partial u_{\theta 1}}{\partial \theta} + u_{s1}\left(\frac{1}{r}\frac{dr}{ds} + \frac{1}{h_o}\frac{dh_o}{ds}\right) = 0 \quad (12c)$$

New coefficients in these equations are defined in, Childs (1987).

Solution Procedure: First-Order Equations

The functions $p_{s1}(\theta, t)$, $p_{e1}(\theta, t)$ provide the boundary excitation for the first-order equations. The general form for the excitation takes the form

$$p_{s1}(\theta,t) = e^{j\Omega t}(p_{s1c}\cos n\theta + p_{s1s}\sin n\theta)$$
$$p_{e1}(\theta,t) = e^{j\Omega t}(p_{e1c}\cos n\theta + p_{e1s}\sin n\theta) \quad (13)$$

where n can reasonably be expected to vary from zero (plane wave) upwards through multiples of the number of blades in the impeller. The form of Eq. (13) suggests that the θ variation in boundary pressures is defined in an impeller-fixed coordinate system, which is precessing at the frequency Ω.

The θ and time dependency of the dependent variables is eliminated by assuming the comparable, separation-of-variable, solution format

$$u_{s1} = e^{jf\tau}(u_{s1c}\cos n\theta + u_{s1s}\sin n\theta)$$
$$u_{\theta 1} = e^{jf\tau}(u_{\theta 1c}\cos n\theta + u_{\theta 1s}\sin n\theta)$$
$$p_1 = e^{jf\tau}(p_{1c}\cos n\theta + p_{1s}\sin n\theta) \quad (14)$$

where the coefficients are solely functions of s, and

$$f = \Omega/\omega \quad (15)$$

is the normalized precession frequency. Substituting into Eqs. (12) and equating like coefficients of cos $n\theta$ and sin $n\theta$ yields six first-order equations in s. Introducing the complex variables

$$\bar{u}_{s1} = u_{s1c} + ju_{s1s}, \quad \bar{u}_{\theta 1} = u_{\theta 1c} + ju_{\theta 1s} \quad \bar{p}_1 = p_{1c} + jp_{1s} \quad (16)$$

reduces these real equations to three, complex, ordinary differential equations

$$\frac{d}{ds}\begin{Bmatrix}\bar{u}_{s1}\\ \bar{u}_{\theta 1}\\ \bar{p}_1\end{Bmatrix} + [A(n,f,s)]\begin{Bmatrix}\bar{u}_{s1}\\ \bar{u}_{\theta 1}\\ \bar{p}_1\end{Bmatrix} = 0 \quad (17)$$

where

$$[A] = \begin{bmatrix} B & -jn\omega t/r & 0 \\ A_{3\theta}/u_{s0} & (A_{2\theta} + j\Gamma T)/u_{s0} & -j\dfrac{nb}{ru_{s0}}\left(\dfrac{Ls}{Ri}\right) \\ A_{3s} - Bu_{s0} + j\Gamma T & \left(A_{2s} + j\dfrac{n\omega T}{r}u_{s0}\right) & 0 \end{bmatrix} \quad (18)$$

$$B = \frac{1}{r}\frac{dr}{ds} + \frac{1}{h_0}\frac{dh_0}{ds}, \quad \Gamma = \omega\left(f - n\frac{u_{\theta 0}}{r}\right) \quad (19)$$

Since there is no right-hand side to Eq. (17), the homogeneous solution is the complete solution and can be stated as follows in terms of the transition matrix and initial conditions

$$\begin{Bmatrix}\bar{u}_{s1}\\ \bar{u}_{\theta 1}\\ \bar{p}_1\end{Bmatrix} = [\Phi(n,f,s)]\begin{Bmatrix}\bar{u}_{s1}(0)\\ \bar{u}_{\theta 1}(0)\\ \bar{p}_1(0)\end{Bmatrix} \quad (20)$$

The inlet initial condition $\bar{u}_{\theta 1}(0)$ is set equal to zero, and calculation of $\bar{u}_{s1}(0)$ and $\bar{p}_1(0)$ in terms of the specified boundary conditions is the immediate problem at hand. Substitution from Eqs. (13) and (14) into Eq. (9) yields

$$\bar{p}_{s1} - \bar{p}_1(0) = (1+\xi)\bar{u}_{s1}(0)$$
$$\bar{p}_1(1) - \bar{p}_{e1} = C_{de}u_{s0}(1)\bar{u}_{s1}(1) \quad (21)$$

where

$$\bar{p}_{s1} = p_{s1c} + jp_{s1s}$$
$$\bar{p}_{e1} = p_{e1c} + jp_{e1s} \quad (22)$$

From Eq. (20)

$$\bar{u}_{s1}(1) = \Phi_{11}(1)\bar{u}_{s1}(0) + \Phi_{13}(1)\bar{p}_1(0)$$
$$\bar{p}_1(1) = \Phi_{31}(1)\bar{u}_{s1}(0) + \Phi_{33}(1)\bar{p}_1(0) \quad (23)$$

Hence, from Eq. (21) one obtains

$$\begin{bmatrix} (1+\xi) & 1 \\ \Phi_{31}(1 - C_{de}u_{s0}(1)\Phi_{11}(1) & \Phi_{33}(1) - C_{de}u_{s0}(1)\Phi_{13}(1) \end{bmatrix} \times \begin{Bmatrix}\bar{u}_{s1}(0)\\ \bar{p}_1(0)\end{Bmatrix} = \begin{Bmatrix}\bar{p}_{s1}\\ \bar{p}_{e1}\end{Bmatrix} \quad (24)$$

Inversion of this equation yields

$$\begin{Bmatrix}\bar{u}_{s1}(0)\\ \bar{p}_1(0)\end{Bmatrix} = \begin{bmatrix} Z_{11} & Z_{12} \\ Z_{21} & Z_{22}\end{bmatrix}\begin{Bmatrix}\bar{p}_{s1}\\ \bar{p}_{e1}\end{Bmatrix} \quad (25)$$

$\bar{p}_{s1}$ and $\bar{p}_{e1}$ cannot be specified independently, and a relationship between the two cannot be established without a knowledge of the fluid system beyond the current terminating orifices. For the purposes of this discussion, the arbitrary choice

$$\bar{p}_{s1} = 1, \quad \bar{p}_{e1} = 0$$

is made to examine the influence of pressure perturbations at the impeller exit (annulus inlet). The resulting set of initial conditions for Eq. (20) is then

$$\begin{Bmatrix}\bar{u}_{s1}(0)\\ \bar{p}_1(0)\end{Bmatrix} = \begin{Bmatrix}Z_{11}\\ Z_{21}\end{Bmatrix}, \quad \bar{u}_{\theta 1}(0) = 0 \quad (26)$$

The complete solution along the impeller is found by evaluating Eq. (20) for $s \in [0, 1]$.

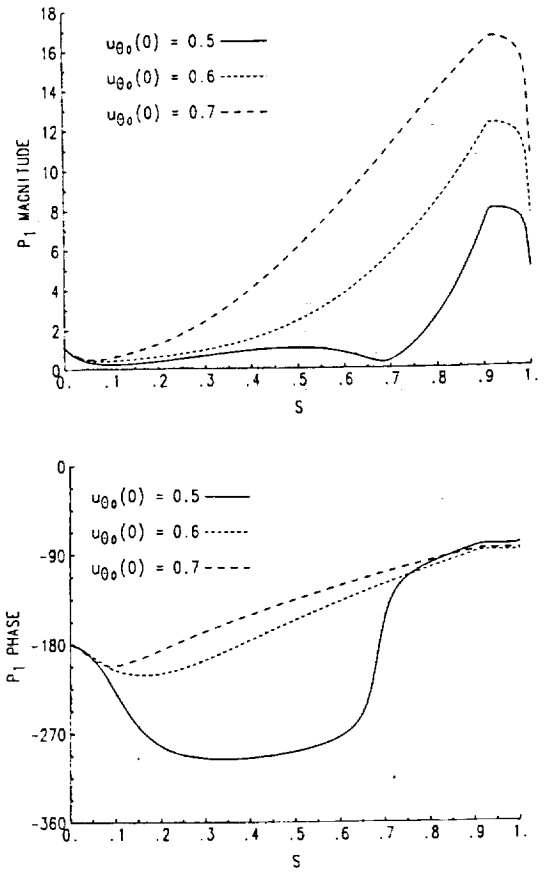

Fig. 4 $\bar{p}_1(s)$ complex eigenvector from Childs (1990b); n = 1

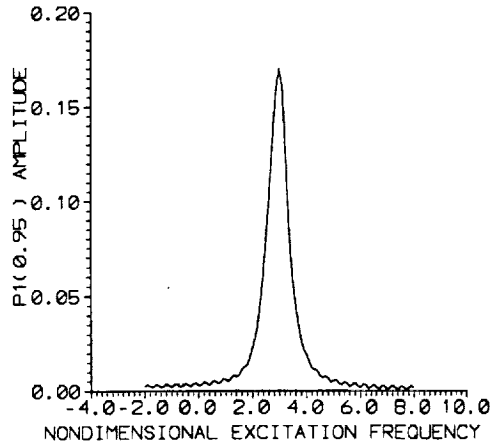

Fig. 5(a) $|\bar{p}_1(0.95)|$ versus f; C_r = 0.36mm, $u_{\theta 0}(0)$ = 0.5, n = 5

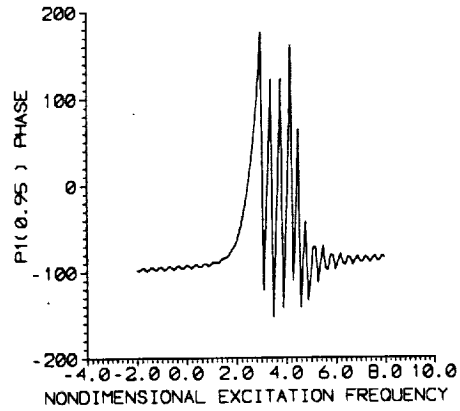

Fig. 5(b) Phase $\bar{p}_1(0.95)$ versus f; C_r = 0.36mm, $u_{\theta 0}(0)$ = 0.5, n = 5

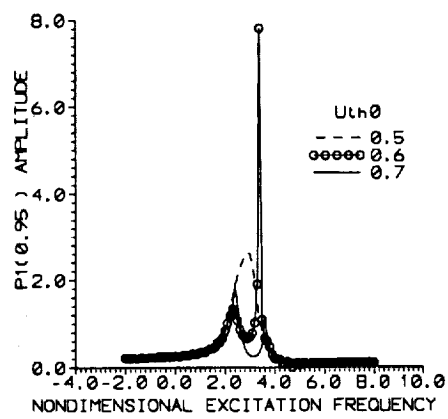

Fig. 6 $|\bar{p}_1(0.95)|$ versus f; C_r = 0.36mm, n = 5, and $u_{\theta 0}(0)$ = 0.5, 0.6, and 0.7.

Numerical Results. Childs' (1990b) analysis yields complex eigenvalues $\bar{\alpha}$ and eigenvectors $\bar{u}_{s1}(s)$, $\bar{u}_{\theta 1}(s)$, $\bar{p}_1(s)$ for the system modeled by Eq. (12). Figure 4 illustrates the amplitude and phase for the first (lowest-natural-frequency) eigenvalue for n = 1; $u_{\theta 0}(0)$ = 0.5, 0.6, and 0.7. Observe that the peak-pressure amplitudes lie near the wearing-ring seal, which is consistent with the internally-melted HPFTP wearing-ring-seal results cited earlier. Forced, harmonic-response solutions developed in this study due to impeller-discharge-pressure oscillations also show the largest pressure oscillations to occur near the wearing-ring seal (s = 0.95); hence, results presented here focus on $\bar{p}_1(0.95)$. This peak-pressure-oscillation location is very near the exit-wearing-ring seal of Fig. 3. The first question to be addressed here is, "How does $\bar{p}_1(0.95)$ depend on n, f, and C_r?"

Figure 5 illustrates the amplitude and phase of $\bar{p}_1(0.95)$ versus f for C_r = 0.36mm, n = 5, and $u_{\theta 0}$ = 0.5. As will be explained later, the choice n = 5, arises because of the number of impeller and diffuser blades used in Bolleter et al.'s (1987) pump. The phase results indicate that numerous resonances exist for positive values of f. However, only the first resonance experiences significant amplification. The remaining fluid modes are heavily damped.

Figure 6 illustrates $|\bar{p}_1(0.95)|$ for C_r = 0.36mm, n = 5, and $u_{\theta 0}(0)$ = 0.5, 0.6, and 0.7. The peak-response frequency increases as $u_{\theta 0}(0)$ is increased from 0.5 to 0.6, and a secondary peak appears around f = 2.5. Increasing $u_{\theta 0}(0)$ from 0.6 to 0.7 causes an additional peak to appear.

Figure 7 illustrates $|\bar{p}_1(0.95)|$ for C_r = 0.36mm, $u_{\theta 0}(0)$ = 0.5, and n = 0, 1, 3, 5, and 7. The response is heavily damped for n = 0, rises sharply as n is increased to one, but then remains relatively constant as n ranges upwards over 3, 5, and 7. Figure 8 repeats the results of Fig. 7, except for worn clearances; i.e., C_r = 0.72mm. Comparisons of Figs. 7 and 8 show that doubling the clearances reduces pressure amplification and slightly elevates the peak-amplitude-excitation frequency f^*. Table 2 shows f^* versus n for the new(C_r = 0.36mm) and worn seals(C_r = 0.72mm). Note that f^* increases more-or-less linearly with increasing n.

The questions which now arise are: **In a real pump, what value of n is likely to arise in impeller-pressure-discharge patterns, and what precession frequency is most likely to be present and dominant?** Answers to these questions have been provided by Bolleter (1988), who presents an analysis for the pressure waves developed by the interaction of impeller and diffuser vanes or impeller vanes and volutes. For an impeller with n_1 vanes and a diffuser with n_2 vanes, Bolleter shows that a rotating pressure wave is developed around the impeller exit with $n = |n_1 - n_2|$ diametral nodes. If $n_1 > n_2$ the pressure wave rotates in the direction of the pump with the frequency $n_1\omega/$

Table 2 f^* (peak-excitation-amplitude frequency) versus n for $u_{\theta 0}(0) = 0.5$

n	1	2	3	4	5	6	7
C_r = 0.36mm	0.3	0.8	1.4	2.1	2.9	3.6	4.2
C_r = 0.72mm	0.3	0.9	1.6	2.4	3.1	3.8	4.4

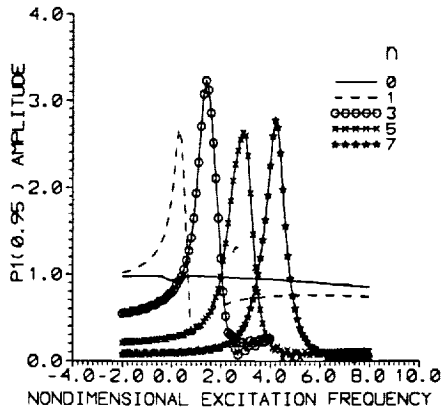

Fig. 7 $|\bar{p}_1(0.95)|$ versus f for n = 0, 1, 3, 5, 7; C_r = 0.36mm, and $u_{\theta 0}(0)$ = 0.5

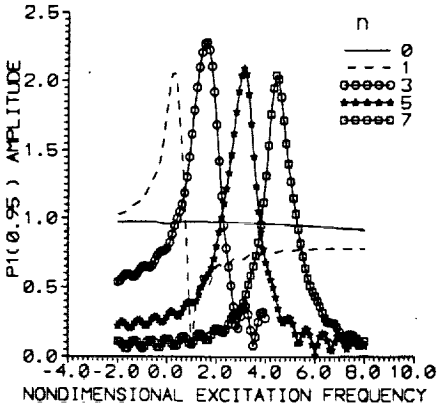

Fig. 8 $|\bar{p}_1(0.95)|$ versus f for n = 0, 1, 3, 5, 7; C_r = 0.72mm, and $u_{\theta 0}(0)$ = 0.5

n. If $n_1 < n_2$ the precessional frequency is $-n_1\omega/n$. Note that n, the number of diametral nodes, cited by Bolleter is the same n used in Eq. (13) for the pressure excitation. Further, in terms of Eq. (13), $\Omega = \pm n_1\omega/|n_1 - n_2|$. Tyler and Sofrin (1962) earlier developed this same result in analyzing the noise generated by the interaction of a rotor and stator in axial compressors of gas turbines.

Bolleter et al.'s pump (1987) used 12 diffuser blades, and the impeller of Fig. 3 has 7 blades. Hence, from Bolleter (1988), $n = |7 - 12| = 5$, and $\Omega = -7\omega/5 = -1.4\omega$. If the impeller were mounted in a double volute, $n = |7 - 2| = 5$, and $\Omega = 7\omega/5 = 1.4\omega$. From Fig. 5 ($n = 5$, $u_{\theta 0}(0) = 0.5$), amplification for $f = -1.4$ and 1.4 is 0.23 and 0.5, respectively. Hence, pressure disturbances from the impeller would generate pressure oscillations about twice as large in a double volute as in a 12-vaned diffuser. However, in either case, because the predominant frequency is well removed from the peak-amplitude-excitation frequency $f^* = 2.9$, impeller pressure disturbances would actually be attenuated by the annulus.

From Bolleter's equations, and the results of Figs. 5 through 7, significant amplification of impeller-discharge-pressure variations will only arise when the number of impeller blades exceeds the number of diffuser (or volute) blades, yielding a positive normalized precession frequency.

$$f^+ = n_1/n = n_1/(n_1 - n_2) \tag{27}$$

Table 3 Dominant normalized precession frequency f^+ and peak-excitation-amplitude frequency f^* versus n_1 and n_2; $u_{\theta 0}(0) = 0.5$

n_1	n_2	n	f^+	f^* (C_r=0.36mm)	f^* (C_r=0.72mm)
8	1	7	1.14	4.2	4.4
	2	6	1.33	3.6	3.8
	3	5	1.60	2.9	3.1
	4	4	2.0	2.1	2.4
	5	3	2.67	1.4	1.6
	6	2	4	0.8	0.9
	7	1	8	0.3	0.3
7	1	6	1.16	3.6	3.8
	2	5	1.40	2.9	3.1
	3	4	1.75	2.1	2.4
	4	3	2.33	1.4	1.6
	5	2	3.5	0.8	0.9
	6	1	7.0	0.3	0.3
6	1	5	1.2	2.9	3.1
	2	4	1.5	2.1	2.4
	3	3	2.0	1.4	1.6
	4	2	3.0	0.8	0.9
	5	1	6.0	0.3	0.3
5	1	4	1.25	2.1	2.4
	2	3	1.67	1.4	1.6
	3	2	2.5	0.8	0.9
	4	1	5.0	0.3	0.3

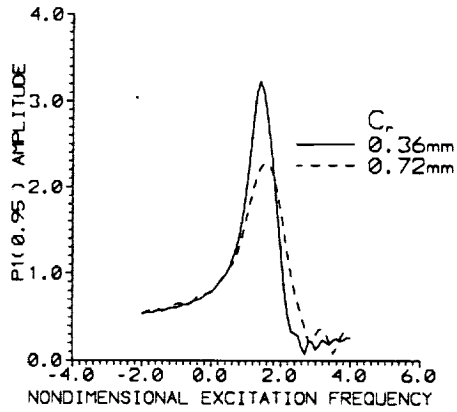

Fig. 9 $|\bar{p}_1(0.95)|$ versus f; n = 3, $u_{\theta 0}(0)$ = 0.5; C_r = 0.36 and 0.72mm

Moreover, for significant amplification within the leakage annulus, f^+ must lie near f^*, the peak-amplitude excitation frequency. Table 3 shows the variation of f^+ and f^* for various combinations of n_1 and n_2. The case of $n_1 = 8$ (eight-bladed impeller) and $n_2 = 4$ (four-bladed diffuser) yields a close proximity of $f^* = 2.1$, 2.4 to $f^+ = 2.0$; however, this is an unrealistic combination. For a practical configuration, the nondimensional frequencies $f^+ = 1.67$ and $f^* = 1.6$ are closest for $n_1 = 5$(five-bladed impeller) and $n_2 = 2$(double-discharge volute). Figure 9 illustrates $|\bar{p}_1(.95)|$ for $u_{\theta 0}(0) = 0.5$ and $n = 3$, confirming the predictions of Table 3. An amplification by a factor of 2.6 is predicted for new clearances and 3.2 for worn clearances.

Numerical Uncertainty. The numerical uncertainty issue for the results presented concerns the numerical integration of Eq. (17). The results presented were obtained with a fourth-order Runge-Kutta integrator package using 200 integration steps for the interval [0, 1]. Repeating these calculations with 400 integration steps yielded the same results to about three significant figures.

Summary and Conclusions

An analysis has been developed and results presented for the pressure oscillations in the leakage annulus between a shrouded pump impeller and its housing. These pressure oscillations are driven by a circumferential variation of the impeller discharge pressure which can precess either in the same or opposite to the direction of rotation. The circumferential variation can be modeled with a Fourier decomposition with each mode having n diametral nodes across the impeller. The peak-pressure oscillations within the impeller are predicted to occur near the exit wearing-ring seal in association with a centrifugal-acceleration-mode response of the fluid within the annulus (Childs, 1988, 1990b). The peak-amplitude-excitation frequency increases linearly with n. Using Bolleter's (1988) work which provides a dependency of n and the precessional frequency on the number of impeller (n_1) and diffuser (n_2) blades, situations are presented which can yield large amplifications (or significant attenuation) of impeller discharge variations. The occurrence and nature of the pressure oscillations are shown to depend on: (*a*) the tangential-velocity ratio of the fluid entering the seal, (*b*) the order of the Fourier coefficient, (*c*) the closeness of the precessional frequency of the rotating pressure field to the first natural frequency of the fluid annulus, and (*d*) the clearance of the wearing-ring seal.

The present results suggest an explanation for the internal melting observed on SSME HPFTP seal parts. However, given liquid hydrogen's significant compressibility, a more complete analysis, including fluid compressibility, is in order.

Bolleter, U., Wyss, A., Welte, Z., and Stürchler, R., 1987, "Measurement of Hydrodynamic Interaction Matrices of Boiler Feedpump Impellers," ASME *Journal of Vibrations, Stress, and Reliability in Design*, Vol. 109, pp. 144–151.

Bolleter, U., 1988, "Blade Passage Tones of Centrifugal Pumps," *Vibrations*, Vol. 4, No. 3.

Childs, D., 1987, "Fluid-Structure Interaction Forces at Pump-Impeller-Shroud Surfaces for Rotordynamic Calculations," *Rotating Machinery Dynamics*, Vol. II, ASME 1987, pp. 581–593.

Childs, D., 1989, "Fluid-Structure Interaction Forces at Pump-Impeller-Shroud Surfaces for Rotordynamic Calculations," ASME *Journal of Vibration, Acoustics, Stress, and Reliability in Design*, Vol. 111, July 1989, pp. 216–225.

Childs, D., 1990a, "Fluid-Structure Interaction Forces at Pump-Impeller-Shroud Surfaces for Axial Vibration Analysis," accepted for publication in ASME *Journal of Vibration and Acoustics*, May 1990.

Childs, D., 1990b, "Centrifugal-Acceleration Modes for Incompressible Fluid in the Leakage Annulus Between A Shrouded Pump Impeller and Its Housing," accepted for publication in ASME *Journal of Vibration and Acoustics*, May 1990.

Hirs, G., 1973, "A Bulk-Flow Theory for Turbulence in Lubricant Films," ASME *Journal of Lubrication Technology*, pp. 137–146.

Tyler, M. J., and Sofrin, T. A., 1962, "Axial Compressor Noise Studies," *SAE Trans.*, Vol. 70, pp. 309–332.

993)

ABSTRACT

Compressibility Effects on Rotor Forces in the Leakage Path between a Shrouded Pump Impeller and Its Housing. (August 1993)

Nhai The Cao, B.S., Texas A&M University

Chair of Advisory Committee: Dr. Dara Childs

A modified approach to Childs' previous work (1989,1992) on fluid-structure interaction forces in the leakage path between an impeller shroud and its housing is presented in this paper. Three governing equations consisting of continuity, path-momentum, and circumferential-momentum equations were developed to describe the leakage path inside a pump impeller. Radial displacement perturbations were used to solve for radial and circumferential force coefficients. In addition, impeller-discharge pressure disturbances were used to obtain pressure oscillation responses due to precessing impeller pressure wave pattern. Childs' model was modified from an incompressible model to a compressible barotropic-fluid model (the density of the working fluid is a function of the pressure and a constant temperature only). Results obtained from this model yielded interaction forces for radial and circumferential force coefficients. Radial and circumferential forces define reaction forces within the impeller leakage path.

An acoustic model for the same leakage path was also developed. The convective, Coriolis, and centrifugal acceleration terms are removed from the compressible model to obtain the acoustics model. The compressible model is compared with the incompressible model and the acoustic model. A solution due to impeller discharge pressure disturbances model was also developed for the compressible and acoustic models. The results from these modifications are used to determine what effects additional perturbation terms in the compressible model have on the acoustic model.

The results show that the additional fluid mechanics terms in the compressible

model cause resonances (peaks) in the force coefficient response curves. However, these peaks only occurred at high values of inlet circumferential velocity ratios, $u_{\theta 0}(0) > 0.7$. The peak pressure oscillation was shown to occur at the wearing ring seal. Introduction of impeller discharge disturbances with $n = 11$ diametral nodes showed that maximum peak pressure oscillations occurred at nondimensional precession frequencies ($f = \Omega/\omega$ where ω is the running speed of the pump) of $f = 6.4$ and $f = 7.8$ for this particular pump. Bolleter's results suggest that for peak pressure oscillations to occur at the wearing ring seal, the nondimensional excitation frequency should be on the order of $f = 2.182$ for $n = 11$. The resonances found in this research do not match the excitation frequencies predicted by Bolleter. At the predicted peak excitation frequencies given by Bolleter, the compressible model shows an attenuation of the pressure oscillations at the seal exit.

The compressibility of the fluid does not have a significant influence on the model at low values of nondimensional excitation frequency. At high values of nondimensional frequency, the effects of compressibility become more significant. For the acoustic analysis, the convective, Coriolis, and centrifugal acceleration terms do affect the results to a limited extent for precession excitation and to a large extent for a pressure excitation when the fluid operates at relatively high Mach numbers.

To the memory of my grandfather, Cao Van Tac.

ACKNOWLEDGEMENTS

I would like to express my thanks to Dr. Dara Childs for his countless hours of help, instruction, and support. I would also like to thank Dr. Childs for providing the opportunity for me to work on this project.

Dr. Tae Wong Ha, Dr. Zhou Yang, and Dr. Alan Duncan have provided much needed intellectual stimulation, and my thanks go out to them for their tireless effort.

Thanks also go out to Mr. Andy Ma, Mr. Gabriel Rodriguez, Mr. Patrick Hardin, and everyone else who sacrificed their sanity by providing the computer resources used in preparing this report.

Finally, Mr. Kenneth Kmiec, Mr. Steven Suh, Mr. Monte Williams, and Mr. Max Gibbs deserve special thanks for putting up with the Coke cans and all the other stuff.

TABLE OF CONTENTS

CHAPTER Page

LIST OF FIGURES

FIGURE Page

LIST OF TABLES

NOMENCLATURE

A_{1s}, A_{2s}, A_{3s}, A_{4s}, $A_{1\theta}$, $A_{2\theta}$, $A_{3\theta}$, $A_{4\theta}$	coefficients introduced in Eq. (32-33)
$b = V_i/R\omega$	nondimensional velocity ratio
C_{dc}	discharge coefficient for the exit wearing ring seal (Eq. 11)
C_i	initial (s=0) clearance (L)
C_r	exit (s=1) clearance (L)
$f = \Omega/\omega$	nondimensional frequency ratio
$h = H/C_i$	nondimensionalized clearance
H	clearance between impeller shroud and housing (L)
L	path length (L)
L_s	leakage path length (L)
M	Mach number - fluid velocity/acoustic velocity
n	difference in number of impeller blades and diffuser vanes
P	fluid static pressure (F/L^2)
$p = P/\rho V_i^2$	dimensionless pressure
$p_s(\theta,t)$	dimensionless inlet supply pressure (s=0)
$p_e(\theta,t)$	dimensionless exit pressure (seal exit)
R	radial coordinate (L)
R_i	initial radial coordinate (s=0)
$R_\alpha = 2HU_s/\nu$	Reynolds number defined in Equation (8)
$r = R/R_i$	nondimensionalized radial coordinate
S	Path coordinate (L)
$s = S/L_s$	nondimensionalized path length
$T = L_s/V_i$	representative transit time for fluid traversing the leakage path (T)
t	Time (T)
$u_s = U_s/V_i$	nondimensionalized path fluid velocity

$u_\theta = U_\theta/R_i\omega$	nondimensionalized circumferential fluid velocity
U_s, U_θ	path and circumferential velocity of fluid (L/T)
V_i	initial (s=0) path fluid velocity
ϵ	perturbation parameter
λ_r,λ_s	Friction factor definitions defined in Eq. (19)
σ_r,σ_s	Wall friction factor defined in Eq. (19)
μ	Fluid viscosity ($F\text{-}T/L^2$)
ρ	Fluid density (m/L^3)
$\tilde{\rho} = \rho/\rho_i$	nondimensionalized fluid density
$\tau = \omega t$	nondimensionalized time
τ_w	Wall shear stress (F/L^2)
τ_s, τ_r	Shear stress on stator and rotor surfaces (F/L^2)
θ	Circumferential coordinate
ω	Rotor angular velocity (T^{-1})
Ω	Shaft whirl angular velocity (T^{-1})
ξ	Inlet loss coefficient
ν	Kinematic viscosity (L^2T^{-1})

Subscripts

r, s	Rotor and stator
z, θ	Axial and circumferential directions
0, 1	Zeroth and first-order perturbations

CHAPTER I
INTRODUCTION

In the past, wear-ring seals used on the SSME HPFTP (Space Shuttle Main Engine High Pressure Fuel Turbopump) made from KEL-F plastic came back after operation revealing highly unusual characteristics. Despite being in constant contact with liquid hydrogen, post-test inspection showed that interior points in the stator element had melted and resolidified. The material used in the seal stator has poor heat conduction properties and high internal hysteretic damping. Pressure oscillations adjacent to the seal may be a source of cyclic stress producing hysteretic losses. This investigation will examine the pressure oscillations which may cause cyclic stresses in the leakage path between the impeller shroud and its housing. Possible sources of excitation causing the seal to melt and resolidify will be investigated.

For this project, an analysis will be performed for a bulk flow model of the leakage path between a pump impeller shroud and a housing along the front side of the impeller, from inlet to discharge (Fig. 1). Simply defined, a bulk flow model considers only the average of the velocity distribution across the flow field. The research will be an extension of analyses performed previously by Childs (1989, 1992) for a shrouded pump impeller and its housing.

The working fluid will be modelled as a barotropic fluid in this analysis, instead of an incompressible fluid, to account for fluid compressibility. The density and viscosity of barotropic fluids depend only on the local pressure and are independent of temperature. This assumption is reasonable for most cryogenic fluids, where viscosity is low and effects of viscous heating are negligible. The properties of the working fluid, i.e., density and viscosity, will be implemented into a new analysis by using a general 32-term, thermodynamic, equations-of-state program, MIPROPS (McCarty, 1986, modified by San Andres, 1991).

This paper is modelled after the ASME *Journal of Tribology*.

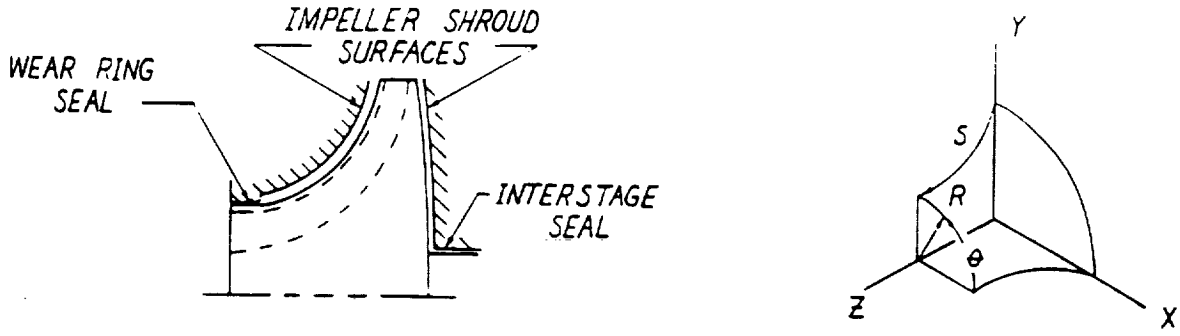

Figure 1 - Impeller stage and surface geometry

CHAPTER II
LITERATURE REVIEW

Childs (1989) performed a bulk-flow analysis for the leakage path between an impeller shroud and a pump housing. Three governing equations of motion were derived for a bulk-flow model to represent incompressible fluid flow in the leakage path of a conventional water pump impeller. Three equations, consisting of a continuity equation, a path-momentum equation, and a circumferential-momentum equation, were used to solve for rotordynamic forces due to a precessional excitation of the rotor.

Childs used a perturbation expansion in the eccentricity ratio of the governing equations of fluid motion for small motions about a centered impeller position yielding a set of zeroth and first-order governing equations. A zeroth-order solution was obtained by an iterative procedure to define the leakage, pressure, and circumferential-velocity distribution. Using a perturbed clearance function due to a radial displacement perturbation, Childs evaluated the first-order model at several inlet circumferential velocity conditions to obtain the first-order perturbed solutions. First-order perturbation results provided rotordynamic coefficients (direct and cross-coupled stiffness, damping, and mass) and lateral reaction forces for the model. Childs' predictions for the impeller of Fig. 2 are shown in Fig. 3. The predicted radial and circumferential force coefficients are shown versus the nondimensional precessional frequency for nondimensionalized inlet circumferential velocities of $u_{\theta 0}(0) = 0.5, 0.6,$ and 0.7. Nondimensional precessional frequency is the ratio of the impeller precession frequency, Ω, to its running speed, ω. The graphs showed a considerable "dip", or resonance, in the radial and circumferential force response coefficients at higher values of $u_{\theta 0}(0)$. The radial and circumferential force coefficients represent the nondimensionalized reaction forces acting on the impeller face due to impeller precession. Childs showed that the centrifugal acceleration terms in the momentum equations produced the "dip" in the results. By removing the

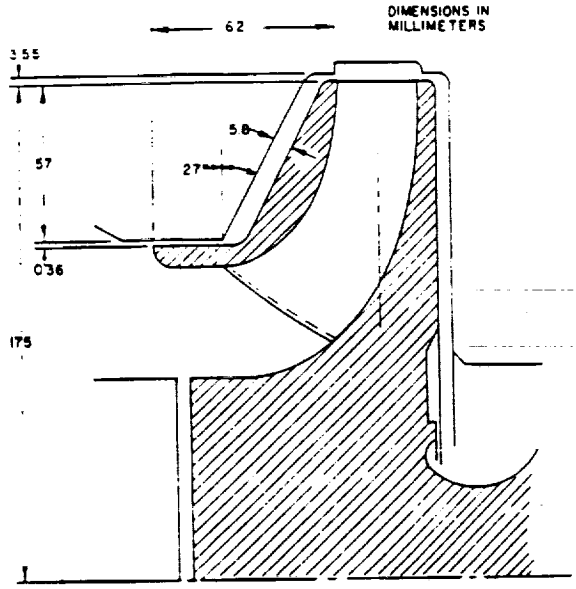

Figure 2 - Nominal configuration of conventional water impeller

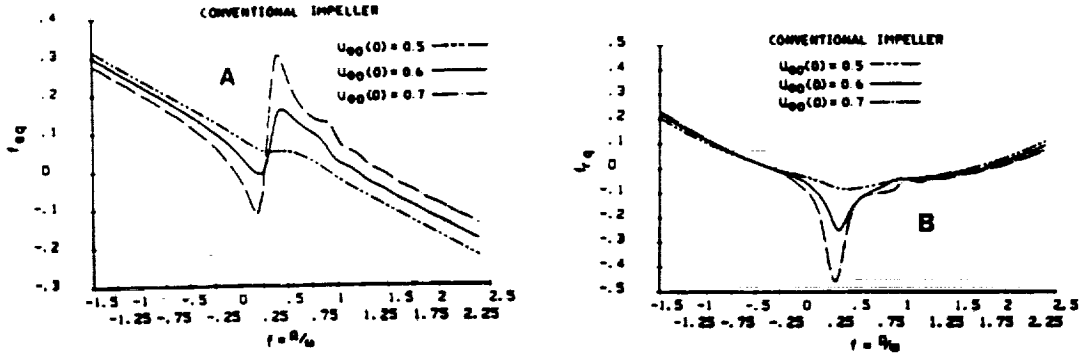

Figure 3 - Nondimensional force coefficients for the conventional impeller (a) circumferential-force coefficient, (b) radial-force coefficient

centrifugal acceleration term from the path-momentum equation, the "dips" in the plots were eliminated.

Bolleter (1988) presents a relationship between the difference (n) in the number of impeller blades (n_1) and diffuser vanes (n_2) and the precessional frequency for pressure pulsations in an impeller leakage path. Various combinations of impeller blade and diffuser vane number causing vibrations and pressure pulsations in the impeller are described. The relationship presented by Bolleter states that a pressure pattern develops with $n = |n_1 - n_2|$ diametral nodes around the impeller exit. The precession velocity of the pressure oscillation is $n\omega_1/(|n_1 - n_2|)$. For example, an impeller with $n_1 = 11$ blades and $n_2 = 6$ diffuser vanes would have amplifications of the pressure oscillations at frequencies of multiples of $11\omega/(|11 - 6|)=2.2\omega$.

Childs (1992) performed an analysis similar to (Childs, 1989) incorporating the effects of different numbers of impeller blades and diffuser vanes for the bulk flow model using excitations due to discharge-pressure oscillations instead of orbital motion. This analysis considered the harmonic response of flow within the annulus due to variations in the discharge pressure of the impeller. This analysis also compared the effect on the response of the pressure oscillation due to different numbers of pump impeller blades and diffuser vanes. Zeroth and first-order perturbation equations were also derived for this analysis. However, the first order perturbations in this analysis were excited by discharge-pressure perturbations instead of impeller precession. The impeller discharge excitation was defined as a precessing harmonic pressure oscillation with n nodes and a precessional frequency of Ω.

Results from the analysis due to perturbed flow in the leakage path caused by oscillations in the impeller discharge pressure show that the peak pressure oscillation occur near the exit ring seal. The pressure oscillations from the impeller were shown to depend on the circumferential velocity of the fluid entering the seal, the Fourier coefficient, n, and the relative closeness to the first resonant frequency of the fluid to the peak precessional frequency of the rotating pressure field. Note that n represents both the Fourier coefficient used by Childs and Bolleter's $n = |n_1 - n_2|$.

Acoustic modes are produced by the interaction of fluid inertia and compressibility. Thompson (1988) explains that the wave equation, the fundamental equation of acoustics, is obtained by assuming that the convective acceleration terms are negligible compared with the temporal acceleration terms. For ordinary acoustic analysis, Thompson states that this assumption is "highly satisfactory" for fluid flow characterized by a low Mach number, typically $M^2 \ll 0.1$. By removing the convective, Coriolis, and centrifugal acceleration terms from a modified general perturbation (compressible) version of Childs' model, a similar wave equation can be obtained. This resulting equation, in theory, can be used for an "acoustic" analysis of the flow fields.

San Andres (1991) developed a solution procedure for a model of fluid flow in turbulent hydrostatic bearings and annular seals operating with cryogenic barotropic fluids. He used a 32-term equations-of-state program provided by NBS Standard Reference Data Base for prediction of the properties of LH_2, LO_2, LN_2, and other fluids at different pressures and temperatures. The code, MIPROPS, delivers fluid properties which are used in the analysis procedure. In addition to obtaining the fluid properties from MIPROPS for use in a compressible model, San Andres also considered the properties of the working fluid as a linear function of pressure. From his results, San Andres found that for highly compressible fluids, such as liquid hydrogen, the barotropic properties model based on an equation of state gave accurate leakage and force response for bearings and seals with a large pressure differential.

CHAPTER III
OBJECTIVES

This research will introduce compressibility of the working fluid in the leakage path as an extension to the analyses performed by Childs (1989, 1992). The results will provide information concerning the relationship between an incompressible, a compressible, and an acoustic model with liquid hydrogen as the working fluid. The results will also provide information regarding the cause of the unusual behavior exhibited by the KEL-F plastic rotor element and verify the validity of Thompson's assessment concerning the effects of fluid mechanics and acoustics. This research project will also analyze the effects of the centrifugal acceleration modes and acoustic modes of a barotropic fluid in the leakage path between a shrouded pump impeller and its housing.

The results obtained from a compressible-flow model will be compared with the results of an incompressible model. The compressible-flow model will also be reduced to an acoustics model, the results of which will be compared to the compressible-flow model. This comparison will be performed for two different perturbation excitations: (a) a precessional excitation involving an orbital motion of the rotor, and (b) a pressure oscillation excitation, involving perturbation of the discharge or inlet pressure of the leakage path. The geometric and operating characteristics of the first stage impeller of the SSME HPFTP will provide the parameters used for the governing equations.

A bulk-flow model will be developed and used to simulate the leakage path inside the first impeller stage of the Space Shuttle Main Engine Turbopump. Results from the computation should indicate if any interaction exists between acoustic and centrifugal acceleration modes, and the influence of fluid mechanics terms (convective, Coriolis, or centrifugal acceleration terms) on acoustic modes.

CHAPTER IV
GEOMETRIC AND OPERATING CHARACTERISTICS

Figure 4 shows the first-stage impeller of the Space Shuttle Main Engine Turbopump. The impeller measures 0.3048 m in diameter at the exit (leakage path inlet) and 0.1905 m in diameter at the seal inlet (leakage path exit). The impeller is also characterized by 24 impeller blades and 13 diffuser vanes. At full power levels, this stage operates at 34,000 rpm, with an inlet pressure at the entrance to the leakage path of 13.79 MPa and a discharge pressure of 1.72 MPa at the exit of the wearing ring seal. Operating at a pump speed of 34,000 rpm, the resultant velocity vector of the liquid hydrogen inside the leakage path is calculated to be about 0.4 times the acoustic velocity of liquid hydrogen.

The wearing ring seal contains four steps, measuring 0.1915, 0.185, 0.1786, and 0.172 m in diameter, which accommodate four teeth at the end of the impeller blade. The radial clearances between the seal and the rotor teeth are estimated to be 0.229 mm (0.009 in), accounting for radial expansion of the rotor during operation.

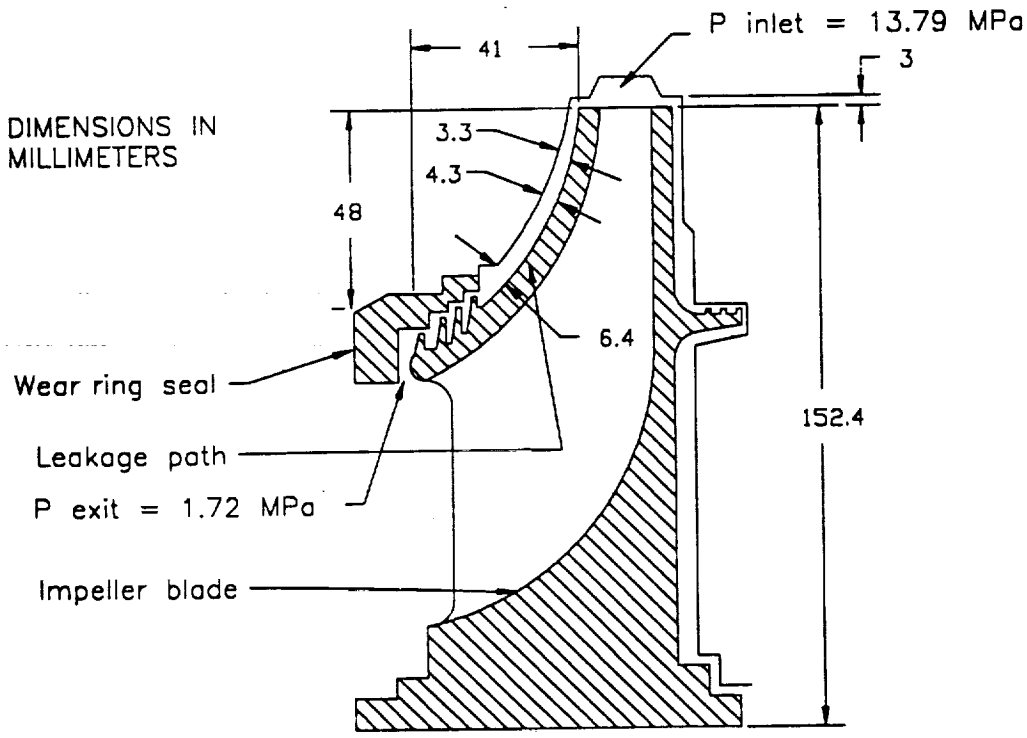

Figure 4 - SSME HPFTP first impeller stage

CHAPTER V
BULK FLOW MATHEMATICAL MODEL

Childs' governing equations will be modified for this project to reflect a bulk flow model operating with a barotropic fluid. As in Childs' analysis, these equations will be nondimensionalized and perturbed to yield zeroth and first-order governing equations.

5.1 General Governing Equations

Using the approach taken by Childs (1989), the governing equations are:

- *Continuity Equation*

$$\frac{\partial \rho H}{\partial t} + \frac{\partial}{\partial S}(\rho U_s H) + \frac{1}{R}\frac{\partial}{\partial \Theta}(\rho U_\theta H) + \frac{H}{R}\frac{\partial R}{\partial S}\rho U_s = 0 \qquad (1)$$

- *Path-Momentum Equation*

$$-H\frac{\partial P}{\partial S} = -\rho H\frac{U_\theta^2}{R}\frac{dR}{dS} + \tau_{ss} + \tau_{sr} + \rho H\left(\frac{\partial U_s}{\partial t} + \frac{\partial U_s}{\partial \Theta}\frac{U_\theta}{R} + \frac{\partial U_s}{\partial S}U_s\right) \qquad (2)$$

- *Circumferential-Momentum Equation*

$$-\frac{H}{R}\frac{\partial P}{\partial \Theta} = \tau_{\theta s} + \tau_{\theta r} + \rho H\left(\frac{\partial U_\theta}{\partial t} + \frac{\partial U_\theta}{\partial \Theta}\frac{U_\theta}{R} + \frac{\partial U_\theta}{\partial S}U_s + \frac{U_\theta U_s}{R}\frac{\partial R}{\partial S}\right) \qquad (3)$$

An additional governing equation is obtained by using MIPROPS to obtain the properties of liquid hydrogen.

• *Equations of State*

$$\rho = \rho(P, \bar{T}^{\circ})$$
$$\mu = \mu(P, \bar{T}^{\circ}) \tag{4}$$

With the exception of the addition of ρ to the continuity equation, Eqs. (1-3) are identical to Childs' (1989). The path and circumferential-momentum equations do not change from Childs' model because the density (ρ) drops out of the momentum equations when the continuity equation is used to simplify them.

The equations of state in Eq. (4) define the density and viscosity for the bulk-flow model. The variation in density of the fluid in the model will be implemented by assuming that the working fluid is barotropic. Here, the variation in density of the working fluid will be modelled as a function of pressure and a constant temperature only. In this investigation, the MIPROPS code calculates the value of density and viscosity at a constant temperature of 23.37 K with varying input pressures, and returns values of density and viscosity to the main program. The variation of viscosity with respect to pressure were very slight; therefore, viscosity was kept constant.

$H(S, \theta, t)$ in the governing equations defines the clearance between the impeller and the housing. Nondimensionalization of this variable is given in the nomenclature and also later in this text.

Hir's (1973) definitions were used to define the shear stress components of the rotor and stator surfaces. The equations shown below define the shear stress acting on the impeller and its housing. The first subscript in the equations denotes the direction of fluid flow (path and circumferential), and the second subscript refers to the surface (stator and rotor), respectively.

$$\tau_{ss} = \frac{nS}{2}\rho U_s^2 R_a^{ms}\left[1 + (U_\theta/U_s)^2\right]^{\frac{ms+1}{2}} \tag{5}$$

$$\tau_{sr} = \frac{nr}{2}\rho U_s^2 R_\alpha^{mr}\left\{1+\left[(U_\theta - R\omega)/U_s\right]^2\right\}^{\frac{mr+1}{2}} \tag{6}$$

$$\tau_{\theta s} = \frac{ns}{2}\rho U_\theta U_s R_\alpha^{ms}\left[1+(U_\theta/U_s)^2\right]^{\frac{ms+1}{2}} \tag{7}$$

$$\tau_{\theta r} = \frac{nr}{2}\rho U_s(U_\theta - R\omega)R_\alpha^{mr}\left\{1+\left[(U_\theta - R\omega)/U_s\right]^2\right\}^{\frac{mr+1}{2}} \tag{8}$$

Reynolds' number used in these equations is represented by,

$$R_\alpha = 2HU_s/\nu \tag{9}$$

Boundary Conditions

The pressure drop of the inlet to the leakage path provides the inlet boundary condition (s=0) given by the relationship,

$$P_s - P_0(0,\theta,t) = \rho(1+\xi)U_{s0}^2(0,\theta,t)/2 \tag{10}$$

The exit wearing-ring seal defines the following exit boundary condition,

$$P(L_s,\theta,t) - P_e = \frac{\rho}{2}C_{de}U_s^2(L_s,\theta,t) \tag{11}$$

These boundary conditions apply directly for precession excitations.

For the analysis which examines the changes in (u_s, u_θ, p) due to changes in the impeller's discharge P_e or inlet pressure P_s, the following boundary conditions are

stated for the inlet and exit, respectively,

$$P_s(\theta,t) - P_0(0,\theta,t) = \rho(1+\xi)U_{s0}^2(0,\theta,t)/2 \tag{12}$$

$$P(L_s,\theta,t) - P_e(\theta,t) = \frac{\rho}{2} C_{de} U_s^2(L_s,\theta,t) \tag{13}$$

Eqs. (12-13) differ from Eqs. (10-11) because P_e and P_s are now also functions of time.

5.2 General Perturbed Equations - Nondimensionalization and Perturbation Analysis

Introducing the following variables into Eqs. (1-8),

$$\begin{aligned} &u_s = U_s/V_i, \quad u_\theta = U_\theta/R_i\omega, \quad p = P/\rho V_i^2, \quad \tilde{\rho} = \rho/\rho_i \\ &h = H/C_i, \quad s = S/L_s, \quad r = R/R_i \\ &\tau = \omega t, \quad b = V_i/R_i\omega, \quad T = L_s/V_i \end{aligned} \tag{14}$$

yields nondimensional governing equations.

The perturbation variables used to obtain zeroth and first-order equations are defined by,

$$\begin{aligned} u_s = u_{s0} + \epsilon u_{s1}, \quad h = h_0 + \epsilon h_1, \quad \tilde{\rho} = \tilde{\rho}_0 + \epsilon\tilde{\rho}_1 \\ u_\theta = u_{\theta 0} + \epsilon u_{\theta 1}, \quad p = p_0 + \epsilon p_1 \end{aligned} \tag{15}$$

where ϵ is the perturbation coefficient to be defined separately below for precession and discharge-pressure excitation.

5.2.1 Zeroth Order Solution

The zeroth-order equations are the same for the precession and exit-pressure excitations.

5.2.1.1 Zeroth-Order Equations

The path and circumferential velocity distribution and the leakage rate for a centered impeller position are defined by the following zeroth-order governing equations.

- *Continuity Equation*

$$rh_0 u_{s0} \tilde{\rho}_0 = 1 \tag{16}$$

- *Path-Momentum Equation*

$$-\frac{1}{\tilde{\rho}_0}\frac{dp_0}{ds} = u_{s0}\frac{du_{s0}}{ds} - \frac{1}{r}\frac{dr}{ds}\left(\frac{u_{\theta 0}}{b}\right)^2 + \frac{(\sigma_s+\sigma_r)}{2}u_{s0}^2 \tag{17}$$

- *Circumferential-Momentum Equation*

$$2\frac{du_{\theta 0}}{ds} + 2\frac{u_{\theta 0}}{r}\frac{dr}{ds} + \left[\sigma_r(u_{\theta 0} - r) + \sigma_s u_{\theta 0}\right] = 0 \tag{18}$$

where

$$\sigma_s = (L_s/H_0)\lambda_s,\ \sigma_r = (L_s/H_0)\lambda_r$$

$$\lambda_s = nsR_{\alpha 0}^{ms}\left[1 + (u_{\theta 0}/bu_{s0})^2\right]^{\frac{ms+1}{2}} \tag{19}$$

$$\lambda_r = nsR_{\alpha 0}^{mr}\left\{1 + \left[(u_{\theta_0} - r)/bu_{s0}\right]^2\right\}^{\frac{mr+1}{2}}$$

- *Equation of State*

$$\tilde{\rho} = \tilde{\rho}(p, \bar{T}^\circ) \tag{20}$$

Eq. (19) represents friction factor definitions for the stator and rotor surfaces, respectively, introduced in Eqs. (5-8).

5.2.1.2 Zeroth-Order Solution

The zeroth-order continuity Eq. (16) can also be expressed as,

$$\frac{du_{s0}}{ds} = -u_{s0}\left[\frac{1}{h_0}\frac{dh_0}{ds} + \frac{1}{\tilde{\rho}_0}\frac{d\tilde{\rho}_0}{ds} + \frac{1}{r}\frac{dr}{ds}\right] \tag{21}$$

This equation can be substituted into Eq. (17) to obtain

$$-\frac{1}{\tilde{\rho}_0}\frac{dp_0}{ds} = -u_{s0}^2\left[\frac{1}{h_0}\frac{dh_0}{ds} + \frac{1}{\tilde{\rho}_0}\frac{d\tilde{\rho}_0}{ds} + \frac{1}{r}\frac{dr}{ds}\right] - \frac{1}{r}\frac{dr}{ds}\left(\frac{u_{\theta 0}}{b}\right)^2 + \frac{(\sigma_s+\sigma_r)}{2}u_{s0}^2 \tag{22}$$

The governing zeroth-order equations now reduce to two governing equations, consisting of Eq. (18) and Eq. (22). Eq. (20) defines ρ solely as a function of p and provides the density used in Eq. (18) and Eq. (22).

Boundary Conditions

The inlet boundary condition for the zeroth-order pressure relationship can be expressed from Eq. (10) as,

$$p_0(0) = \frac{P_s}{\rho_i V_i^2} - (1+\xi)\frac{u_{s0}^2(0)}{2} \tag{23}$$

The zeroth-order solutions are obtained by solving Equations (18) and (22) iteratively. An initial (s=0) fluid velocity V_i is estimated which then defines $u_{s0}(s)$. A specified $u_{\theta 0}(0)$ and the calculated p_0 from Eq. (23) are used to numerically integrate the zeroth-order equations (18) and (22) from the path entrance (s=0), to the path exit (s=1). The procedure is continued with revised values of V_i until convergence is obtained between the prescribed and the calculated exit pressure.

5.2.1.3 Zeroth-Order Results

The zeroth-order results provide the mass flow rate through the leakage path.

The discharge coefficient C_{de} used in this analysis was obtained by using the leakage rate through the wearing ring seal. The leakage through the wearing ring seal of the SSME HPFTP was calculated using a seal leakage code developed by Morrison et al. (1983), and this value was used to calculate the discharge coefficient at specific impeller operating conditions. The seal leakage code uses the geometry of the seal and the operating conditions, i.e., inlet and exit pressures, viscosity, density, etc. to calculate the leakage rate through the seal. Note that this seal leakage code treats the working fluid as incompressible.

The seal leakage code yielded several mass flow rates for the prescribed geometry and operating conditions, depending upon the pressure drop across the impeller and the wearing ring seal. Several discharge coefficients were tested in the model to match the flow rate through the impeller leakage path and the flow rate through the seal. Once the two flow rates converged, the resulting C_{de} was used in the model as an exit restriction boundary condition. The mass flow rate through the seal was found to be 1.6373 kg/s, with the resulting C_{de} being 7039.6, and inlet and exit pressure of the seal being 8.101 MPa and 1.72 MPa, respectively. This pressure drop across the seal represents about one third of the total pressure drop across the entire impeller leakage path.

Zeroth-order pressure solutions for the incompressible and compressible models are shown in Figure 5. The nondimensional path velocity along the leakage path is given in Figure 6, and the zeroth-order circumferential path velocity is shown in Figure 7. For the incompressible model, a mean value for the density of liquid hydrogen inside the impeller leakage path was used to obtain the results shown.

The results of the compressible model vary only slightly from the incompressible model for the zeroth-order solution. The pressure distribution across the leakage path shows the same trend and approximately the same magnitude of pressure drop, but not exactly the same inlet and exit pressure values. The C_{de} found earlier provides the exit restriction for the seal and therefore is used for both models. Because the incompressible model uses an average density along the leakage path, the inlet and exit densities for the two models will be slightly different. This accounts for

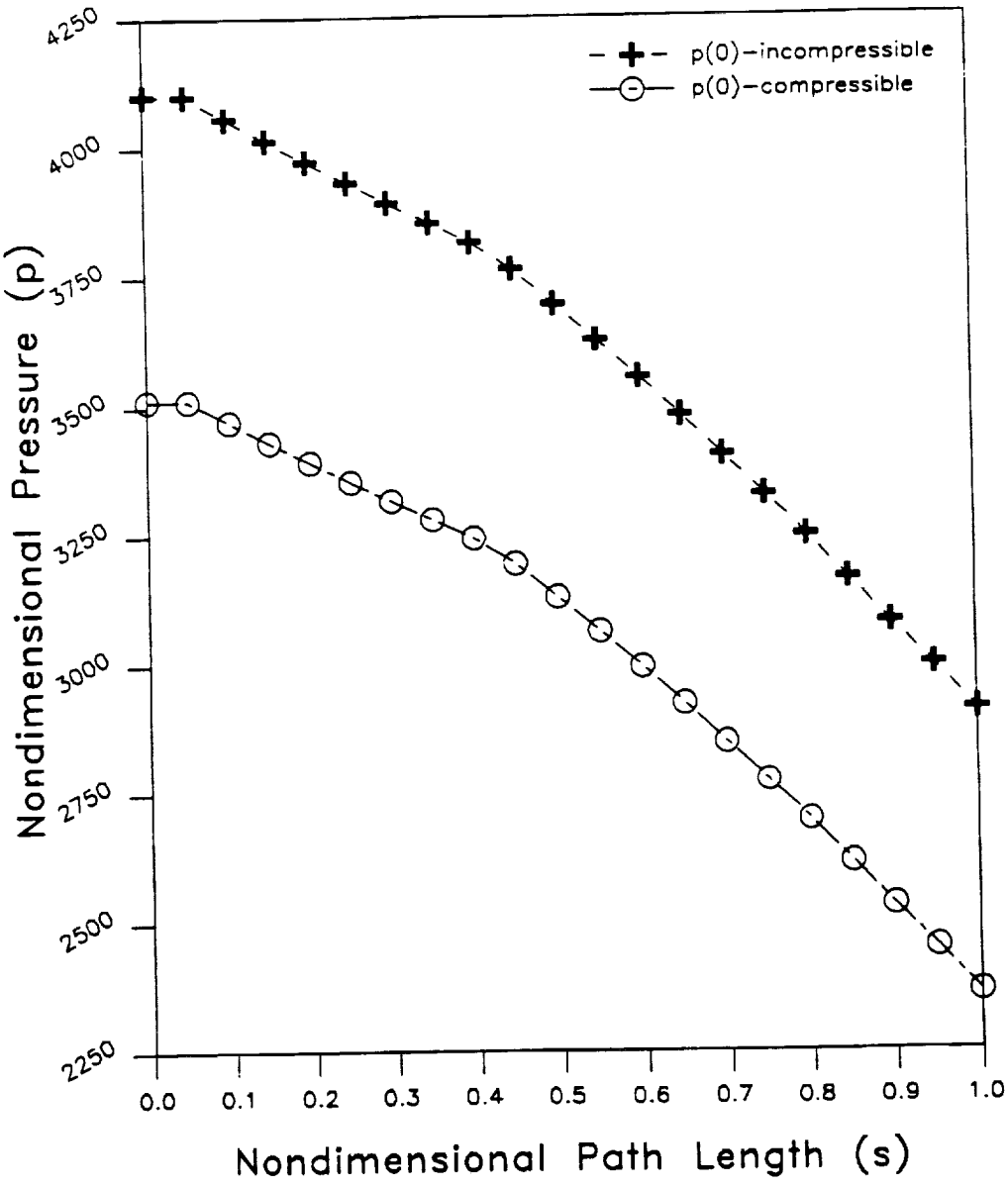

Figure 5 - Zeroth-order pressure p distribution along leakage path for compressible and incompressible models for $u_{s0}(0) = 0.7$

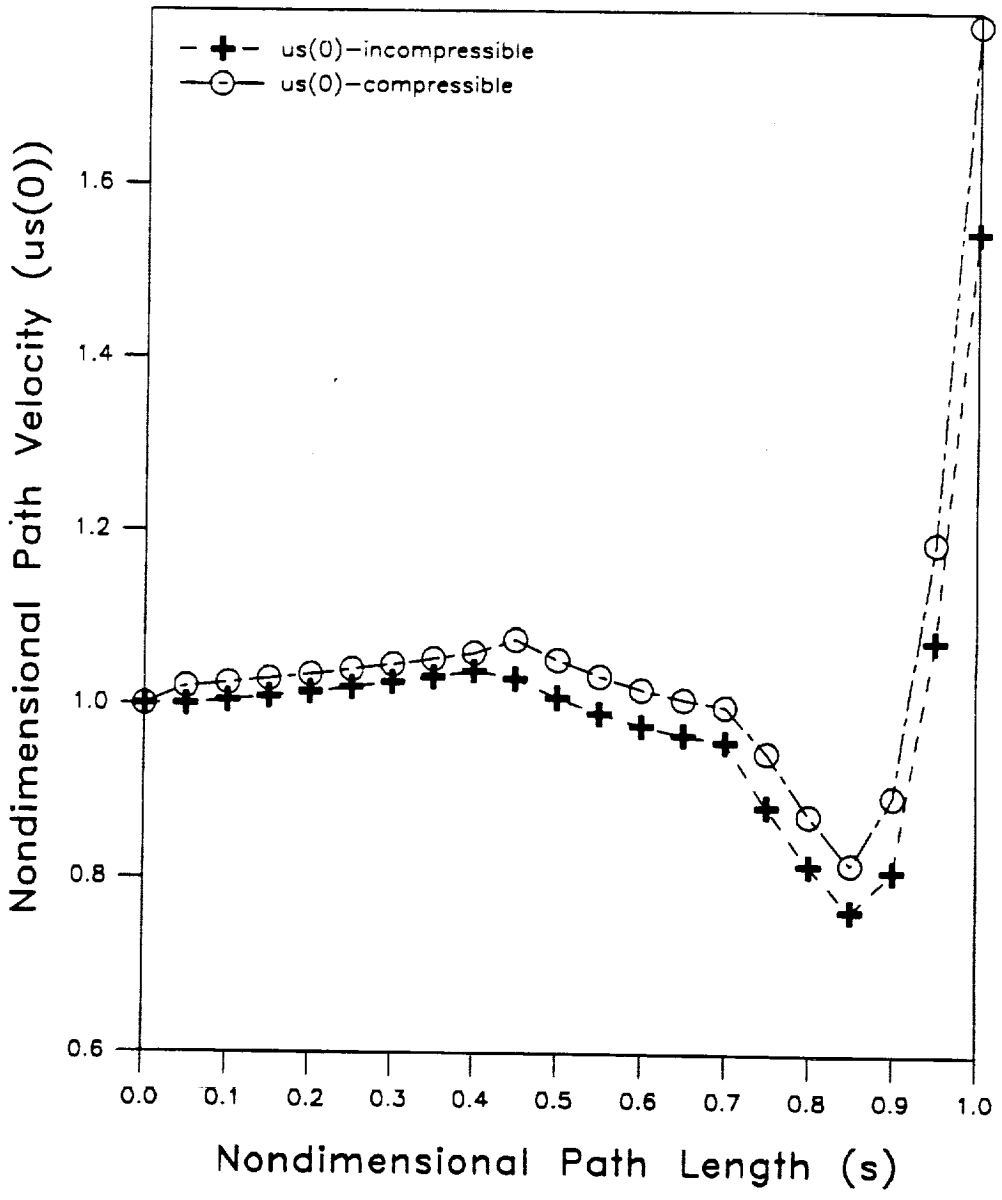

Figure 6 - Zeroth-order path velocity (u_{s0}) distribution along leakage path for compressible and incompressible models for $u_{\theta 0}(0) = 0.7$

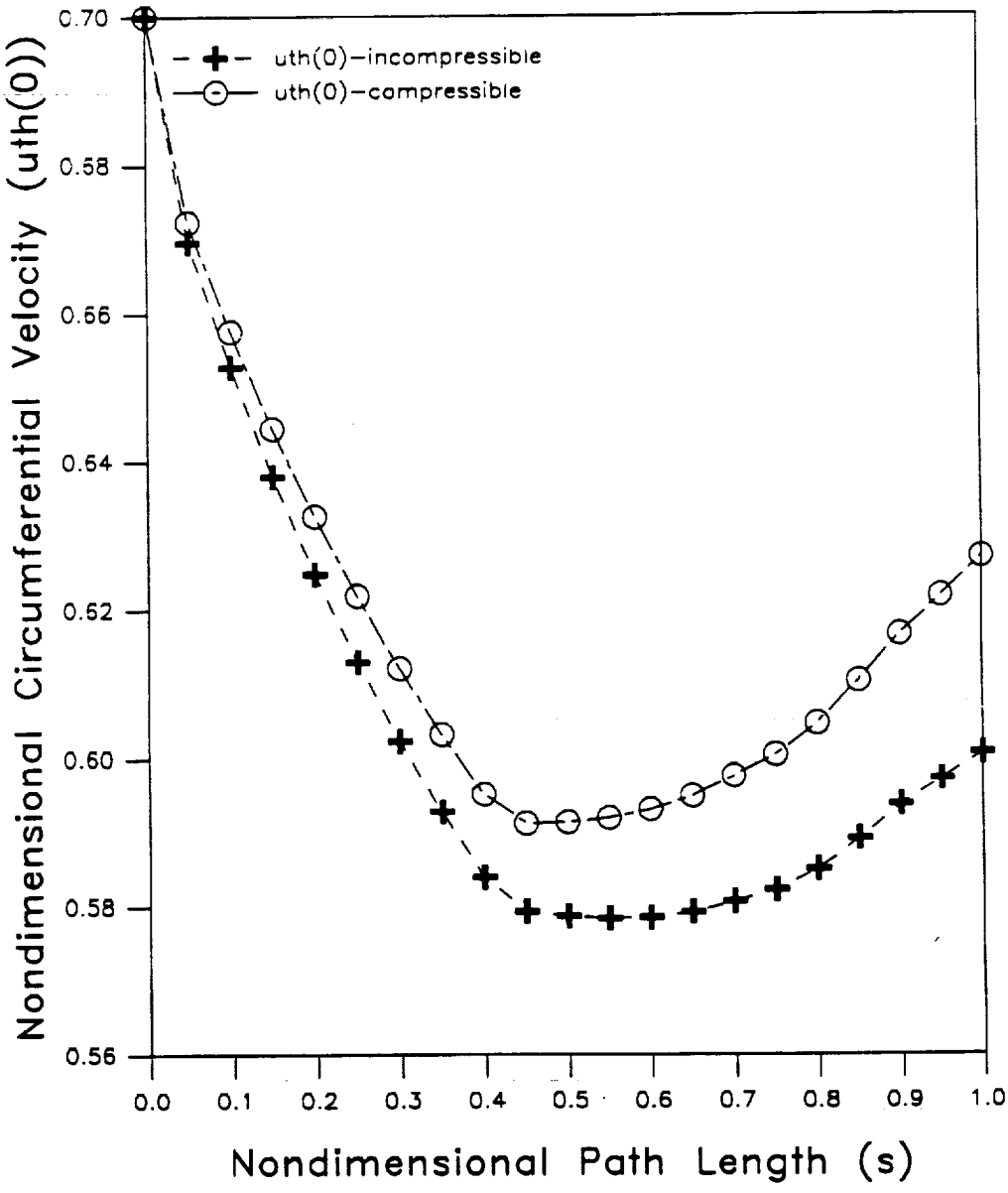

Figure 7 - Zeroth-order circumferential velocity distribution along leakage path for compressible and incompressible models for $u_{\theta 0}(0) = 0.7$

the difference in the dimensionless pressure magnitudes shown in Figure 5. The dimensional pressures at the inlet are almost exactly the same value, confirming the inlet boundary condition. As shown in Figure 6 and Figure 7, the zeroth-order path velocity and the zeroth-order circumferential velocity are not affected significantly by compressibility.

5.2.2 First-Order Equations

First-order governing equations define the path and circumferential velocity and pressure distribution along the leakage path due to perturbed clearance function or perturbed discharge-pressure.

First-order perturbation equations obtained by the perturbation expansion of Eq. (14) are

- *Continuity Equation*

$$\tilde{\rho}_0\frac{\partial h_1}{\partial \tau}+h_0\frac{\partial \tilde{\rho}_1}{\partial \tau}+\frac{1}{r}\left[u_{\theta 0}h_0\frac{\partial \tilde{\rho}_1}{\partial \theta}+h_0\tilde{\rho}_0\frac{\partial u_{\theta 1}}{\partial \theta}+u_{\theta 0}\tilde{\rho}_0\frac{\partial h_1}{\partial \theta}\right]$$
$$+\frac{1}{T\omega}\left[\frac{\partial(\tilde{\rho}_0u_{s0}h_1)}{\partial s}+\frac{\partial(\tilde{\rho}_0u_{s1}h_0)}{\partial s}+\frac{\partial(\tilde{\rho}_1u_{s0}h_0)}{\partial s}\right]+\frac{1}{T\omega}\frac{dr}{r\,ds}(u_{s0}\tilde{\rho}_0h_1+u_{s1}\tilde{\rho}_0h_0+u_{s0}\tilde{\rho}_1h_0)=0 \tag{24}$$

- *Path-Momentum Equation*

$$\frac{1}{\partial\tilde{\rho}_0}\frac{\partial p_1}{\partial s}+u_{\theta 1}A_{2s}+u_{s1}A_{3s}+\tilde{\rho}_1A_{4s}+\left[T\omega\frac{\partial u_{s1}}{\partial \tau}+T\omega\frac{u_{\theta 0}\partial u_{s1}}{r\partial\theta}+u_{s0}\frac{\partial u_{s1}}{\partial s}\right]=h_1A_{1s} \tag{25}$$

- *Circumferential-Momentum Equation*

$$\frac{b}{r}\frac{L_s}{R_i}\frac{\partial p_1}{\tilde{\rho}_o\partial\theta}+u_{\theta 1}A_{2\theta}+u_{s1}A_{3\theta}+\tilde{\rho}_1A_{4\theta}+\left[T\omega\frac{\partial u_{\theta 1}}{\partial \tau}+T\omega\frac{u_{\theta 0}}{r}\frac{\partial u_{\theta 1}}{\partial\theta}+u_{s0}\frac{\partial u_{\theta 1}}{\partial s}\right]=h_1A_{1\theta} \tag{26}$$

- *Equation of State*

$$\frac{\partial \tilde{\rho}_1}{\partial s} = \frac{d\tilde{\rho}_1}{dp}\frac{\partial p_1}{\partial s}, \quad \frac{\partial \tilde{\rho}_1}{\partial \tau} = \frac{d\tilde{\rho}_1}{dp}\frac{\partial p_1}{\partial \tau}, \quad \frac{\partial \tilde{\rho}_1}{\partial \theta} = \frac{d\tilde{\rho}_1}{dp}\frac{\partial p_1}{\partial \theta} \tag{27}$$

With the exceptions of A_{4s} and $A_{4\theta}$, which are defined in the appendix, the parameters A_{1s}, A_{2s}, etc., in these equations can be found in Childs (1989).

The dependency of $\tilde{\rho}$ with respect to s, τ, and θ in Eq. (24-26) are eliminated from the governing equations by applying the definitions of Eq. (27). The relationship between $\tilde{\rho}$ and p in Eq. (27) was obtained from the results produced by MIPROPS.

CHAPTER VI
FIRST ORDER EQUATIONS AND SOLUTIONS FOR GENERAL PERTURBED COMPRESSIBLE MODELS

This chapter provides the first order equations and solutions for precession excitation and pressure excitation cases for the general perturbation (compressible) models. Results for both excitation cases are presented using an inlet tangential velocity of $u_{\theta 0}(0) = 0.7$. The radial and circumferential-force coefficient response curves represent the nondimensional reaction force acting on the impeller face in the respective directions versus nondimensional frequency ratio, f.

For the first-order solution analysis, a separation of variable approach was used to obtain complex ordinary differential equations. The resulting coupled equations were integrated to obtain the nondimensional radial and circumferential force response coefficients. The calculated results from the first-order precession excitation and the pressure excitation of the general perturbed bulk flow model provide predictions which can be used to qualify and quantify the effects of fluid compressibility in the model.

6.1 Precession Excitation: General-Perturbation Model

The precession excitation of the general perturbed model uses the perturbed clearance function,

$$\epsilon h_1 = h_{1c}(s,\tau)\cos\theta + h_{1s}(s,\tau)\sin\theta \tag{28}$$

as the excitation.

The theta dependency of Eqs. (24-26) can be eliminated by substituting the following solution format

$$\begin{aligned} u_{s1} &= u_{s1c}\cos\theta + u_{s1s}\sin\theta & \qquad u_{\theta 1} &= u_{\theta 1c}\cos\theta + u_{\theta 1s}\sin\theta \\ p_1 &= p_{1c}\cos\theta + p_{1s}\sin\theta & \qquad \tilde{\rho}_1 &= \tilde{\rho}_{1c}\cos\theta + \tilde{\rho}_{1s}\sin\theta \end{aligned} \tag{29}$$

into Eqs. (24-26), which yields six real equations.

Three complex equations in the independent variables s and τ can be obtained by introducing the complex variables

$$\underline{u}_{s1} = u_{s1c} + ju_{s1s}, \quad \underline{u}_{\theta 1} = u_{\theta 1c} + ju_{\theta 1s}, \quad \underline{\tilde{\rho}}_1 = \tilde{\rho}_{1c} + j\tilde{\rho}_{1s}$$
$$\underline{p}_1 = p_{1c} + jp_{1s}, \quad \underline{h}_1 = h_{1c} + jh_{1s} \tag{30}$$

These complex equations in the independent variables s and τ are

$$\frac{\partial \underline{u}_{s1}}{\partial s} - \frac{j\omega T}{r}\underline{u}_{\theta 1} + \underline{u}_{s1}\left[\frac{1}{h_0}\frac{\partial h_0}{\partial s} + \frac{1}{\tilde{\rho}_0}\frac{\partial \tilde{\rho}_0}{\partial s} + \frac{1}{r}\frac{\partial r}{\partial s}\right] - \underline{\tilde{\rho}}_1\left[\frac{u_{s0}}{\tilde{\rho}_0{}^2}\frac{\partial \tilde{\rho}_0}{\partial s} + j\frac{\omega T}{\tilde{\rho}_0 r}u_{\theta 0}\right]$$
$$+ \frac{\omega T}{\tilde{\rho}_0}\frac{d\tilde{\rho}_1}{dp_1}\frac{\partial p_1}{\partial \tau} + \frac{u_{s0}}{\tilde{\rho}_0}\frac{\partial \tilde{\rho}_1}{\partial s} = \underline{h}_1\left[\frac{u_{s0}}{h_0{}^2}\frac{\partial h_0}{\partial s} + j\frac{\omega T}{h_0 r}u_{\theta 0}\right] - \frac{\omega T}{h_0}\frac{\partial \underline{h}_1}{\partial \tau} - \frac{u_{s0}}{h_0}\frac{\partial \underline{h}_1}{\partial s} \tag{31}$$

$$\frac{1}{\tilde{\rho}_0}\frac{\partial \underline{p}_1}{\partial s} + \underline{u}_{\theta 1}A_{2s} + \underline{u}_{s1}A_{3s} + \underline{\tilde{\rho}}_1 A_{4s} + \left[T\omega\frac{\partial \underline{u}_{s1}}{\partial \tau} - jT\omega\frac{u_{\theta 0}}{r}\underline{u}_{s1} + u_{s0}\frac{\partial \underline{u}_{s1}}{\partial s}\right] = \underline{h}_1 A_{1s} \tag{32}$$

$$-\frac{b}{r}\frac{L_s}{R_i}\frac{\underline{p}_1}{\tilde{\rho}_0} + \underline{u}_{\theta 1}A_{2\theta} + \underline{u}_{s1}A_{3\theta} + \underline{\tilde{\rho}}_1 A_{4\theta} + \left[T\omega\frac{\partial \underline{u}_{\theta 1}}{\partial \tau} - jT\omega\frac{u_{\theta 0}}{r}\underline{u}_{\theta 1} + u_{s0}\frac{\partial \underline{u}_{\theta 1}}{\partial s}\right] = h_1 A_{1\theta} \tag{33}$$

Since the equation of state is a function of pressure and a constant temperature only, it can be modified as shown in Eq. (27) and used to remove the dependency of $\tilde{\rho}_1$ from s in Eq. (31). Further simplification of Eqs.(33-35) can be made by using the following definitions provided by Childs (1989)

$$\epsilon \underline{h}_1 = -q\left(\frac{L}{L_s}\right)\frac{dz}{ds} \tag{34}$$

$$\epsilon \frac{\partial \underline{h}_1}{\partial s} = -q\left(\frac{L}{L_s}\right)\frac{d^2 z}{ds^2} \tag{35}$$

where

$$q = x + jy \tag{36}$$

Eq. (36) represents the physical motion of the rotor in the x and y directions, shown in Figure 1.

Assuming a harmonic seal motion of the form

$$q = q_0 e^{jf\tau}, \quad f = \Omega/\omega \tag{37}$$

the corresponding harmonic solutions can be stated,

$$u_{s1} = \bar{u}_{s1} e^{jf\tau}, \quad u_{\theta 1} = \bar{u}_{\theta 1} e^{jf\tau}, \quad p_1 = \bar{p}_1 e^{jf\tau} \tag{38}$$

which yields the following three complex ordinary differential equations of motion,

$$\frac{d}{ds}\begin{Bmatrix} \bar{u}_{s1} \\ \bar{u}_{\theta 1} \\ \bar{p}_1 \end{Bmatrix} + [A]\begin{Bmatrix} \bar{u}_{s1} \\ \bar{u}_{\theta 1} \\ \bar{p}_1 \end{Bmatrix} = \left(\frac{q_0}{\epsilon}\right)\begin{Bmatrix} g_1 \\ g_2 \\ g_3 \end{Bmatrix} \tag{39}$$

where

$$[A] = \begin{bmatrix} A_{11} & -\dfrac{j\omega T}{r} - A_{12} & -\dfrac{d\tilde{\rho}_0}{ds}\left(\dfrac{u_{s0}}{\tilde{\rho}_0^2}\dfrac{d\tilde{\rho}_0}{ds} + \dfrac{j\omega T u_{\theta 0}}{\tilde{\rho}_0 r}\right) + j\omega T\dfrac{d\tilde{\rho}_0}{ds} + A_{13} \\ \dfrac{A_{3s}}{u_{s0}} & \dfrac{A_{2\theta}}{u_{s0}} + \dfrac{j\Gamma T}{u_{s0}} & A_{4\theta}\dfrac{d\tilde{\rho}_0}{ds} - j\dfrac{bL_s}{r u_{s0}\tilde{\rho}_0 R_i} \\ A_{31} & A_{32} & \dfrac{A_{4s}}{\tilde{\rho}_0} - \dfrac{A_{33}}{\tilde{\rho}_0}\dfrac{d\tilde{\rho}_0}{ds} \end{bmatrix} \tag{40}$$

$$\begin{Bmatrix} g_1 \\ g_2 \\ g_3 \end{Bmatrix} = \left(\frac{L}{L_s}\right) \begin{Bmatrix} \frac{u_{s0}}{\tilde{\rho}_0}\frac{d\tilde{\rho}_0}{dp_0}G_q + F_2 + j\frac{\Gamma T}{h_0}\frac{dz}{ds} \\ -\frac{dz}{ds}\frac{A_{1\theta}}{u_{s0}} \\ G_q \end{Bmatrix} \tag{41}$$

Elements used in Eqs. (40-41) can be found in Appendix A.

6.1.1 Boundary Conditions

Nondimensional first-order boundary conditions for the precession excitation can be stated from equations (10) and (11) as

$$\frac{\bar{p}_1(0)}{\left(1+\frac{(1+\xi)}{2}\frac{d\tilde{\rho}}{dp}|_0\right)} = -(1+\xi)\bar{u}_{s1}(0) \tag{42}$$

$$\frac{\bar{p}_1(1)}{\left(1+\frac{(1+\xi)}{2}\frac{d\tilde{\rho}}{dp}|_1\right)} = C_{de}u_{s0}(1)\bar{u}_{s1}(1) \tag{43}$$

Additionally, the perturbation entrance circumferential velocity can be stated as zero,

$$\bar{u}_{\theta 1}(0) = 0 \tag{44}$$

The solution to this set of equations is obtained by applying the procedure presented by Childs (1989). The solution procedure used to determine the reaction forces and moments are also given by Childs (1989).

6.1.2 First-Order Results

Radial and circumferential force response coefficients for general compressible and incompressible precession excitation models operating with an inlet circumferential velocity of $u_{\theta 0}(0) = 0.7$ are shown in Figure 8 and Figure 9. The results

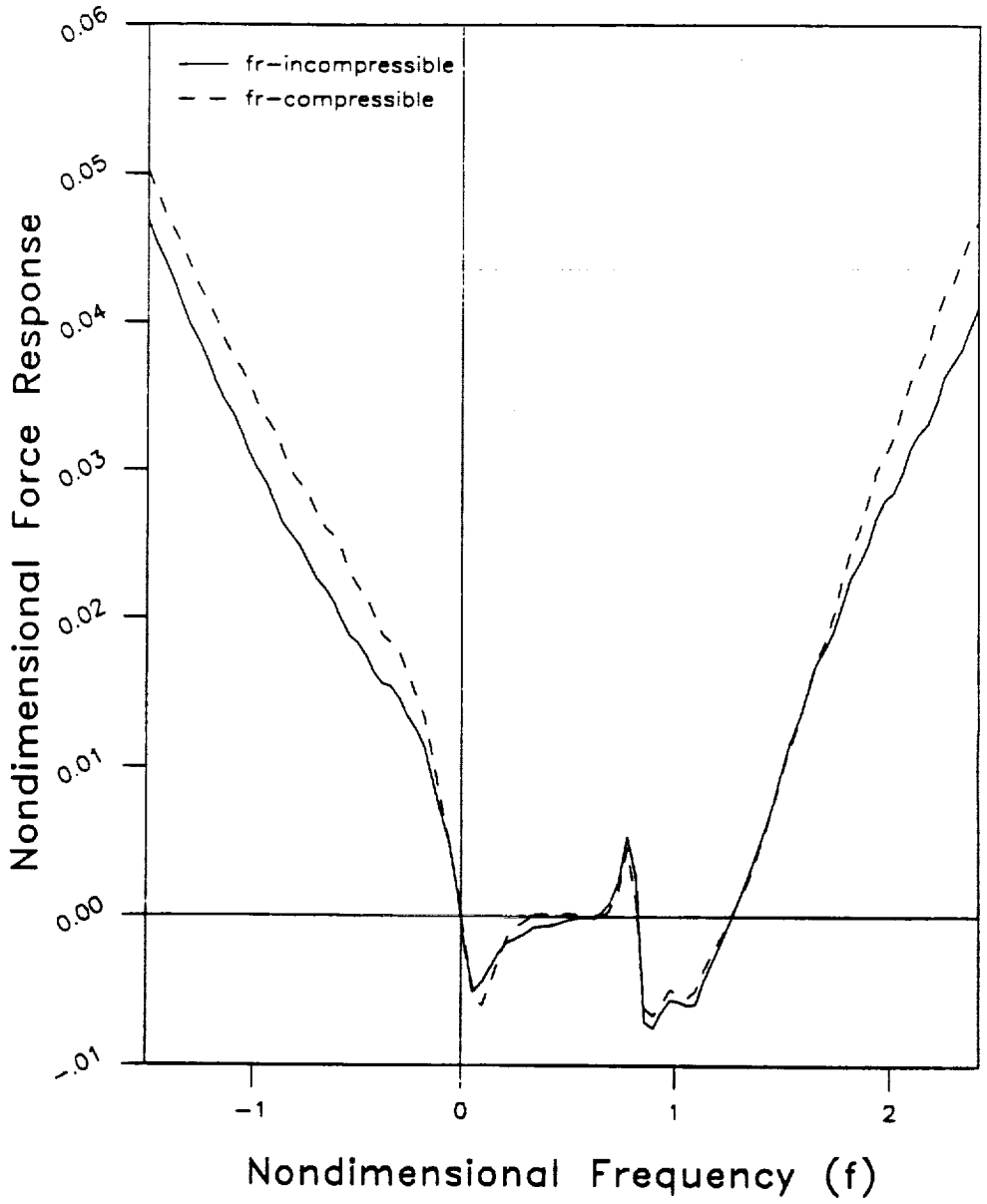

Figure 8 - Radial response for compressible and incompressible models for precession excitation for $u_{\theta 0}(0) = 0.7$

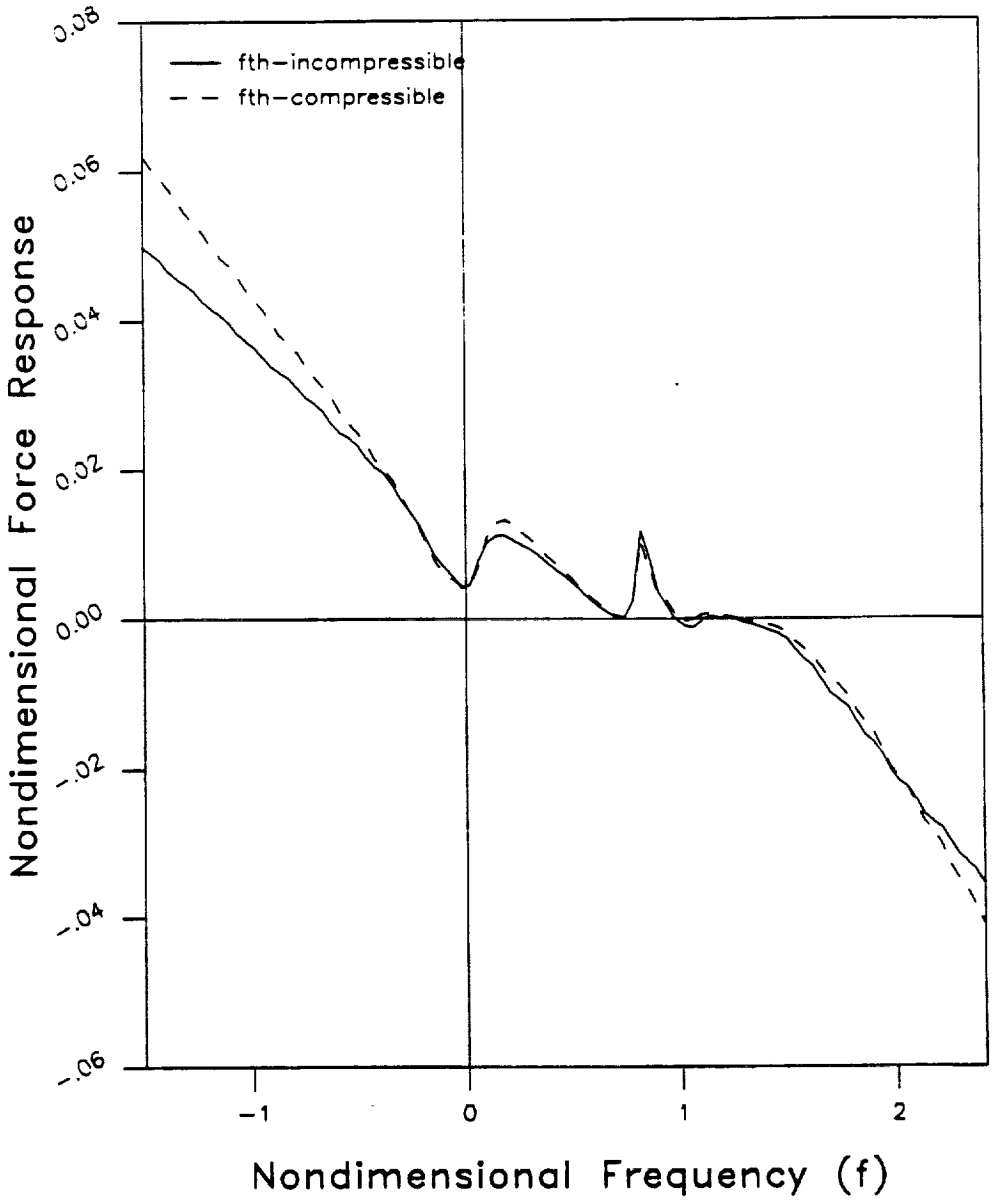

Figure 9 - Circumferential response for compressible and incompressible models for precession excitation for $u_{\theta 0}(0) = 0.7$

show that the effects of compressibility do not affect the results of the model to a great extent over the frequency range considered. As with Childs' results, local resonance peaks occur in the response curves. Two local peaks occur in the response curves, at nondimensional frequency ratios of $f = 0.1$ and $f = 0.8$. For low inlet values of circumferential velocity $u_{\theta 0}(0) = 0.5$, the behavior of the response curves of the compressible model is virtually the same as the results shown for an incompressible model shown by Childs (1989), i.e., the resonance in the response curves diminish at lower values of inlet circumferential velocity.

Complex first-order pressure, path velocity, and circumferential velocity for different nondimensional excitation frequencies along the leakage path produced from the first-order perturbation analysis provide approximate complex modes at the resonant frequencies. The real and imaginary parts of these results are used to obtain amplitude and phase plots at the resonant frequencies. Amplitude and phase plots of first-order nondimensional pressure in the leakage path at the frequency ratios of $f = 0.1$ and $f = 0.8$, where the local peaks occur, are shown in Figures 10 and 11. Complex modes for u_{s1} at the same frequency ratios are shown in Figures 12 and 13.

At the frequency ratio of $f = 0.1$, the amplitude of the pressure along the leakage path steadily increases and has a maximum value at the exit of the leakage path. For the frequency ratio of $f = 0.8$, the maximum pressure amplitude occurs near the middle of the leakage path. The mode shape for u_{s1} at $f = 0.1$ shows a slightly decreasing amplitude along the leakage path, with a minor increase in the amplitude at the exit. As with the mode shape for the pressure distribution at $f = 0.8$, the maximum magnitude occurs near the middle of the seal.

As with Childs' model, the resonant peaks found in this analysis can be attributed to the centrifugal acceleration terms. When the centrifugal acceleration terms are removed from the model, the local peaks in the response curves diminish significantly. The mode shapes at $f = 0.8$ do not support the theory that maximum pressure oscillations at the leakage path exit are causing the seal to melt because the maximum amplification occurs near the middle of the leakage path.

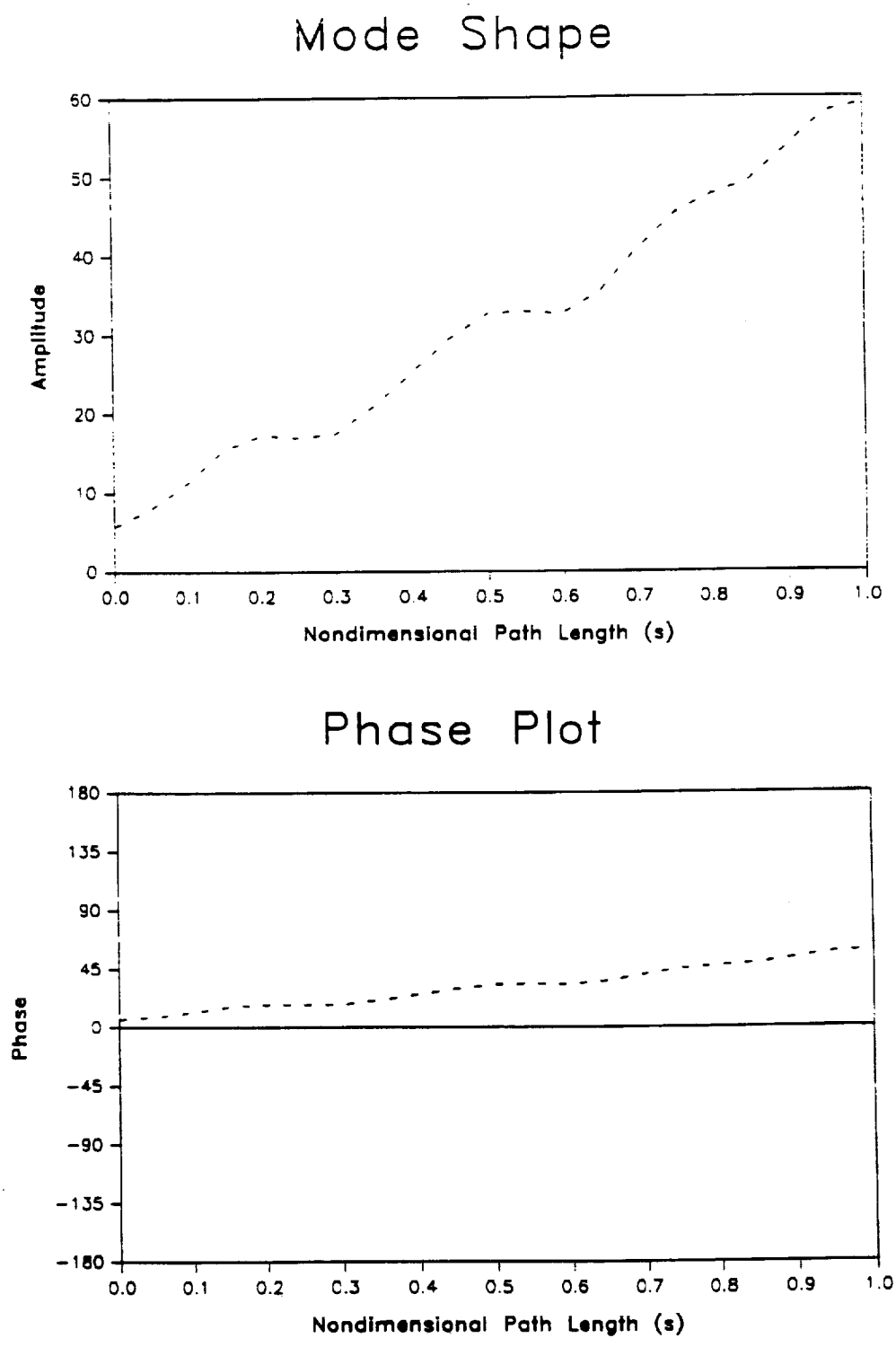

Figure 10 - Amplitude and phase plot of nondimensional pressure p for precessional excitation of compressible model at $f = 0.1$

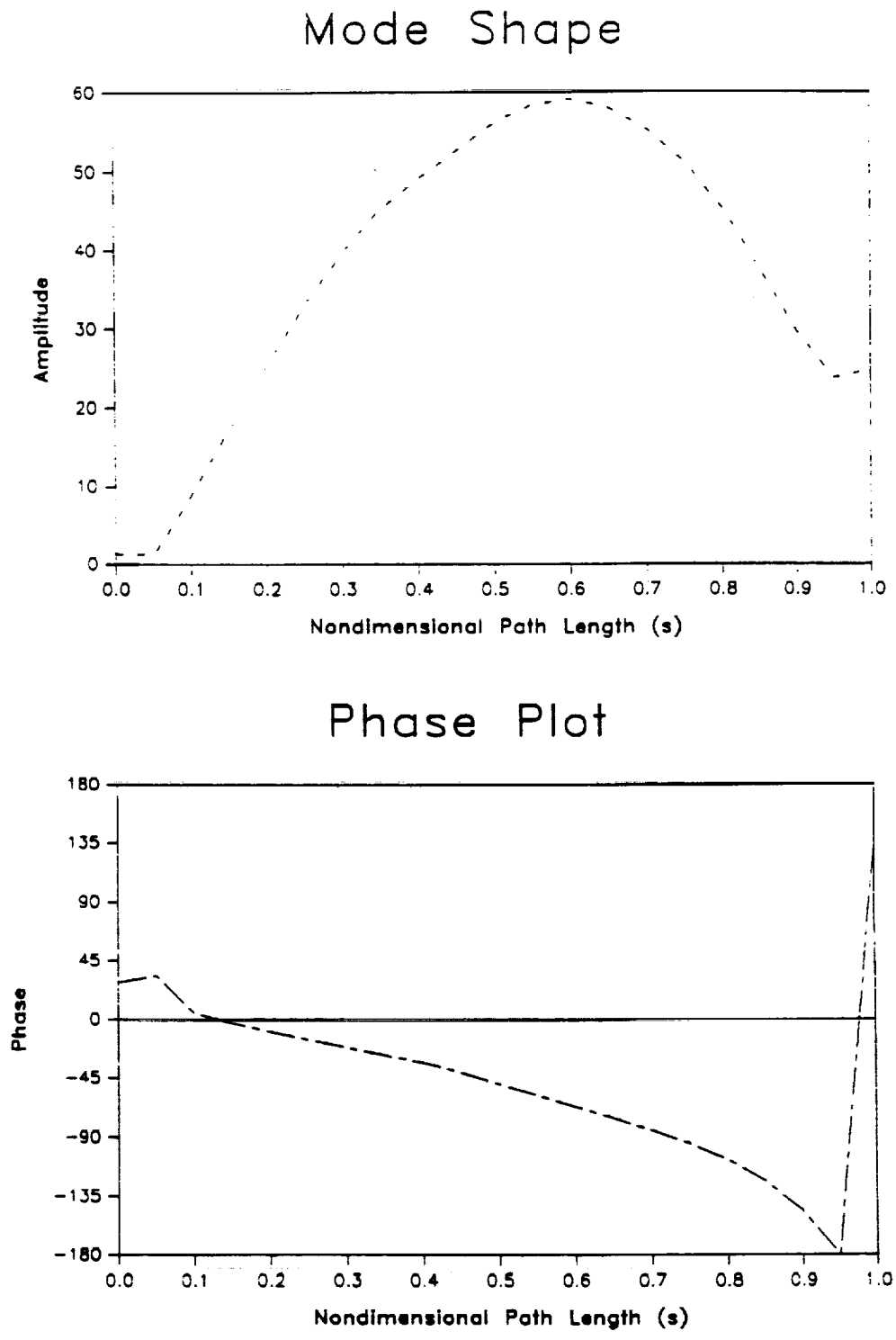

Figure 11 - Amplitude and phase plot of nondimensional pressure p for precessional excitation of compressible model at $f = 0.8$

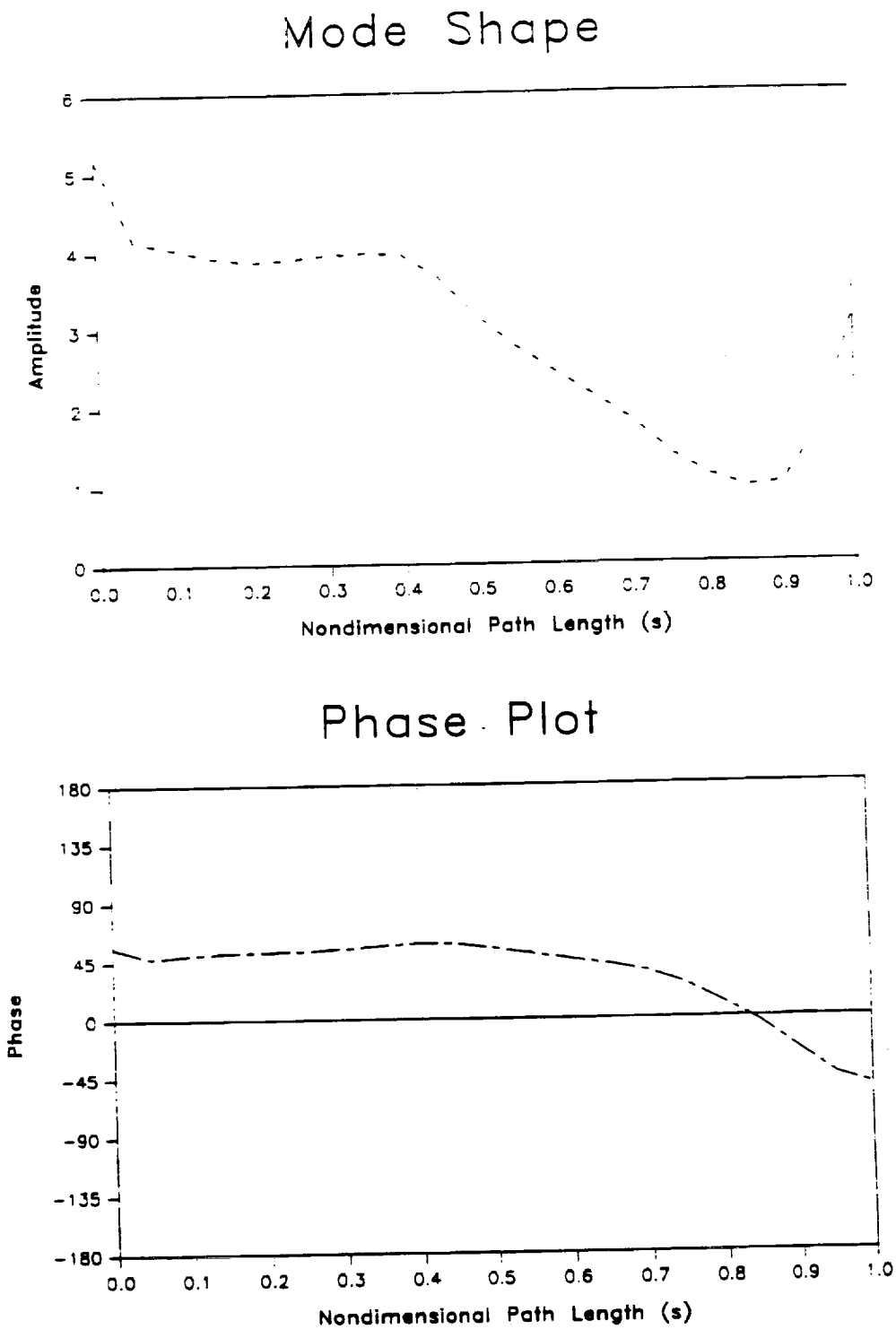

Figure 12 - Amplitude and phase plot for precessional excitation for path velocity u_{s1} of compressible model at $f = 0.1$

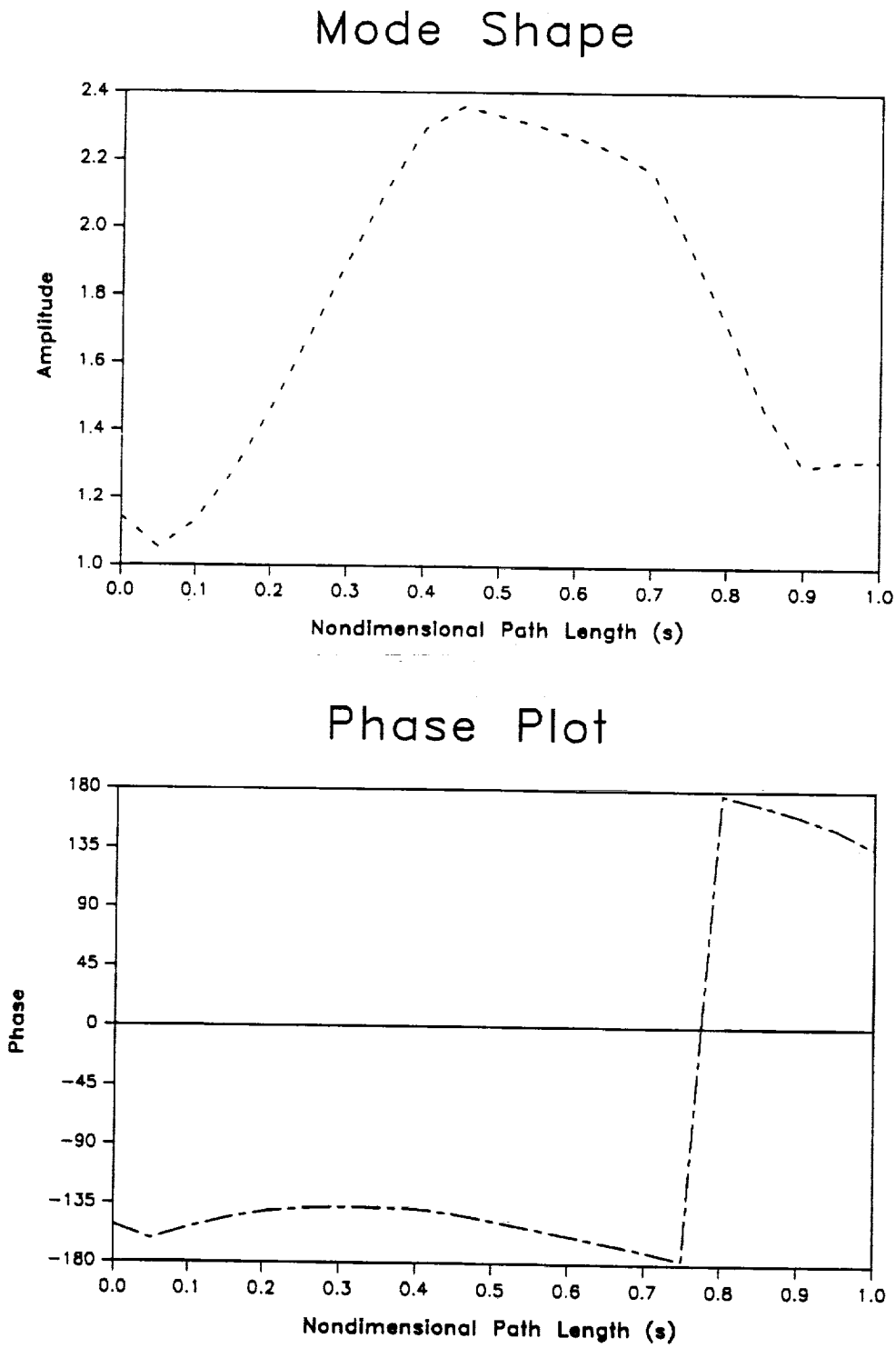

Figure 13 - Amplitude and phase plot for precessional excitation for path velocity u_{s1} of compressible model at $f = 0.8$ and $u_{\theta 0}(0) = 0.7$

Noticeable effects of compressibility upon the model can be seen at higher nondimensional frequency ratios. Figure 14 shows the response curves of the compressible and incompressible models for high frequency ratios. The force responses of the incompressible model continue to grow with increasing f, while the results of the compressible model exhibit peaks corresponding to the natural frequency. This is consistent with classical vibration analysis, with the incompressible model having no natural frequency due to an infinitely high bulk modulus, while the compressible model has a natural frequency corresponding to the compressibility of liquid hydrogen in the model.

6.2 Pressure Excitation

This part of the research involves introducing a time and circumferentially varying impeller discharge pressure to the compressible model. With different excitations involved in this model, new boundary conditions also exist. The pressure perturbation takes the form of the following equation.

- *Supply Pressure-Excitation Perturbation*

$$P_s(\theta,t) = P_{s0} + \epsilon P_{s1}(\theta,t) \tag{45}$$

The occurrence of epsilon in this equation represents the perturbation coefficient for discharge-pressure excitation.

6.2.1 First-Order Equations

Nondimensionalization and perturbation of the general governing equations (6-8) yields the same governing equations for pressure excitation perturbation as for precession excitation governing Eqs. (31-33), except with $h_1 = 0$ for this model. Therefore, the first-order governing equations for pressure excitation will not be presented in this section.

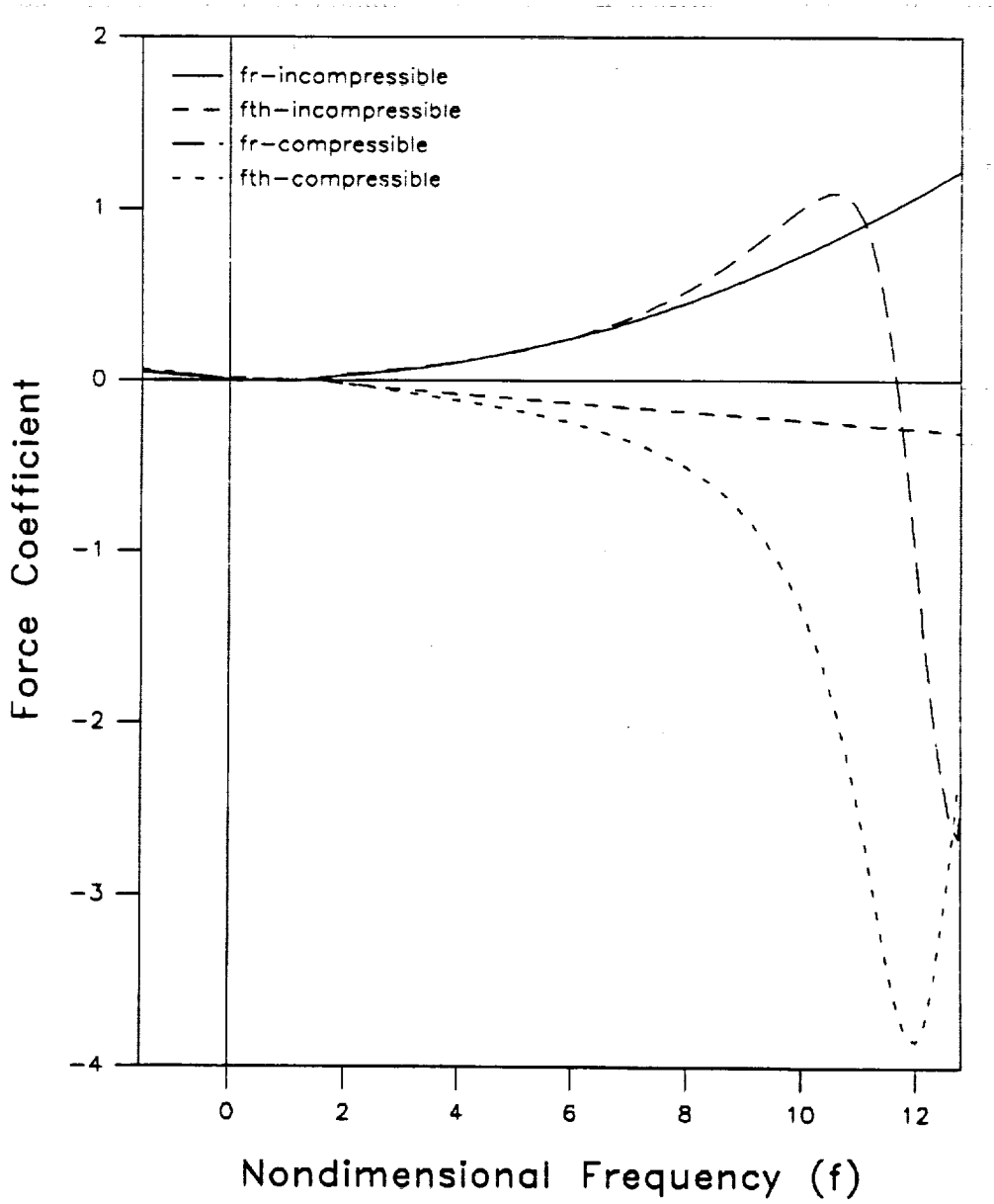

Figure 14 - Nondimensional force response of compressible and incompressible models for precessional excitation for extended frequency range

6.2.2 Boundary Conditions

Nondimensionalization and perturbation of the boundary conditions introduced in Eq. (12-13), the first-order boundary condition can be stated as

$$p_{s1}(\theta,t) - p_1(0,\theta,t) = (1+\xi)u_{s1}(0,\theta,t)\left(1+\frac{(1+\xi)}{2}\frac{d\tilde{p}}{dp}\Big|_0\right)$$
$$p_1(1,\theta,t) - p_{e1}(\theta,t) = C_{de}u_{s0}(1)u_{s1}(1,\theta,t)\left(1+\frac{(1+\xi)}{2}\frac{d\tilde{p}}{dp}\Big|_1\right) \quad (46)$$

$p_{s1}(\theta,t)$, $p_{e1}(\theta,t)$ provide the boundary excitations and take the form,

$$p_{s1}(\theta,t) = e^{j\Omega t}(p_{s1c}\cos n\theta + p_{s1s}\sin n\theta)$$
$$p_{e1}(\theta,t) = e^{j\Omega t}(p_{e1c}\cos n\theta + p_{e1s}\sin n\theta) \quad (47)$$

6.2.3 First Order Solution

The theta and time dependency of the first-order pressure excitation governing equations is eliminated by assuming

$$u_{s1} = e^{jf\tau}(u_{s1c}\cos n\theta + u_{s1s}\sin n\theta)$$
$$u_{\theta 1} = e^{jf\tau}(u_{\theta 1c}\cos n\theta + u_{s1s}\sin n\theta)$$
$$p_1 = e^{jf\tau}(p_{1c}\cos n\theta + p_{1s}\sin n\theta) \quad (48)$$

where n represents the difference of number of impeller blades and vanes, also defined as the number of diametral nodes (Bolleter). Substitution of Eqs. (48) into the first-order pressure excitation governing equations, equating coefficients of cos $n\theta$ and sin $n\theta$, and using complex variables described in Eq. (30) reduces the real equations to three, complex ordinary differential equations

$$\frac{d}{ds}\begin{Bmatrix}\bar{u}_{s1}\\ \bar{u}_{\theta 1}\\ \bar{p}_1\end{Bmatrix} + [B(n,f,s)]\begin{Bmatrix}\bar{u}_{s1}\\ \bar{u}_{\theta 1}\\ \bar{p}_1\end{Bmatrix} = 0 \quad (49)$$

where

$$[B] = \begin{bmatrix} B_{11} & -\frac{jn\omega T}{r} - B_{12} & -\frac{d\tilde{\rho}_0}{ds}\left(\frac{u_{s0}d\tilde{\rho}_0}{\tilde{\rho}_0^2 ds} + \frac{jn\omega T u_{\theta 0}}{\tilde{\rho}_0 r}\right) + jn\omega T\frac{d\tilde{\rho}_0}{ds} + B_{13} \\ \frac{A_{3s}}{u_{s0}} & \frac{A_{2\theta}}{u_{s0}} + \frac{j\Gamma T}{u_{s0}} & A_{4\theta}\frac{d\tilde{\rho}_0}{ds} - j\frac{bL_s}{ru_{s0}\tilde{\rho}_0 R_i} \\ B_{31} & B_{32} & \frac{A_{4s}}{\tilde{\rho}_0} - \frac{B_{33}}{\tilde{\rho}_0}\frac{d\tilde{\rho}_0}{ds} \end{bmatrix} \quad (50)$$

Eq. (49) differs from Eq. (40) in that Eq. (49) is now a function of n with $h_l = 0$. These equations are solved using the method presented by Childs (1992).

6.2.4 First-Order Results

Results from the pressure excitation perturbation analysis using a difference of impeller blades and vanes (n) is presented in this section. Since the SSME HPFTP wearing-ring seal is located at the end of the leakage path ($s = 1$), the results from this section will concentrate on this area of the leakage path. The pressure-oscillation response at the end of the leakage path versus nondimensional excitation frequency corresponding for $n = 11$ is illustrated in Figure 15. The value of $n = 11$ is used because, as mentioned previously, the SSME HPFTP has 24 impeller blades and 13 diffuser vanes, for a difference of 11. Bolleter (1988) explains that the dominant pressure pattern to be expected for this arrangement would have 11 diametral nodes. This is important because it is the value used as n in Eq. (48). Figure 15 shows that the peak pressure oscillation at the exit of the impeller leakage path ($s = 1$) occurs at a nondimensional frequency of about $f = 6.4$ and $f = 7.8$. Bolleter predicts that the peak pressure oscillation should occur as a function of the difference in the number of impeller blades and vanes, presented in Tables 1 and 2.

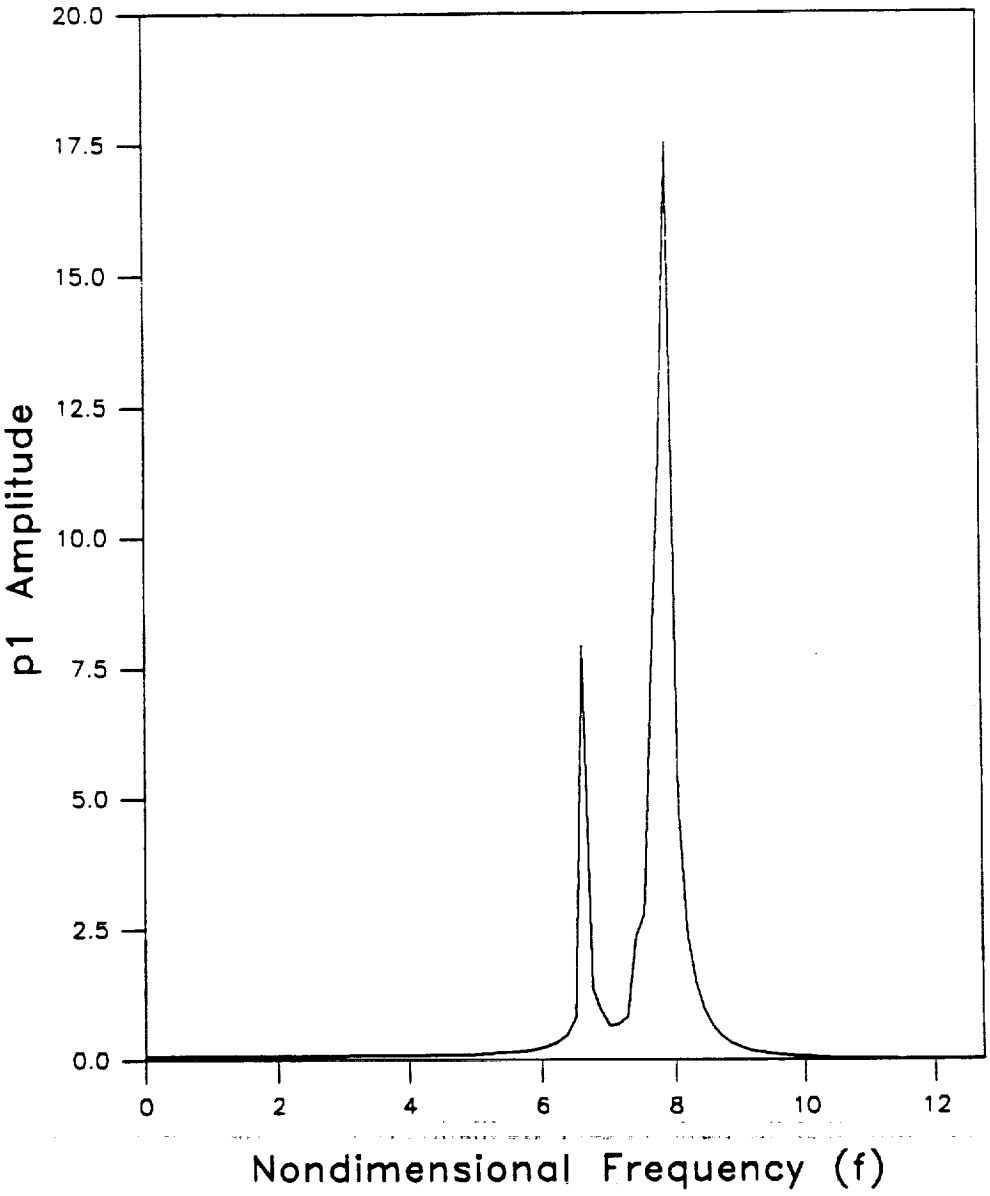

Figure 15 - Pressure oscillation response of compressible model for pressure excitation for $n = 11$ at leakage path exit ($s = 1$) and $u_{s0}(0) = 0.7$

The resonant frequency ratios at $f = 6.5$ and $f = 7.8$ clearly are not functions near the predicted excitation frequencies provided in Table 2 for $n = 11$. None of the other cases tested yielded results which correspond to the values shown in Table 2 for the respective value of n. These results reveal that amplification of peak pressure oscillation does not occur at the expected frequency ratio. At the predicted frequency ratios, the cases tested for this model showed that an attenuation, rather than an amplification of the pressure waves occurred.

Table 1 - $(n_1 - n_2)$ for various combinations of multiples of impeller blades and vanes

n_2 \ n_1	24	48	96
13	11	35	83
26	-2	22	70
39	-15	9	57

Table 2 - Expected peak nondimensional frequency ratios, f or, $\{n/(n_1 - n_2)\}$, for various combinations of multiples of impeller blades and vanes

n_2 \ n_1	24	48	96
13	2.18	1.37	1.16
26	-12.00	2.18	1.37
39	-1.60	5.33	1.68

Amplitude and phase plots (Figures 16 and 17) of the pressure oscillation for the two resonant frequency ratios found for n for the compressible pressure excitation model show that the peak pressure oscillation occurs at the exit of the leakage path. This result helps to support the hypothesis that pressure oscillations at the leakage path

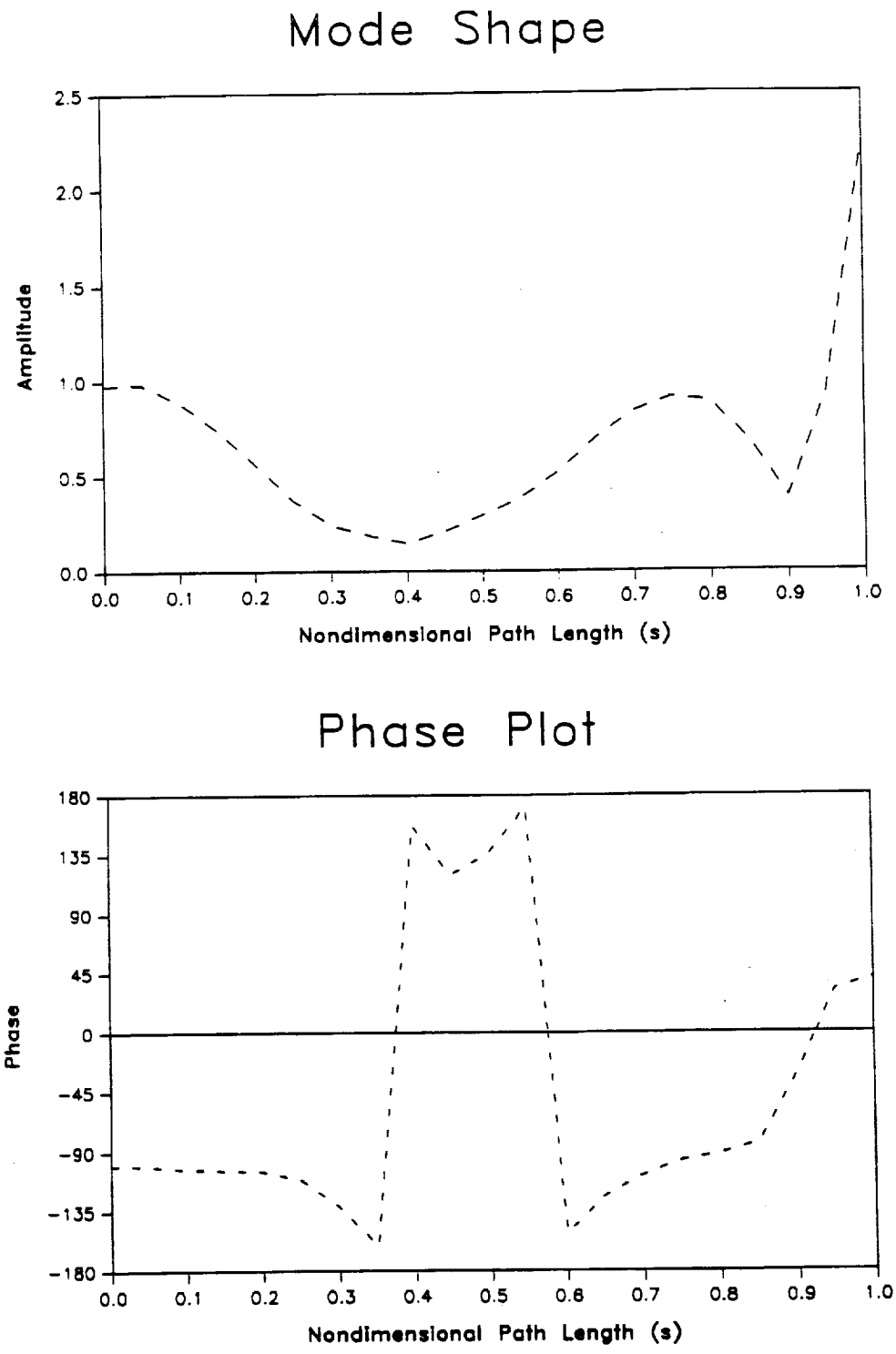

Figure 16 - Amplitude and phase plot for pressure oscillation of compressible model inside impeller leakage path at $f = 6.4$ for $n = 11$ and $u_{\theta 0}(0) = 0.7$

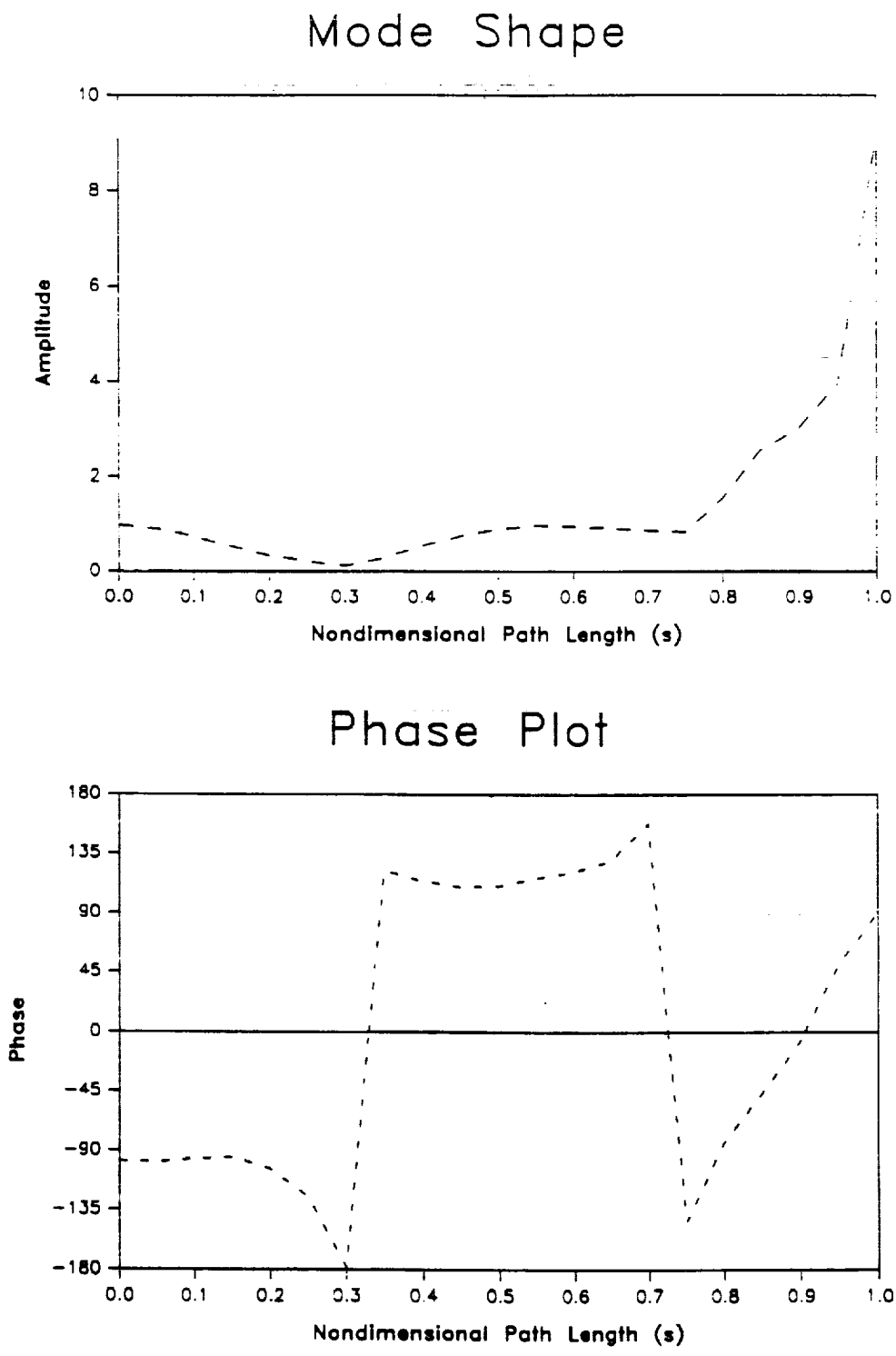

Figure 17 - Amplitude and phase plot for pressure oscillation of compressible model inside impeller leakage path at $f = 7.5$ for $n = 11$ and $u_\theta(0) = 0.7$

exit are causing the seal to melt. However, the result does not provide enough evidence to provide a very plausible explanation for the behavior exhibited by the wearing ring seal.

The response of the compressible model for other values of n is plotted in Figure 18. The graph shows the relationship of the peak pressure oscillation response to the number of diametral nodes. The nondimensional excitation frequency ratio at which the peak pressure oscillation occurs increases as the number of diametral nodes increase, consistent with Childs' analysis (1992). However, unlike Childs' results, where the magnitude of the peak amplitude stays relatively constant, regardless of n, the results produced from the compressible model show that the amplitude of the pressure oscillations increases as n increases. The effects of added compressibility to the results of this model is greatly enhanced compared to results of the precession excitation model. But, as with the precession excitation analysis, the influence due to compressibility effects is only noticeable at higher nondimensional frequencies.

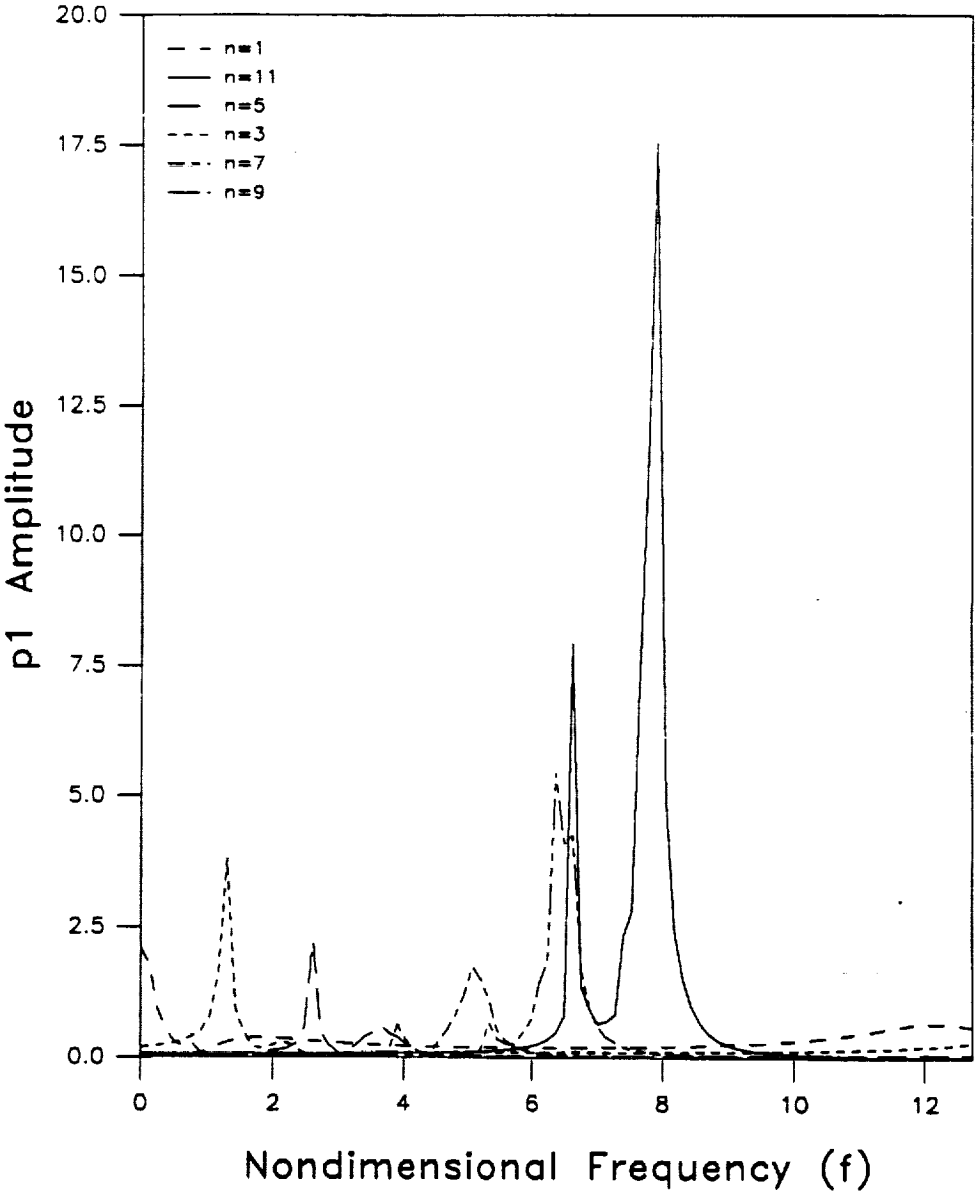

Figure 18 - Pressure oscillation response for pressure oscillation of compressible model with multiple n and $u_{e0}(0) = 0.7$

CHAPTER VII
FIRST ORDER EQUATIONS AND SOLUTIONS FOR ACOUSTIC MODELS

For acoustics analysis, the temporal acceleration terms are the only acceleration terms which remain from the set of general governing equations. A highly reasonable assumption may be made that the contributions from the convective, Coriolis, and centrifugal acceleration terms are negligible compared to the temporal acceleration terms in the realm of ordinary acoustics ($M^2 \ll 1$) (Thompson, 1988). However, due to the high Mach number with which the working fluid in the SSME HPFTP operates ($M \cong 0.4$), the general perturbation fluid model and the acoustic model must be compared to investigate the effects of the convective, Coriolis, and centrifugal acceleration terms in an acoustic analysis.

The zeroth-order solution for the acoustics models do not change from the previous results obtained because the zeroth-order equations and solution remain the same .

7.1 Precession Excitation Model

7.1.1 First Order Equations

First-order governing equations for the acoustic precession excitation model can be obtained by removing the effects of fluid mechanics, i.e., the convective, the Coriolis, and the centrifugal acceleration terms from the general perturbation governing equations given in 5.2.2, Eqs. (24-26). Removing the convective acceleration terms, $u_\theta du_\theta/ds$ $u_s du_s/ds$, the Coriolis acceleration term, $2u_{s_0}dr/rds$, and $-2u_{\theta_0}dr/(b^2rds)$, representing centrifugal acceleration, from the continuity Eq. (24) yields the first-order governing acoustic continuity governing Eq. (51). The first-order governing acoustic equations for the path and circumferential momentum are obtained by removing the convective acceleration terms from Eqs. (25-26).

- *Continuity Equation*

$$\tilde{\rho}_0\frac{\partial h_1}{\partial \tau}+h_0\frac{\partial \tilde{\rho}_1}{\partial \tau}+\frac{1}{T\omega}\left[h_1\frac{\partial(\tilde{\rho}_0 u_{s0})}{\partial s}+u_{s1}\frac{\partial(\tilde{\rho}_0 h_0)}{\partial s}+\tilde{\rho}_1\frac{\partial(u_{s0}h_0)}{\partial s}\right]=0 \tag{51}$$

- *Path-Momentum Equation*

$$\frac{1}{\tilde{\rho}_0}\frac{\partial p_1}{\partial s}+u_{\theta 1}A_{2s}+u_{s1}A_{3s}+\tilde{\rho}_1 A_{4s}+T\omega\frac{\partial u_{s1}}{\partial \tau}=h_1 A_{1s} \tag{52}$$

- *Circumferential-Momentum Equation*

$$\frac{b}{r}\frac{L_s}{R_i\tilde{\rho}_0}\frac{\partial p_1}{\partial \theta}+u_{\theta 1}A_{2\theta}+u_{s1}A_{3\theta}+\tilde{\rho}_1 A_{4\theta}+T\omega\frac{\partial u_{\theta 1}}{\partial \tau}=h_1 A_{1\theta} \tag{53}$$

7.1.2 First-Order Precession Excitation Solution

The theta dependency of Eqs. (51-53) can be eliminated by substituting the solution format presented in Eq. (29). The three resulting complex equations in the independent variables s and τ after introducing the complex variables of Eq. (32) are

- *Continuity Equation*

$$\begin{aligned}\frac{\partial \underline{u}_{s1}}{\partial s}-\frac{j\omega T}{r}\underline{u}_{\theta 1}+\underline{u}_{s1}\left[\frac{1}{h_0}\frac{\partial h_0}{\partial s}+\frac{1}{\tilde{\rho}_0}\frac{\partial \tilde{\rho}_0}{\partial s}\right]&=\underline{h}_1\left[\frac{u_{s0}}{h_0^{\,2}}\frac{\partial h_0}{\partial s}+j\frac{\omega T}{h_0 r}u_{\theta 0}\right]\\ +\underline{\tilde{\rho}}_1\left[j\frac{\omega T}{\tilde{\rho}_0 r}u_{\theta 0}+\frac{u_{s0}}{\tilde{\rho}_0^{\,2}}\frac{\partial \tilde{\rho}_0}{\partial s}\right]-\frac{\omega T}{h_0}\frac{\partial \underline{h}_1}{\partial \tau}-\frac{u_{s0}}{h_0}\frac{\partial \underline{h}_1}{\partial s}-\frac{\omega T}{\tilde{\rho}_0}\frac{d\underline{\tilde{\rho}}_1}{dp_1}\frac{\partial p_1}{\partial \tau}\end{aligned} \tag{54}$$

- *Path-Momentum Equation*

$$\frac{\partial p_1}{\tilde{\rho}_0 \partial s}+\underline{u}_{\theta 1}A_{2s}+\underline{u}_{s1}A_{3s}+\underline{\tilde{\rho}}_1 A_{4s}+T\omega\frac{\partial \underline{u}_{s1}}{\partial \tau}=\underline{h}_1 A_{1s} \tag{55}$$

- *Circumferential-Momentum Equation*

$$-\frac{b}{r}\frac{L_s}{R_i}\frac{p_1}{\tilde{\rho}_0} + u_{\theta 1}A_{2\theta} + u_{s1}A_{3\theta} + \tilde{p}_1 A_{4\theta} + T\omega\frac{\partial u_{\theta 1}}{\partial \tau} = h_1 A_{1\theta} \tag{56}$$

Assuming the harmonic seal motion described in section 6.1, Eq. (38), the three governing equations reduce to two differential equations of motion of the form,

$$\frac{d}{ds}\begin{Bmatrix} u_{s1} \\ p_1 \end{Bmatrix} + [C]\begin{Bmatrix} u_{s1} \\ p_1 \end{Bmatrix} = \begin{pmatrix} q_0 \\ \epsilon \end{pmatrix}\begin{Bmatrix} g_7 \\ g_8 \end{Bmatrix} \tag{57}$$

where

$$\begin{Bmatrix} g_7 \\ g_8 \end{Bmatrix} = \begin{pmatrix} L \\ L_s \end{pmatrix}\begin{Bmatrix} \dfrac{u_{s0}}{\tilde{\rho}_0}\dfrac{d\tilde{\rho}_0}{dp}G_q + F_2 + j\dfrac{\Gamma T}{h_0}\dfrac{dz}{ds} - j\dfrac{\omega T}{r}\dfrac{A_{1\theta}}{(A_{2\theta} + j\omega Tf)} \\ G_q - \dfrac{A_{2s}A_{1\theta}}{(A_{2\theta} + j\omega Tf)} \end{Bmatrix} \tag{58}$$

The [C] matrix elements are given in Appendix C.

The $du_{\theta 1}/ds$ term has dropped from the governing equations and thus $u_{\theta 1}$ can be solved directly without integrating the partial differential equations, yielding,

$$u_{\theta 1} = \left[h_1 A_{1\theta} - u_{s1}A_{3\theta} + \left(j\frac{b}{r}\frac{L_s}{R_i\tilde{\rho}_0} - \frac{d\tilde{\rho}_0}{dp}A_{4\theta}\right)p_1\right] / (A_{2\theta} + j\omega Tf) \tag{59}$$

Results to these equations are obtained using the same solution procedure and boundary conditions described for the first-order precession excitation equations in section 6.2.2. The solution to these sets of equations can then be used to calculate the force and moment coefficients in the impeller leakage path for the acoustic case where classical acoustic assumptions are made.

C-2

7.1.3 First-Order Results

The nondimensional radial force coefficient responses for the general perturbation and acoustic cases are shown in Figure 19. The response curves for the circumferential force coefficients are shown in Figure 20. The response curves for the acoustic case are less erratic in behavior, and the peaks exhibited by the compressible model totally disappear. This shows that the convective, Coriolis, and centrifugal acceleration terms do affect the results of the compressible model to a considerable extent at low frequencies. Childs (1989) correctly predicted that the centrifugal acceleration terms caused the resonance in the response curve. Although the results of the two models do not differ quantitatively, the trend exhibited by both models are similar, as evidenced by Figures 20 and 21.

At higher values of nondimensional frequency, the effects of removing the fluid mechanics terms from the model is shown in Figure (21). The two models show about the same results. The natural frequency of the acoustic model is slightly lower and the peaks are slightly higher. Mode shapes for pressure oscillations at $f = 11.5$ and $f = 12$ are shown in Figures 22 and 23. The mode shapes show that, at these frequencies, the pressure oscillations are not the cause of the uncharacteristic behavior of the exit wearing ring seal due to a precession excitation. The mode shapes do not show conclusively that the pressure oscillations are occurring at the exit of the seal.

7.2 Pressure Excitation Model

7.2.1 First-Order Equations

The equations obtained for the first-order acoustic pressure excitation perturbation use the same procedure as for the first-order acoustic precession excitation shown in section 7.1.1. The boundary conditions and perturbation excitation are defined by the equations used for the general first-order pressure excitation solution given in section 6.2. The resulting governing equations for pressure excitation of the acoustic model are the same as those given in section 7.1.1, except with h_l being zero, analogous with the results obtained for the pressure excitation equations for the general perturbation model.

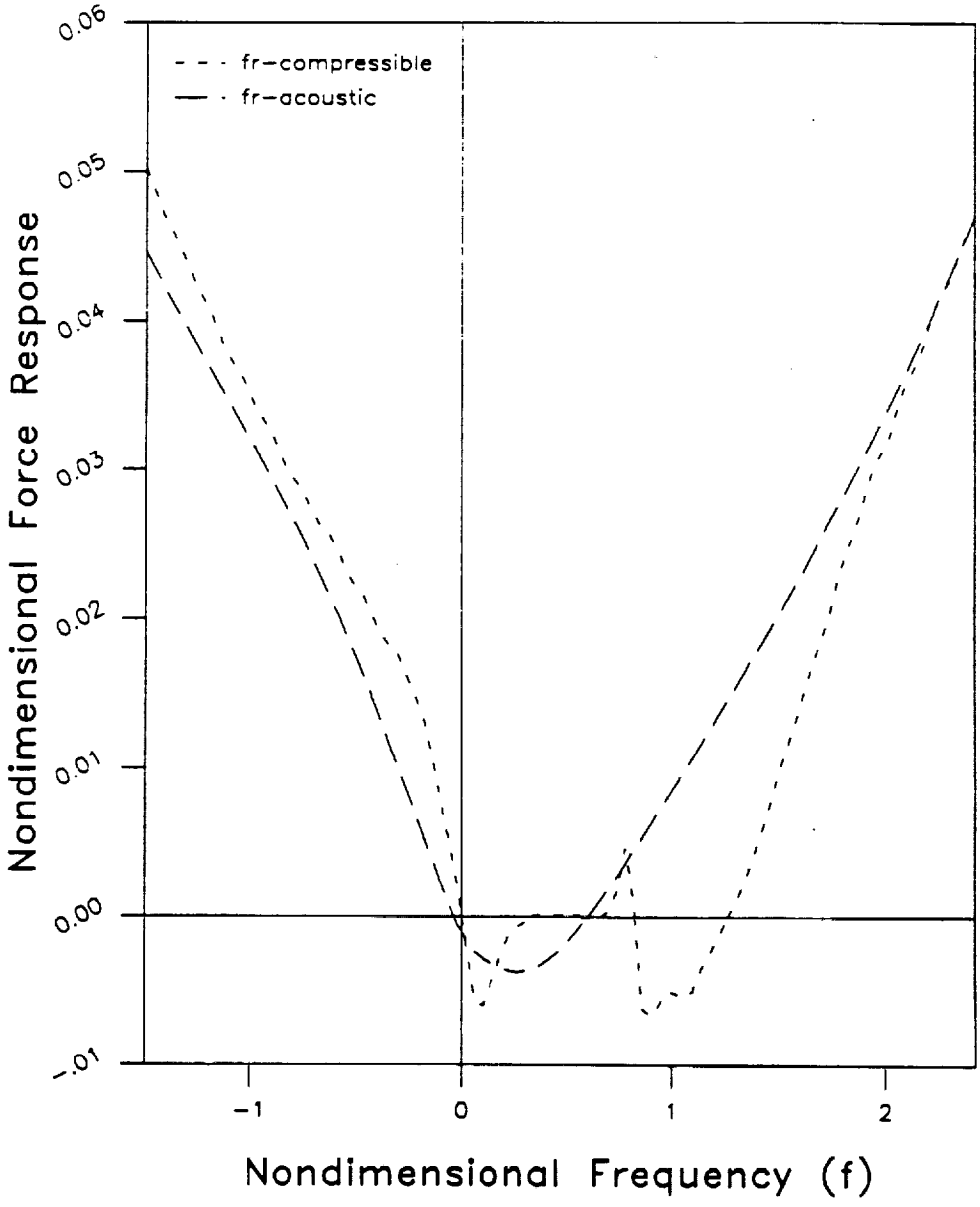

Figure 19 - Radial response for acoustic and compressible models for precessional excitation for $u_{w0}(0) = 0.7$

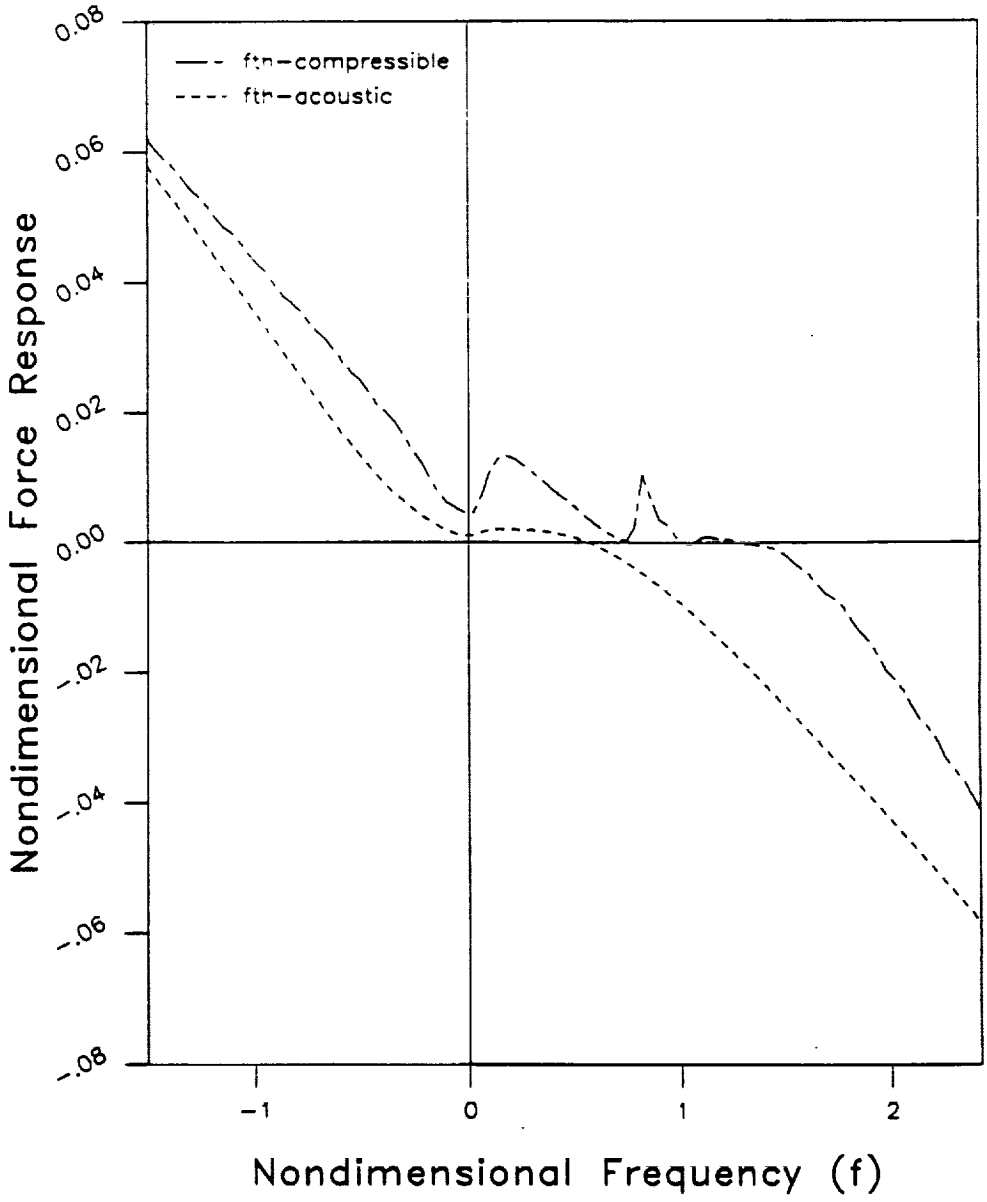

Figure 20 - Circumferential force response for acoustic and compressible models for precessional excitation for $u_{\infty}(0) = 0.7$

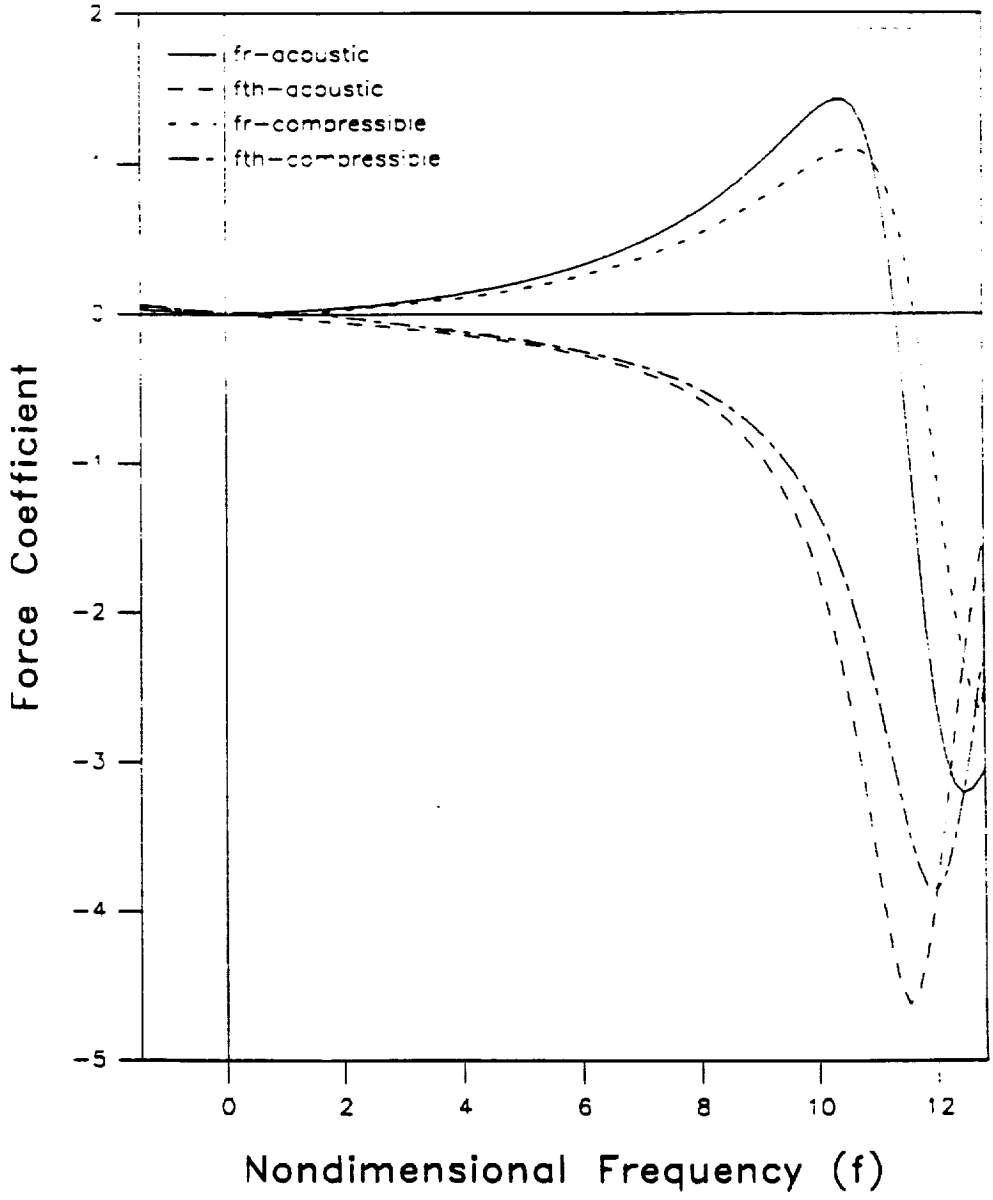

Figure 21 - Force response coefficient for acoustic and compressible models at extended frequency ratios

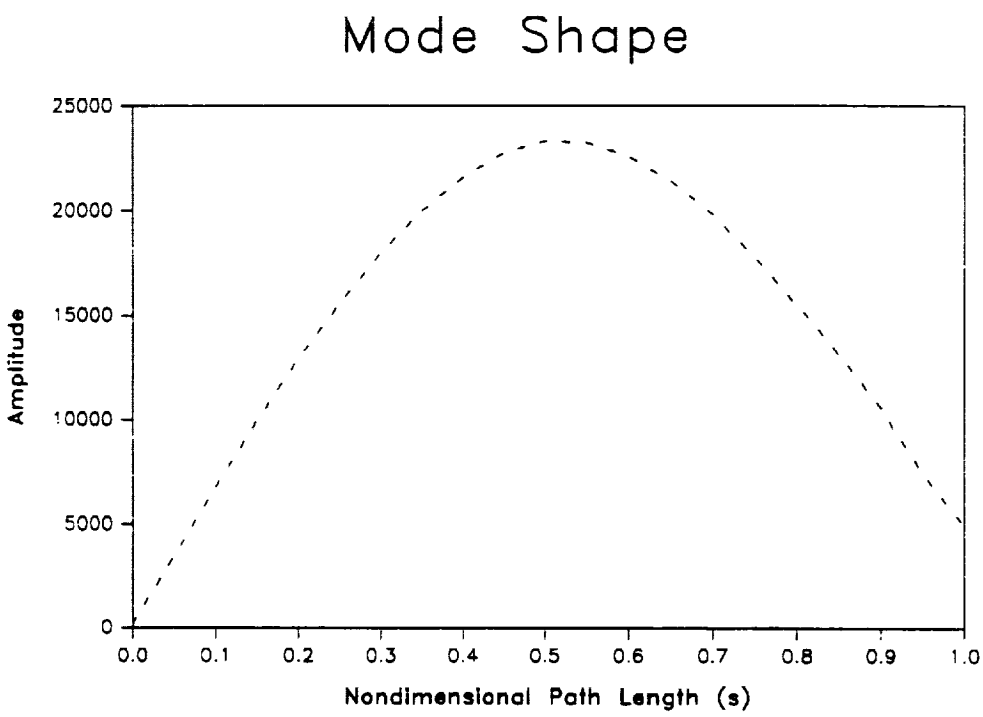

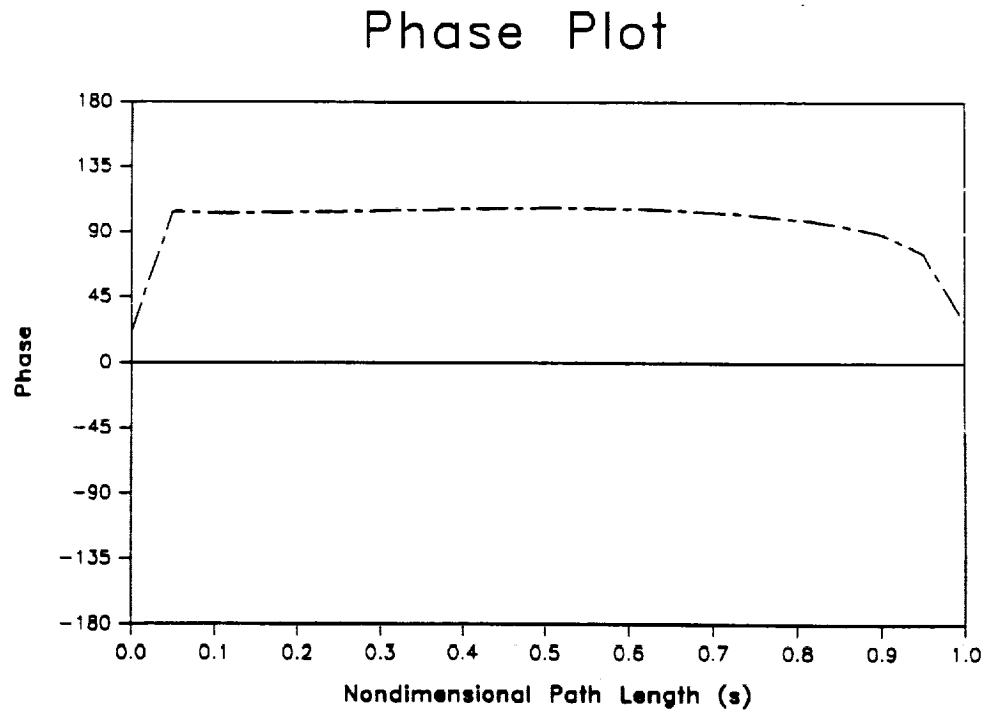

Figure 22 - Amplitude and phase plot of nondimensional pressure of acoustic model vs. path length at $f = 11.5$ for $u_{60}(0) = 0.7$

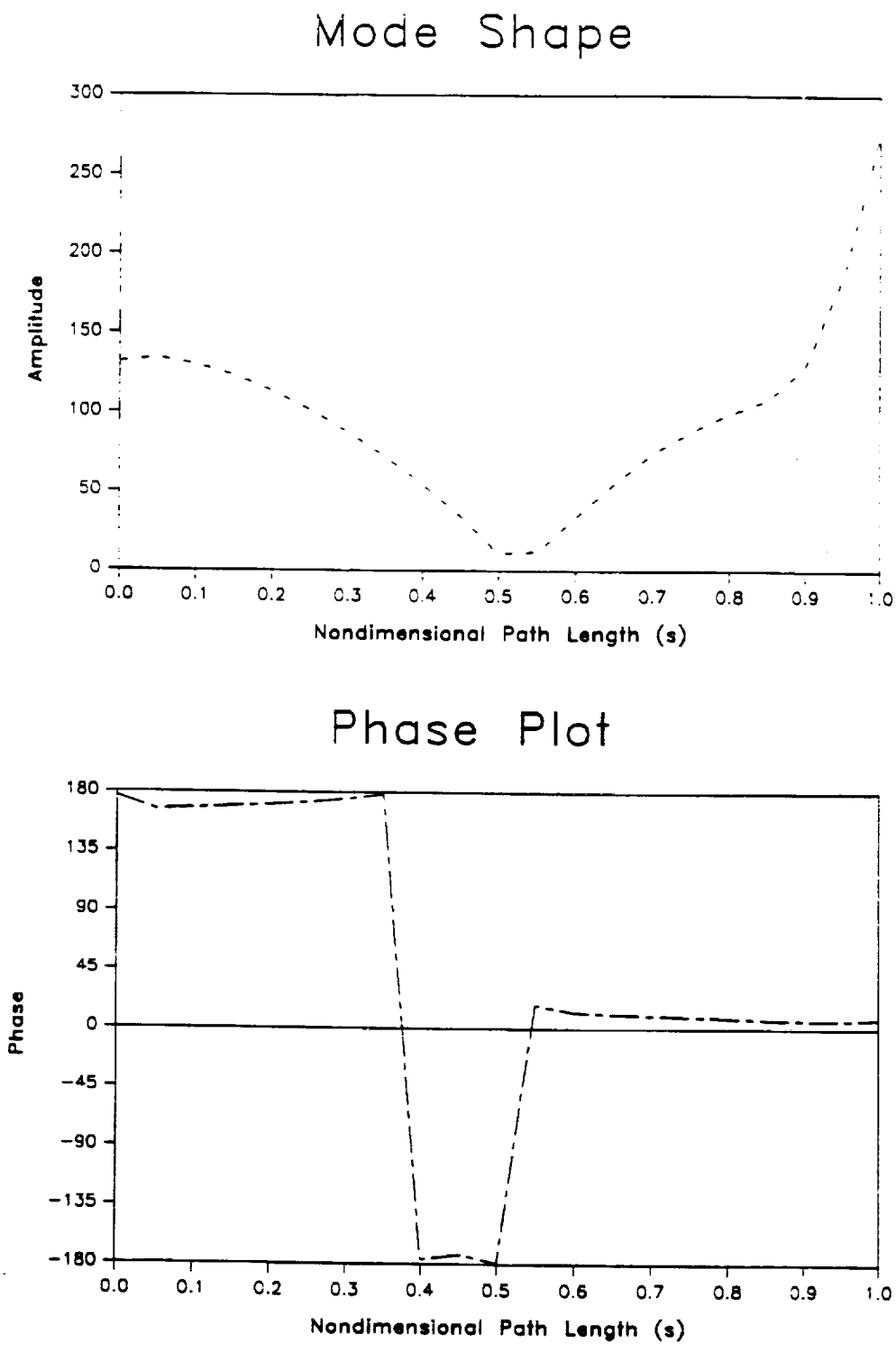

Figure 23 - Pressure mode shape and phase plot of acoustic model vs. path length at $f = 12.0$ for $u_\theta(0) = 0.7$

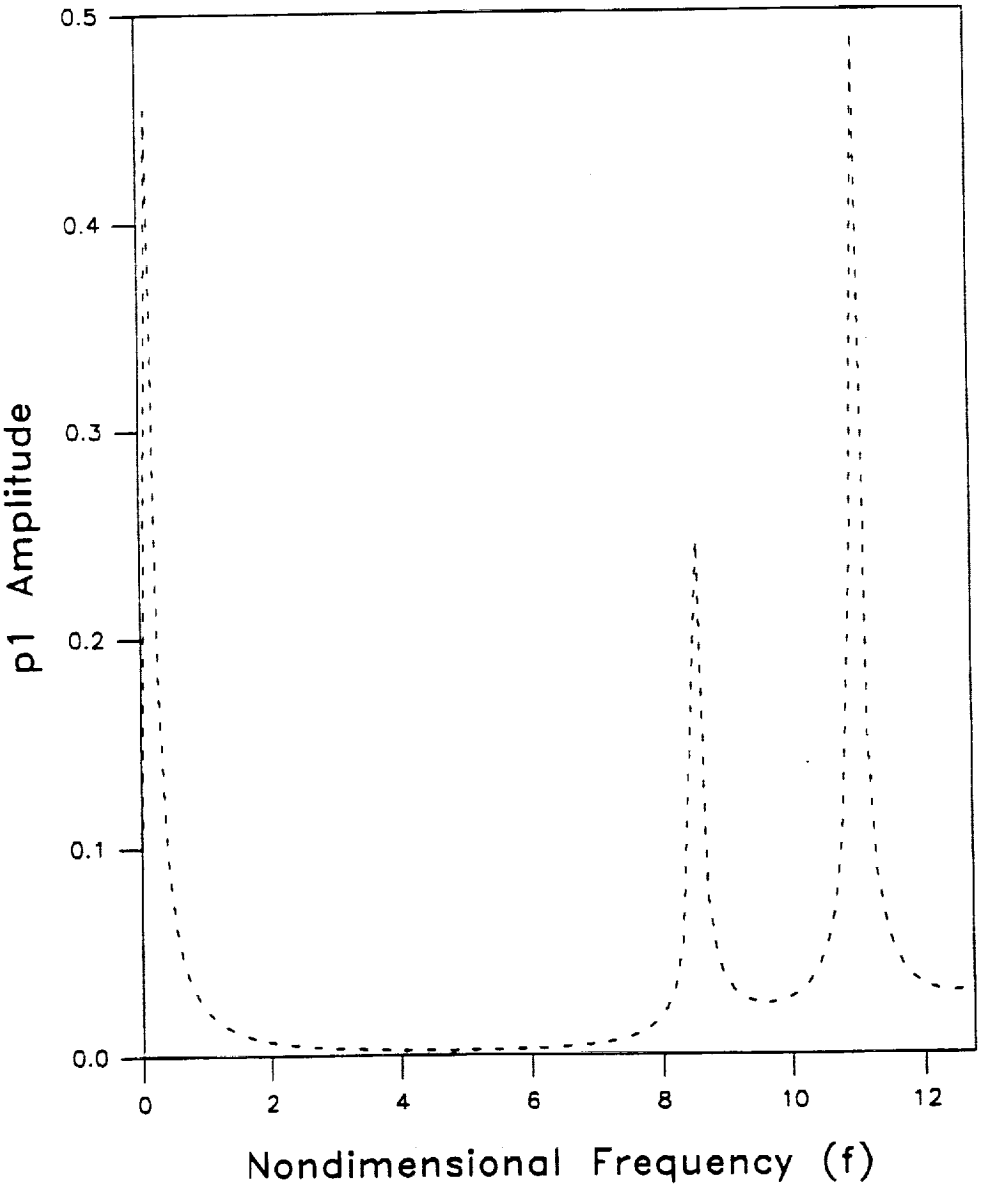

Figure 24 - Acoustic response for impeller discharge pressure excitation for $n = 11$ for $u_{60}(0) = 0.7$

7.2.2 First-Order Pressure Excitation Solution

Using Eq. (48) to eliminate the theta and time dependency from the first-order pressure excitation of the acoustic model and using the pressure excitation perturbation described in Eq. (45), the resulting governing equations can be represented as,

$$\frac{d}{ds}\begin{Bmatrix} u_{s1} \\ p_1 \end{Bmatrix} + [D]\begin{Bmatrix} u_{s1} \\ p_1 \end{Bmatrix} = 0 \tag{60}$$

Where elements of [D] are provided in Appendix D.

In addition to h_1 being zero, Eq. (60) also is a function of n, unlike Eq. (57).

7.2.3 First-Order Results

Comparison of the general perturbation model and the acoustic model for $n=11$ shows that the peak pressure amplification around $f = 7.8$ displayed by the general perturbation model almost totally disappears for the acoustics model. From Figure 24, the results for the acoustics model show that no amplification of the pressure oscillation occurs, but rather, an attenuation of the pressure oscillation at all frequency ratios. It can be concluded from this result that the convective, Coriolis, and centrifugal acceleration terms contribute significantly to the results of a bulk flow model when a pressure excitation is used as the perturbation parameter of the bulk flow model. The results here also differ with respect to the location of the resonant peaks in the nondimensional frequency range tested. For the acoustic model, the local peaks do not match with those of the compressible model.

The sharp peak of the pressure amplitude near a frequency ratio of $f = 0.0$ is inherent in all the models (compressible, incompressible, and acoustic), shown in Figure 25. The phenomenon causing this resonant excitation is not yet understood and cannot be explained. However, the fact that this resonance occurs in all three models explains that neither the compressibility or the acoustics effects of the models affects this resonant frequency. Also, the fact that the frequency at which resonance occurs is near $f = 0.0$, indicates that this peak could be the response to a free vibration of

the fluid inside the leakage path.

Figure 26 shows the first-order pressure response for multiple cases of n. The frequency responses due to different n show no quantitative trend with respect to n. Unlike the compressible model, where the pressure response showed a definite, noticeable response to different n, the acoustic model shows little quantitative and qualitative response to different n value.

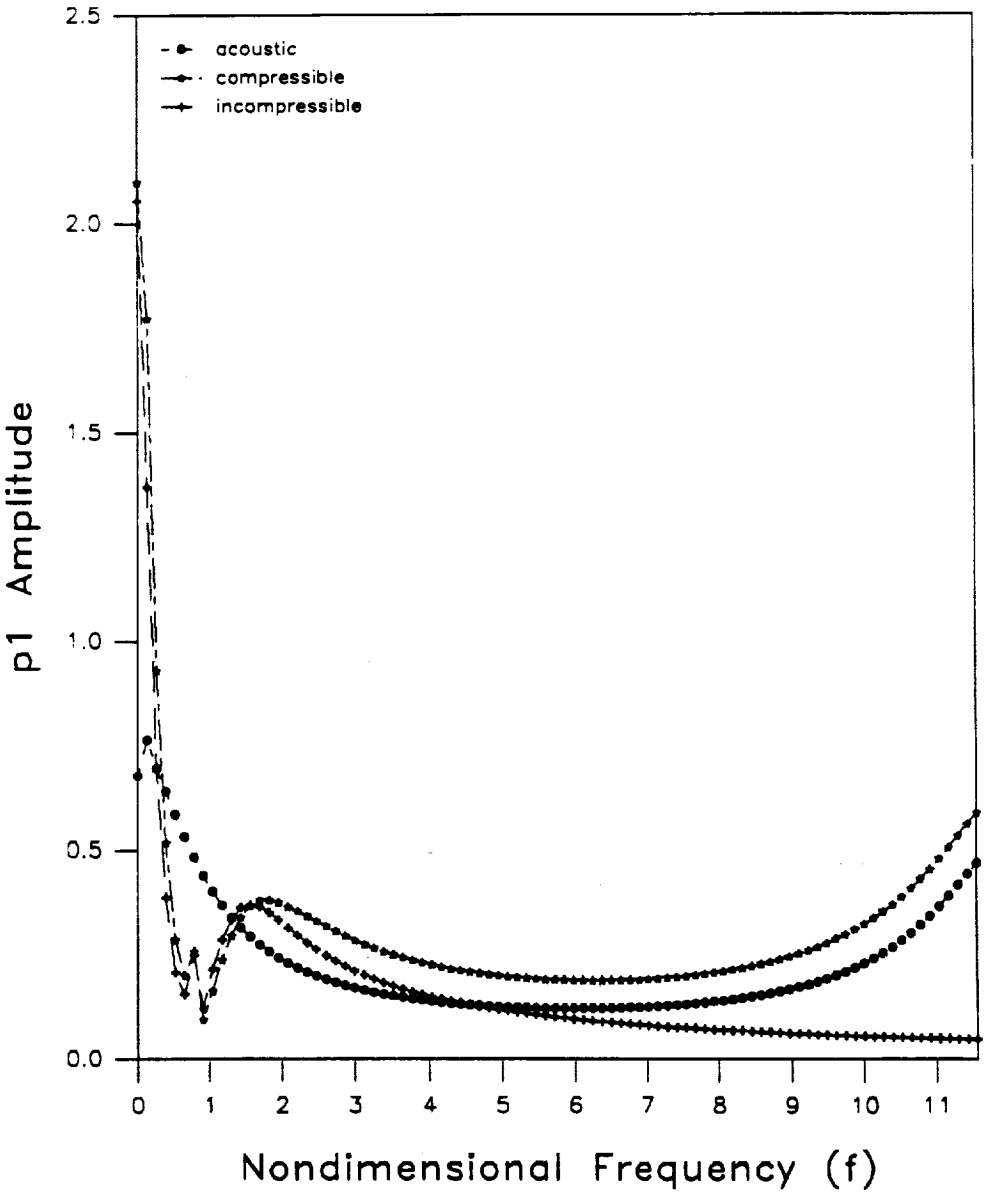

Figure 25 - Pressure response of incompressible, compressible, and acoustic model for impeller discharge pressure excitation for $n = 1$ for $u_{60}(0) = 0.7$

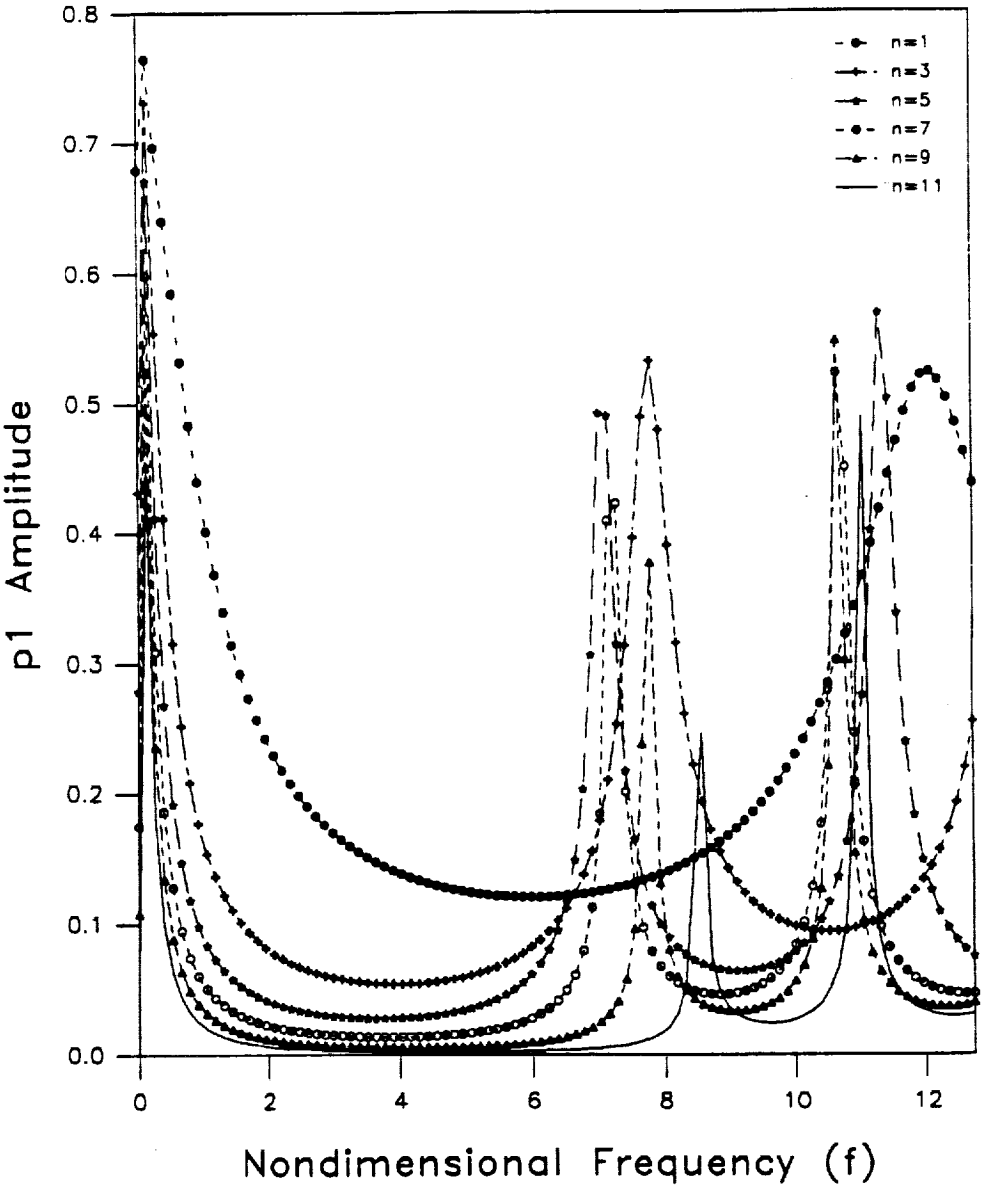

Figure 26 - Pressure response for pressure excitation for multiple *n*

CHAPTER VIII
SUMMARY AND CONCLUSIONS

A modified approach to Childs' previous work (1989,1992) on fluid-structure interaction forces in the leakage path between an impeller shroud and its housing is presented in this thesis. Three governing equations consisting of a continuity, path-momentum, and circumferential-momentum equations were developed to describe the leakage path inside a pump impeller. Radial displacement perturbations were used to solve for radial and circumferential force coefficients. In addition, impeller-discharge pressure disturbances were used to obtain pressure oscillation responses due to precessing impeller pressure wave pattern. Childs' model was modified from an incompressible model to a compressible barotropic-fluid model (the density of the working fluid is a function of the pressure and a constant temperature only). Results obtained from this model yielded interaction forces for radial and circumferential force coefficients. Radial and circumferential forces define reaction forces within the impeller leakage path.

An acoustic model for the same leakage path was also developed. The convective, Coriolis, and centrifugal acceleration terms are removed from the compressible model to obtain the acoustics model. The compressible model is compared with the incompressible model and the acoustic model. A solution due to impeller discharge pressure disturbances model was also developed for the compressible and acoustic models. The results from these modifications are used to determine what effects additional perturbation terms in the compressible model have on the acoustic model.

The results show that the additional fluid mechanics terms in the compressible model do cause resonances (peaks) in the force coefficient response curves. However, these peaks only occurred at high values of inlet circumferential velocity ratios. The peak pressure oscillation was shown to occur at the wearing ring seal. Introduction of impeller discharge disturbances with n diametral nodes showed that maximum peak

pressure oscillations occurred at nondimensional excitation frequencies of $f = 6.4$ and $f = 7.8$ for this particular pump. Bolleter's results suggest that for peak pressure oscillations to occur at the wearing ring seal, the nondimensional excitation frequency should be on the order of $f = 2.182$ for $n = 11$. The resonances found in this research do not match those predicted by Bolleter. At the predicted frequencies given by Bolleter, the compressible model shows an attenuation of the pressure oscillations at the seal exit. This does not provide a plausible explanation for the unusual behavior exhibited by the wearing ring seal.

The compressibility of the fluid does not have a significant influence on the model at low values of nondimensional frequency. At high values of nondimensional frequency, the effects of compressibility become more significant. For the acoustic analysis, the convective, Coriolis, and centrifugal acceleration terms do affect the results to a limited extent for a precession excitation and a large extent for a pressure excitation when the fluid operates at relatively high mach numbers.

REFERENCES

Bolleter, U., 1988, "Blade Passage Tones of Centrifugal Pumps", *Vibrations*, Vol. 4, September, pp. 8-13.

Childs, D. W., 1989, "Fluid-Structure Interaction Forces at Pump-Impeller-Shroud Surface for Rotordynamic Calculations," ASME *Journal of Vibrations, Acoustics, Stress, and Reliability in Design*, Vol. 111, July, pp. 216-225.

Childs, D. W., 1992, "Pressure Oscillations in the Leakage Annulus Between a Shrouded Impeller and Its Housing Due to Impeller-Discharge-Pressure Disturbances," *Journal of Fluids Engineering*, Vol. 114, March, pp. 61-67.

McCarthy, R. D., 1986, "Thermophysical Properties of Fluids, MIPROPS 86," NBS Standard Reference Data Base 12, Thermophysics Division, Center for Chemical Engineering, National Bureau of Standards, Boulder, Colorado.

Morrison, G. L., Rhode, D. L., Logan, K. C., Chi, D., Demco, J., 1983, "Labyrinth Seals for Incompressible Flow - Final Report," G. C. Marshall Space Flight Center, MSFC, Alabama, 35812, Report Number SEAL-4-83, November.

San Andres, L., 1991, "Analysis of Turbulent Hydrostatic Bearings with a Barotropic Fluid," Transactions of the ASME, ASME *Journal of Tribology*, pp. 1-10.

Thompson, P. A., *Compressible Fluid Mechanics*, Department of Mechanical Engineering, Rensselaer Polytechnic Institute, Troy, New York, 1988, pp. 159-163.

Thomson, W. T., *Laplace Transformations*, Prentice Hall, Inc., Englewood Cliffs, New Jersey, 1960, Second Edition, pp.181-201.

APPENDIX A

$$A_{4\theta} = \frac{u_{s0}^2}{2h_0\tilde{\rho}_0}\left[\sigma_r(u_{\theta 0} - 1)mr + \sigma_s u_{\theta 0} ms\right] \tag{A.1}$$

$$A_{4s} = \frac{u_{s0}^2}{2h_0\tilde{\rho}_0}\left(\sigma_r mr + \sigma_s ms\right) \tag{A.2}$$

Coefficient definitions for [A] *Eq. (40)*

$$A_{11} = \left[-\tilde{\rho}_0 u_{s0}\left(\frac{dh_0}{h_0 ds} + \frac{d\tilde{\rho}_0}{\tilde{\rho}_0 ds} + \frac{dr}{rds}\right) - A_{3s}\tilde{\rho}_0 + j\Gamma T\tilde{\rho}_0\right] u_{s0} / \left(\frac{d\tilde{\rho}_0}{dp}\frac{1}{\tilde{\rho}_0} - u_{s0}\tilde{\rho}_0\right) + \left(\frac{1}{h_0}\frac{dh_0}{ds} + \frac{1}{\tilde{\rho}_0}\frac{d\tilde{\rho}_0}{ds} + \frac{1}{r}\frac{dr}{ds}\right) \tag{A.3}$$

$$A_{12} = u_{s0}\left[A_{2s}\tilde{\rho}_0 + j\frac{\omega T}{r}\tilde{\rho}_0 u_{s0}\right] / \left(\frac{d\tilde{\rho}_0}{dp}\frac{1}{\tilde{\rho}_0} - u_{s0}^2\tilde{\rho}_0\right) \tag{A.4}$$

$$A_{13} = \frac{u_{s0}}{\tilde{\rho}_0 F_5}\frac{d\tilde{\rho}_0}{dp}\left[\tilde{\rho}_0 u_{s0}\frac{d\tilde{\rho}_0}{dp}\left(\frac{u_{s0}}{\tilde{\rho}_0^2}\frac{d\tilde{\rho}_0}{ds} + j\frac{\omega T u_{\theta 0}}{\tilde{\rho}_0 r}\right) - j\omega T u_{s0}\tilde{\rho}_0 - A_{4s}\tilde{\rho}_0\right] \tag{A.5}$$

$$A_{31} = \left[\tilde{\rho}_0 u_{s0}\left(\frac{dh_0}{h_0 ds} + \frac{d\tilde{\rho}_0}{\tilde{\rho}_0 ds} + \frac{dr}{rds}\right) + A_{3s}\tilde{\rho}_0 - j\Gamma T\tilde{\rho}_0\right] / F_5 \tag{A.6}$$

$$A_{32} = \left(A_{2s}\tilde{\rho}_0 + j\frac{\omega T}{r}\tilde{\rho}_0 u_{s0}\right) / F_5 \tag{A.7}$$

$$A_{33} = \frac{1}{\tilde{\rho}_0 F_5}\frac{d\tilde{\rho}_0}{dp}\left[\tilde{\rho}_0 u_{s0}\frac{d\tilde{\rho}_0}{dp}\left(\frac{u_{s0}}{\tilde{\rho}_0^2}\frac{d\tilde{\rho}_0}{ds} + j\frac{\omega T u_{\theta 0}}{\tilde{\rho}_0 r}\right) - j\omega T u_{s0}\tilde{\rho}_0 - A_{4s}\tilde{\rho}_0\right] \quad \textbf{(A.8)}$$

$$F_2 = \frac{u_{s0}}{h_0}\left(\frac{d^2 z}{ds^2} - \frac{1}{h_0}\frac{dh_0}{ds}\frac{dz}{ds}\right) \quad \textbf{(A.9)}$$

$$F_3 = \frac{u_{s0}}{h_0}\left(F_1 - \frac{G_0}{h_0}\frac{dh_0}{ds}\right) \quad \textbf{(A.10)}$$

$$F_5 = 1 + \frac{u_{s0}^2}{\tilde{\rho}_0}\frac{d\tilde{\rho}_0}{dp} \quad \textbf{(A.11)}$$

Right hand side definitions for equation 41

$$G_q = \frac{\left(-A_{1s}\tilde{\rho}_0\frac{dz}{ds} - \tilde{\rho}_0 u_{s0}F_2 - j\tilde{\rho}_0 u_{s0}\frac{\Gamma T}{h_0}\frac{dz}{ds}\right)}{\left(1 - u_{s0}^2\frac{d\tilde{\rho}_0}{dp}\right)} \quad \textbf{(A.12)}$$

$$\Gamma = \omega\left(f - u_{\theta 0}/r\right) \quad \textbf{(A.13)}$$

APPENDIX B

Coefficient definitions for **[B]** *of Eq. (50)*

$$B_{11} = \left[-\tilde{\rho}_0 u_{s0} \left(\frac{dh_0}{h_0 ds} + \frac{d\tilde{\rho}_0}{\tilde{\rho}_0 ds} + \frac{dr}{rds} \right) - A_{3s}\tilde{\rho}_0 + j\Gamma T\tilde{\rho}_0 \right] u_{s0} / \left(\frac{d\tilde{\rho}_0}{dp}\frac{1}{\tilde{\rho}_0} - u_{s0}\tilde{\rho}_0 \right) + \left(\frac{1}{h_0}\frac{dh_0}{ds} + \frac{1}{\tilde{\rho}_0}\frac{d\tilde{\rho}_0}{ds} + \frac{1}{r}\frac{dr}{ds} \right) \tag{B.1}$$

$$B_{12} = u_{s0}\left[A_{2s}\tilde{\rho}_0 + j\frac{n\omega T}{r}\tilde{\rho}_0 u_{s0} \right] / \left(\frac{d\tilde{\rho}_0}{dp}\frac{1}{\tilde{\rho}_0} - u_{s0}^2\tilde{\rho}_0 \right) \tag{B.2}$$

$$B_{13} = \frac{u_{s0}}{\tilde{\rho}_0 F_5}\frac{d\tilde{\rho}_0}{dp}\left[\tilde{\rho}_0 u_{s0}\frac{d\tilde{\rho}_0}{dp}\left(\frac{u_{s0}}{\tilde{\rho}_0^2}\frac{d\tilde{\rho}_0}{ds} + j\frac{n\omega T u_{\theta 0}}{\tilde{\rho}_0 r} \right) - jn\omega T u_{s0}\tilde{\rho}_0 - A_{4s}\tilde{\rho}_0 \right] \tag{B.3}$$

$$B_{31} = \left[\tilde{\rho}_0 u_{s0}\left(\frac{dh_0}{h_0 ds} + \frac{d\tilde{\rho}_0}{\tilde{\rho}_0 ds} + \frac{dr}{rds} \right) + A_{3s}\tilde{\rho}_0 - j\Gamma T\tilde{\rho}_0 \right] / F_5 \tag{B.4}$$

$$B_{32} = \left(A_{2s}\tilde{\rho}_0 + j\frac{n\omega T}{r}\tilde{\rho}_0 u_{s0} \right) / F_5 \tag{B.5}$$

$$B_{33} = \frac{1}{\tilde{\rho}_0 F_5}\frac{d\tilde{\rho}_0}{dp}\left[\tilde{\rho}_0 u_{s0}\frac{d\tilde{\rho}_0}{dp}\left(\frac{u_{s0}}{\tilde{\rho}_0^2}\frac{d\tilde{\rho}_0}{ds} + j\frac{n\omega T u_{\theta 0}}{\tilde{\rho}_0 r} \right) - jn\omega T u_{s0}\tilde{\rho}_0 - A_{4s}\tilde{\rho}_0 \right] \tag{B.6}$$

APPENDIX C

Coefficient definitions for [C] *of Eq. (57)*

$$C_{11} = \left[\frac{1}{h_0}\frac{dh}{ds} + \frac{1}{\tilde{\rho}_0}\frac{d\tilde{\rho}_0}{ds} + \frac{A_{3\theta}\omega^2 T^2 f}{rA_{\theta c}} + j\frac{(A_{2\theta}A_{3\theta}\omega T)}{rA_{\theta c}}\right] \tag{C.1}$$

$$C_{21} = A_{3s} - \frac{A_{2\theta}A_{3\theta}A_{2s}}{A_{\theta c}} + j\left(\omega Tf + \frac{A_{3\theta}A_{2s}}{A_{\theta c}}\right) \tag{C.2}$$

$$C_{12} = \frac{\omega T}{A_{\theta c}}\left[\frac{A_{2\theta}bL_s}{r^2 R_i\tilde{\rho}_0} + f\frac{d\tilde{\rho}_0}{dp}A_{4\theta}\right] + j\left[\frac{\Gamma T}{\tilde{\rho}_0}\frac{\tilde{\rho}_0}{dp} + \frac{1}{A_{\theta c}}\left(A_{2\theta}A_{4\theta}\frac{d\tilde{\rho}_0}{dp} - \frac{f\omega^2 T^2 bL_s}{rR_i\tilde{\rho}_0} + \frac{u_0}{\tilde{\rho}_0{}^2}\frac{d\tilde{\rho}_0}{ds}\right)\right] \tag{C.3}$$

$$C_{22} = -\frac{A_{2\theta}}{A_{\theta c}}\left(A_{4\theta}\frac{d\tilde{\rho}_0}{dp} - \frac{\omega TbL_s}{rR_i\tilde{\rho}_0}\right) - \frac{d\tilde{\rho}_0}{dp}A_{4s} + \frac{j}{A_{\theta c}}\left(A_{2\theta}\frac{b}{r}\frac{L_s}{R_i\tilde{\rho}_0} + \frac{d\tilde{\rho}_0}{dp}\omega TfA_{4\theta}\right) \tag{C.4}$$

$$A_{\theta c} = A_{2\theta}^2 + \omega^2 T^2 f^2 \tag{C.5}$$

APPENDIX D

Coefficient definitions for **[D]** *of Eq. (60)*

$$D_{11} = \left[\frac{1}{h_0}\frac{dh}{ds} + \frac{1}{r}\frac{dr}{ds} + \frac{A_{3\theta}n^2\omega^2T^2f}{rA_{\theta c}} + j\frac{(A_{2\theta}A_{3\theta}n\omega T)}{rA_{\theta c}}\right] \tag{D.1}$$

$$D_{21} = A_{3s} - \frac{A_{2\theta}A_{3\theta}A_{2s}}{A_{\theta c}} + j\left(n\omega Tf + \frac{A_{3\theta}A_{2s}}{A_{\theta c}}\right) \tag{D.2}$$

$$D_{12} = \frac{n\omega T}{A_{\theta c}}\left[\frac{A_{2\theta}bL_s}{r^2R_i\tilde{\rho}_0} + f\frac{d\tilde{\rho}_0}{dp}A_{4\theta}\right] + j\left[\frac{\Gamma T}{\tilde{\rho}_0}\frac{d\tilde{\rho}_0}{dp} + \frac{1}{A_{\theta c}}\left(A_{2\theta}A_{4\theta}\frac{d\tilde{\rho}_0}{dp} - \frac{fn^2\omega^2T^2bL_s}{rR_i\tilde{\rho}_0}\right)\right] \tag{D.3}$$

$$D_{22} = -\frac{A_{2\theta}}{A_{\theta c}}\left(A_{4\theta}\frac{d\tilde{\rho}_0}{dp} - \frac{n\omega TbL_s}{rR_i\tilde{\rho}_0}\right) - \frac{d\tilde{\rho}_0}{dp}A_{4s} + \frac{j}{A_{\theta c}}\left(A_{2\theta}\frac{b}{r}\frac{L_s}{R_i\tilde{\rho}_0} + \frac{d\tilde{\rho}_0}{dp}n\omega TfA_{4\theta}\right) \tag{D.4}$$

$$A_{\theta c} = A_{2\theta}^2 + n^2\omega^2T^2f^2 \tag{D.5}$$